

THESIS FOR THE DEGREE OF DOCTOR OF PHILOSOPHY

Integrated Motor Drives and Battery Chargers  
for Electric or Plug-in Hybrid Electric Vehicles

SAEID HAGHBIN



Division of Electric Power Engineering  
Department of Energy and Environment  
Chalmers University of Technology  
Gothenburg, Sweden, 2013

# Integrated Motor Drives and Battery Chargers for Electric or Plug-in Hybrid Electric Vehicles

SAEID HAGHBIN

ISBN 978-91-7385-811-3  
Doktorsavhandlingar vid  
Chalmers tekniska högskola  
Ny serie Nr 3492  
ISSN 0346-718X

Copyright ©2013 Saeid Haghbin  
except where otherwise stated.  
All rights reserved.

Division of Electric Power Engineering  
Department of Energy and Environment  
Chalmers University of Technology  
Gothenburg, Sweden

This thesis has been prepared using L<sup>A</sup>T<sub>E</sub>X.  
Printed by Chalmers Reproservice,  
Gothenburg, Sweden, 2013.

*To my family*



# Abstract

Plug-in vehicles, electric vehicles or plug-in hybrid electric vehicles, use grid power to charge the battery. The components in the traction circuit, like the electric motor and the inverter, are not used during the battery charging, so there is a possibility to use them in the charger circuit to reduce the size, weight and price of the on-board charger; that is called an integrated motor drive and battery charger or simply an integrated charger which can be galvanically isolated or non-isolated from the utility grid.

Different examples of integrated chargers reported by academia or industry, isolated or non-isolated, are reviewed and compared in terms of circuit configuration, control strategy, degree of integration, and efficiency. Moreover some new isolated and non-isolated solutions are presented and explained.

A patented integrated motor drive and isolated battery charger based on a split-phase permanent magnet (PM) motor is described where the motor windings are reconfigured for the traction and charging mode by using a relay-based switching device. To reduce the magnetization current due to the motor airgap, the motor rotates at synchronous speed during the battery charging. So, an extra clutch is used in the system to disconnect the motor from the vehicle transmission during the charge operation. The mathematical model of the split-phase PM motor based on a double  $dq$  approach, the developed controllers, and the system functionality are explained. Moreover, simulation and experimental results show that the system has a good performance in terms of system efficiency and dynamic response with two PM motor alternatives in two separate practical systems.

Two new categories of integrated motor drives and non-isolated battery chargers are presented and explained. The first scheme is based on the winding's reconfiguration of a split-phase PM motor which simulation and practical results are provided. The second scheme is a single-phase solution that a split-phase PM motor and two inverters enable battery charging.

Based on the double  $dq$  model of the split-phase PM motor that provides the theoretical framework, a modal field-oriented controller is proposed for a drive system that utilizes two identical inverters and a split-phase PM motor. A decoupling strategy is proposed based on the eigenvalue decomposition to impart a systematic methodology for the current controllers design. Moreover, a maximum torque per ampere strategy is derived to reach an optimal torque development in the drive system. Simulation results are provided to show the system performance in the steady-state and dynamic for a speed control system. For a reference speed profile, the drive system has a fast speed response while the torque and currents are tracking the optimal trajectories.

**Keywords**

Plug-in vehicles, battery charger, integrated motor drive and battery chargers, split-phase PM motor, isolated and non-isolated integrated charges, field-oriented control, maximum torque per Ampere strategy.

# Acknowledgment

First of all, I would like to thank Professor Ola Carlson, my supervisor and examiner, for his continuous and consistent support and encouragement during the work. It might not be possible to finish the work without his support. Additionally, I would like to thank Dr. Sonja Lundmark, my co-supervisor, for her kind help and support.

Special thanks also go to Professor Torbjörn Thiringer for his valuable contribution and effort in this work. He was firstly my examiner and I have had many technical discussions with him which were quite useful and enjoyable.

I would also like to thank Chalmers University of Technology, the Swedish Hybrid Vehicle Center (SHC), the partners within the SHC, and the Swedish Energy Agency for their financial support of the project. Special thanks go to Professor Mats Alaküla, Mats Leksell, and Dr. Oskar Wallmark, within the SCH Theme 2 working group, for technical discussions in the initial stages of the project. Additionally, many thanks go to Professor Hector Zelaya from ABB for his technical comments and valuable resources.

I would like to thank Sylvain Lechat Sanjuan, David Vindel Munoz, Javier Fernandez Mandiola, Daniel Castro Carmon, and Isabel Serrano Guillen, master students at the division, for their contributions to this work.

As a part of this project, I was hosted by Professor Ronald Harley and Professor Thomas Habetler at the Georgia Institute of Technology, in Atlanta, USA, as a research visitor. I would like to thank them and other colleagues there for their time and contribution.

Many people from industry and academia have been involved in the practical system development for this project. I would like to thank them all for their assistance, as well as my colleagues at the Electric Power Engineering Division (Elteknik) at Chalmers for the time we have been together.

My heartfelt thanks go to my family especially Maliheh Sadeghi Kani, my wife, for the endless love, support, and patience.

Saeid Haghbin  
Gothenburg, February 2013



# List of Publications and Patents

The following publications and patents are direct or indirect result of this work. The content of the thesis is mainly based on these materials.

## Journal Papers

1. Haghbin, S.; Khan, K.; Zhao, Z.; Lundmark, S.; Alakula, M.; Carlson, O.; , "An Integrated 20 *kW* Motor Drive and Isolated Battery Charger for Plug-in Vehicles," *Power Electronics, IEEE Transactions on*, vol. 28, Issue 8, pp. 4013-4029, 2013.
2. Haghbin, S.; Zelaya, H.; Carlson, O.; , "Modal Field-Oriented Control of a Split-Phase PM Motor with Dual Inverters," will be published in the *Journal of Electrical and Control Engineering*, 2013.
3. Haghbin, S.; Lundmark, S.; Alakula, M.; Carlson, O.; , "Grid-Connected Integrated Battery Chargers in Vehicle Applications: Review and New Solution," *Industrial Electronics, IEEE Transactions on* , vol.60, no.2, pp.459-473, Feb. 2013, doi: 10.1109/TIE.2012.2187414.
4. Haghbin, S.; Lundmark, S.; Alakula, M.; Carlson, O.; , "An Isolated High-Power Integrated Charger in Electrified-Vehicle Applications," *Vehicular Technology, IEEE Transactions on* , vol.60, no.9, pp.4115-4126, Nov. 2011 doi: 10.1109/TVT.2011.2162258.

## Conference Papers

1. Haghbin, S.; Serrano Guillen, I.; , "An Integrated Motor Drive and Non-Isolated Battery Charger Based on the Torque Cancellation in the Motor," will be presented in *IEEE International Conference on Power Electronics and Drive Systems, PEDS*, 2013.
2. Haghbin, S.; Sadeghi Kani, M.; Vindel, D.; Carlson, O.; Lundmark, S.; , "A Trigonometric Velocity Estimator Using Resolver Sensor Position Information for Drive Systems," in *39th Annual Conference of the IEEE Industrial Electronics Society, IECON*, 2012.

3. Haghbin, S.; Thiringer, T.; Carlson, O.; , "An Integrated Split-Phase Dual-Inverter Permanent Magnet Motor Drive and Battery Charger for Grid-Connected Electric or Hybrid Vehicles," *Electrical Machines (ICEM), XX International Conference on* , Sept. 2012.
4. Fernández Mandiola, J.; Castro Carmona, D.; Haghbin, S.; Abdulahovic, T.; Ellsén, M.; , "An FPGA Implementation of a Voltage-Oriented Controlled Three-Phase PWM Boost Rectifier," in *International Conference on Electrical Systems for Aircraft, Railway and Ship Propulsion - ESARS 2012*.
5. Vindel, David; Haghbin, Saeid; Rabiei, Ali; Carlson, Ola; Ghorbani, Reza; , "Field-oriented control of a PMSM drive system using the dSPACE controller," *Electric Vehicle Conference (IEVC), 2012 IEEE International* , vol., no., pp.1-5, 4-8 March 2012 doi: 10.1109/IEVC.2012.6183206.
6. Shuang Zhao; Haghbin, S.; Wallmark, O.; Leksell, M.; Lundmark, S.; Carlson, O.; , "Transient modeling of an integrated charger for a plug-in hybrid electric vehicle," *Power Electronics and Applications (EPE 2011), Proceedings of the 2011-14th European Conference on* , vol., no., pp.1-10, Aug. 30 2011-Sept. 1 2011.
7. Haghbin, S.; Lundmark, S.; Carlson, O.; Alakula, M.; , "A combined motor/drive/battery charger based on a split-windings PMSM," *Vehicle Power and Propulsion Conference (VPPC), 2011 IEEE* , vol., no., pp.1-6, 6-9 Sept. 2011 doi: 10.1109/VPPC.2011.6043000.
8. Erfani, M.J.; Thiringer, T.; Haghbin, S.; , "Performance and losses analysis of charging and discharging mode of a bidirectional DC/DC fullbridge converter using PWM switching pattern," *Vehicle Power and Propulsion Conference (VPPC), 2011 IEEE* , vol., no., pp.1-6, 6-9 Sept. 2011 doi: 10.1109/VPPC.2011.6043141.
9. Haghbin, S.; Khan, K.; Lundmark, S.; Alakula, M.; Carlson, O.; Leksell, M.; Wallmark, O.; , "Integrated chargers for EV's and PHEV's: examples and new solutions," *Electrical Machines (ICEM), 2010 XIX International Conference on* , vol., no., pp.1-6, 6-8 Sept. 2010 doi: 10.1109/ICELMACH.2010.5608152.
10. Khan, K.; Haghbin, S.; Leksell, M.; Wallmark, O.; , "Design and performance analysis of a permanent-magnet assisted synchronous reluctance machine for an integrated charger application," *Electrical Machines (ICEM), 2010 XIX International Conference on* , vol., no., pp.1-6, 6-8 Sept. 2010 doi: 10.1109/ICELMACH.2010.5607905.
11. Haghbin, S.; Alakula, M.; Khan, K.; Lundmark, S.; Leksell, M.; Wallmark, O.; Carlson, O.; , "An integrated charger for plug-in hybrid electric vehicles based on a special interior permanent magnet motor," *Vehicle Power and Propulsion Conference (VPPC), 2010 IEEE* , vol., no., pp.1-6, 1-3 Sept. 2010 doi: 10.1109/VPPC.2010.5729071.

12. Haghbin, S.; Lundmark, S.; Carlson, O.; , "Performance of a direct torque controlled IPM drive system in the low speed region," *Industrial Electronics (ISIE)*, 2010 IEEE International Symposium on , vol., no., pp.1420-1425, 4-7 July 2010 doi: 10.1109/ISIE.2010.5637830.
13. Moshari, A.; Yousefi, G.R.; Ebrahimi, A.; Haghbin, S.; , "Demand-side behavior in the smart grid environment," *Innovative Smart Grid Technologies Conference Europe (ISGT Europe)*, 2010 IEEE PES , vol., no., pp.1-7, 11-13 Oct. 2010 doi: 10.1109/ISGTEUROPE.2010.5638956.
14. Haghbin, S.; Thiringer, T.; , "Impact of inverter switching pattern on the performance of a direct torque controlled synchronous reluctance motor drive," *Power Engineering, Energy and Electrical Drives, 2009. POWERENG '09. International Conference on* , vol., no., pp.337-341, 18-20 March 2009 doi: 10.1109/POWERENG.2009.4915173.

## Patents

1. Saeid Haghbin (Chalmers University of Technology) and Mats Alakula (Lund University), Electrical Apparatus Comprising Drive System and Electrical Machine with Reconnectable Stator Winding, International Patent, Pub. No.: WO/2011/159241, Publication Date: 22-12-2011. The patent is an extension of the following Swedish Patent.
2. Saeid Haghbin (Chalmers University of Technology) and Mats Alakula (Lund University), Elektrisk apparat innefattande drivsystem och elektrisk maskin med omkopplingsbar statorlindning, Swedish Patent Office, Patent no 1050607-9, Grant date: 14-02-2012.
3. Reza Ghorbani (University of Hawaii) and Saeid Haghbin (Chalmers University of Technology), Battery Charge Station Using On-Board Motor Drive, US Patent no. 61540741 filed on 29-09-2011, pending.



# Nomenclatures

<i>PM</i>	.....	permanent magnet
$\dot{i}_x$	.....	current with index i
$v_x$	.....	voltage with index i
<i>d</i>	.....	direct axis
<i>q</i>	.....	quadrature axis
<i>PHEV</i>	.....	plug-in hybrid electric vehicles
<i>EV</i>	.....	electric vehicles
<i>RCD</i>	.....	residual current device
<i>MTPA</i>	.....	maximum torque per ampere
<i>FOC</i>	.....	field-oriented control
<i>PWM</i>	.....	pulse width modulation
<i>SPWM</i>	.....	sinusoidal pulse width modulation
<i>V2G</i>	.....	vehicle to grid
<i>EMI</i>	.....	electromagnetic interference
<i>MMF</i>	.....	magnetomotive force
<i>PFC</i>	.....	power factor correction
<i>PI</i>	.....	proportional integral
<i>THD</i>	.....	total harmonic distortion
<i>SVM</i>	.....	space vector modulation
<i>SRM</i>	.....	switched reluctance motor
<i>PMSM</i>	.....	permanent magnet synchronous motor
<i>IPMSM</i>	.....	interior permanent magnet synchronous motor
$v_x$	.....	voltage of phase x

---

$i_x$	.....	current of phase x
$r_s$	.....	stator resistance
$\psi_x$	.....	flux of phase x
$L_{xy}$	.....	inductance of xy
$\psi_{pm}$	.....	permanent magnet flux
$\theta_r$	.....	angle between the rotor d axis and the magnetic axes of winding $a'_1 a_1$
$\bar{L}_m$	.....	average value of the magnetization inductance
$L_{\Delta m}$	.....	half-amplitude of the sinusoidal variation of the magnetization inductance
$L_{ls}$	.....	leakage inductance
$\mathbf{L}_s$	.....	inductance matrix
$\mathbf{i}_s$	.....	current vector
$\mathbf{v}_s$	.....	voltage vector
$\psi_{pm}$	.....	flux vector
$\mathbf{R}_s$	.....	resistance matrix
$\mathbf{I}_6$	.....	$6 \times 6$ identity matrix
$T_e$	.....	torque
$P$	.....	number of poles
$J$	.....	moment of inertia
$B_m$	.....	viscous friction coefficient
$T_L$	.....	load torque
$\omega_r$	.....	electrical speed
$\mathbf{K}_s$	.....	extended Clark/Park transformation matrix
$\mathbf{i}_s^r$	.....	current vector in the rotor reference frame
$\mathbf{v}_s^r$	.....	voltage vector in the rotor reference frame
$\psi_{pm}^r$	.....	flux vector in the rotor reference frame
$v_d$	.....	voltage in the $d$ direction
$v_q$	.....	voltage in the $q$ direction
$i_d$	.....	current in the $d$ direction
$i_q$	.....	current in the $q$ direction

---

$L_d$	.....	inductance in the $d$ direction
$L_q$	.....	inductance in the $q$ direction
$L_{md}$	.....	mutual inductance in the $d$ direction
$L_{mq}$	.....	mutual inductance in the $q$ direction
$EMF$	.....	electro motive force
$v_\alpha$	.....	voltage in the $\alpha$ direction
$v_\beta$	.....	voltage in the $\beta$ direction
$v_{ag}$	.....	grid voltage for the phase a
$v_{bg}$	.....	grid voltage for the phase b
$v_{cg}$	.....	grid voltage for the phase c
$p$	.....	active power
$q$	.....	reactive power
$PMaSynRM$	....	permanent magnet assisted synchronous reluctance motor
$EMC$	.....	electromagnetic compatibility
$IGBT$	.....	insulated-gate bipolar transistor
$RDC$	.....	resolver-to-digital converter
$RD$	.....	resolver-to-digital
$PCB$	.....	printed circuit board
$TTL$	.....	transistor-transistor logic
$I/O$	.....	input/output
$RTI$	.....	real-time interface
$PC$	.....	personal computer
$ISA$	.....	industry standard architecture
$CMOS$	.....	complementary metaloxidesemiconductor
$PLL$	.....	phased-locked loop
$VCO$	.....	voltage controlled oscillator
$LSB$	.....	least significant bit
$T_s$	.....	sampling time
$W$	.....	noise
$L_r$	.....	leakage inductance

$n_i$	neutral point of three-phase winding i
$\lambda_i$	eigenvalue with index i
$\tau_i$	time constant with index i
$\mathbf{e}_i$	eigenvector with index i
$I_s$	magnitude of the stator current
$G_x(s)$	transfer function with index x
$F_e(s)$	controller transfer function
<i>IMC</i>	internal mode control
$\alpha_e$	closed-loop system bandwidth
$t_r$	rise time
$K_p$	proportional gain
$K_i$	integrator gain
$R$	resistance
$L$	inductance
$t$	time
$s$	second
$A$	Ampere
$V$	volt
$W$	Watt
<i>SynRM</i>	synchronous reluctance motor
<i>FEM</i>	finite element method

# List of Tables

2.1	Comparison of integrated charger examples. . . . .	20
4.1	Design summary of the 20 <i>kW</i> PM motor. . . . .	40
4.2	20 <i>kW</i> PM motor parameters respect to the terminals connected to the inverter. . . . .	41
6.1	Split-phase PM motor parameters . . . . .	105



# List of Figures

2.1	A simple diagram of the traction system of a parallel plug-in hybrid electric vehicle. . . . .	7
2.2	Electrical traction in a vehicle based on an ac motor and a three-phase inverter. . . . .	7
2.3	Non-isolated single-phase integrated charger based on an induction motor drive system. . . . .	8
2.4	Three-phase non-isolated integrated charger based on a split-phase ac motor. . . . .	10
2.5	Charging mode equivalent circuit of the three-phase integrated charger based on a split-phase ac motor. . . . .	11
2.6	Charging mode equivalent circuit of the single-phase integrated charger based on a split-phase ac motor. . . . .	12
2.7	Single-phase integrated battery charger for a four wheel drive system. . . . .	13
2.8	System equivalent circuit for the four wheel drive integrated charger during battery charging. . . . .	14
2.9	Single-phase integrated charger based on a PM motor for an electric scooter. . . . .	15
2.10	Three-phase isolated integrated charger based on a wound-rotor induction motor. . . . .	16
2.11	Single-phase integrated charger based on a SRM drive system. . . . .	17
2.12	Single-phase isolated integrated charger based on a dual converter SRM drive. . . . .	17
2.13	System diagram of proposed integrated charger based on the combined bidirectional AC/DC and DC/DC converter. . . . .	18
3.1	Cross section area of a split-phase PM motor with an arbitrary phase-shift angle between two sets of three-phase windings. . . . .	24
4.1	The power stage of the three-phase boost converter. . . . .	32
4.2	Integrated motor drive and isolated battery charger based on the split-phase PM motor for a PHEV. . . . .	32
4.3	Circuit diagram of the proposed isolated integrated charger for a conceptual two pole motor: (a) traction mode and (b) charging mode. . . . .	33
4.4	System operation in battery charging mode: grid synchronization and charge control. . . . .	36

4.5	The inverter reference current as a function of charging power.	37
4.6	20 kW system modes of operation: a) traction and b) charging.	38
4.7	Geometry of the prototype 20 kW PM motor. . . . .	39
4.8	A simplified diagram of the 20 kW PM motor cross section including slot numbering and conductors arrangement. . . . .	39
4.9	Simulation result: grid power to the charger system. . . . .	42
4.10	Simulation result: electrical speed of the motor/generator. . . . .	42
4.11	Simulation result: motor/generator torque during charge time.	43
4.12	Simulation result: phase A of the motor and grid voltages during the synchronization and contactor closing time. . . . .	43
4.13	Simulation result: phase A of the grid current during charge operation. . . . .	44
4.14	Simulation result: three-phase grid currents during the start of high-power charging. . . . .	44
4.15	Simulation result: three-phase grid currents during the step change in the charging power from 2 kW to -500 W. . . . .	44
4.16	Simulation result: phase A grid voltage (V) and scaled grid current (1/20A) during the step change in the charging power from 2 kW to -500 W. . . . .	45
4.17	The experimental setup including the vehicle. . . . .	46
4.18	Block diagram of the experimental system: integrated 20 kW motor drive and isolated battery charger. . . . .	47
4.19	Motor installation inside the vehicle. . . . .	48
4.20	Installed panel inside the vehicle including the inverter, switching relays, sensors and so on. . . . .	48
4.21	Circuit diagram of relay-based switching device for windings reconfiguration from the traction mode to charging mode and vice versa. . . . .	50
4.22	Standalone rack including the dSPACE interfaces, resolver, fast protection and other auxiliaries. . . . .	52
4.23	Measurement: back EMF voltage of the motor windings in the charging mode. . . . .	53
4.24	Measurement: phase A voltage of the grid and motor during synchronization and before closing the contactor. . . . .	54
4.25	Measurement: phase A of the grid voltage and current during the battery charging operation. . . . .	54
4.26	Measurement: system efficiency in charging mode. . . . .	56
4.27	Measurement: system dynamic response to the step change of the charging power. . . . .	56
4.28	Block diagram of the experimental system: integrated 1 kW motor drive and battery charger. . . . .	58
4.29	Photo of the 1 kW experimental system. . . . .	60
4.30	Resolver-to-Digital PCB. . . . .	61
4.31	Measurement: the motor grid-side winding and grid phase A voltages: a) before synchronization b) after synchronization. . . . .	61
4.32	Block diagram of (a) the resolver and (b) the tracking loop of an RD converter. . . . .	64
4.33	Block diagram of the proposed trigonometric open-loop velocity estimator. . . . .	65

4.34	Simulation result: true and estimated speed/position by the trigonometric estimator. . . . .	67
4.35	Measurement: the reference and estimated velocity in the drive system. . . . .	68
4.36	Measurement: the rotor angle during: a)start up, b)speed reversal. . . . .	69
5.1	Non-isolated battery charger based on the dual-winding motor and a switching device: the charge power is equal to the traction power. . . . .	74
5.2	Non-isolated battery charger based on the dual-winding motor and a switching device: the charge power is twice of the traction power. . . . .	75
5.3	Non-isolated battery charger based on the split-phase 20 kW PM motor with the parallel connected windings. . . . .	76
5.4	Simulation result: magnetic flux density distribution in the 20 kW IPMSM during battery charging in non-isolated charger with a sinusoidal current supply. . . . .	77
5.5	Simulation result: Phase inductance in the 20 kW PM motor during battery charging in non-isolated charger with a parallel connected winding arrangement. . . . .	78
5.6	Simulation result: developed torque in the 20 kW PM motor during battery charging in non-isolated charger with a parallel connected winding arrangement. . . . .	79
5.7	Main diagram of the practical setup of the non-isolated integrated charger. . . . .	80
5.8	Practical setup for testing the non-isolated integrated charger for the 20 kW PM motor. . . . .	80
5.9	Measurement: supply voltage and motor waveforms of non-isolated integrated charger in the bridge rectifier setup. . . . .	81
5.10	Measurement and simulation: measurement and Matlab simulation of the motor phase voltage and current of non-isolated integrated charger in the bridge rectifier setup. . . . .	81
5.11	Integrated motor drive and non-isolated battery charger based on the split-phase PM motor and dual inverters. . . . .	83
5.12	FOC of a split-phase PM motor with dual inverters using MTPA for the traction mode. . . . .	85
5.13	Integrated battery charger based on split-phase PM motor and dual inverters in battery charge mode. . . . .	86
5.14	Simulation result: grid current and voltage during battery charging for a charge level step change from 2.5 kW to 10 kW. . . . .	88
5.15	Simulation result: grid current during battery charging for grid half period. . . . .	88
5.16	Simulation result: grid current during battery charging for a few switching periods. . . . .	89
6.1	Drive system structure of the split-phase PM motor with dual inverters. . . . .	93

---

6.2	Proposed modal FOC for the split-phase PM motor with dual inverters based on the MTPA. . . . .	100
6.3	Vector diagram of the motor in steady state and with identical $dq$ currents for each set of windings. . . . .	101
6.4	Simulation result: electrical reference speed and motor speed in traction. . . . .	104
6.5	Simulation result: motor developed electromagnetic torque. . .	104
6.6	Simulation result: reference values of $dq$ currents based on the MTPA strategy. . . . .	106
6.7	Simulation result: three-phase currents in one set of the three- phase windings. . . . .	106
6.8	Simulation result: phase A currents for the first and the second set of windings. . . . .	107
7.1	Motor configuration as a step down grid-frequency single-phase transformer: a) winding placement b) equivalent circuit. . . . .	113

# Contents

<b>Abstract</b>	<b>v</b>
<b>Acknowledgment</b>	<b>vii</b>
<b>List of Publications and Patents</b>	<b>ix</b>
<b>Nomenclatures</b>	<b>xiii</b>
<b>List of Tables</b>	<b>xvii</b>
<b>List of Figures</b>	<b>xvii</b>
<b>1 Introduction</b>	<b>1</b>
1.1 Project Background . . . . .	2
1.2 Purpose of the Thesis and Contributions . . . . .	3
1.3 Thesis Outline . . . . .	4
<b>2 Integrated Motor Drives and Battery Chargers in Vehicle Applications: Review and Comparison</b>	<b>5</b>
2.1 Battery Chargers in Vehicle Applications . . . . .	5
2.2 Examples of Integrated Motor Drives and Battery Chargers . .	6
2.2.1 A Combined Motor Drive and Battery Recharge System Based on an Induction Motor . . . . .	8
2.2.2 Non-isolated Integrated Charger Based on a Split-Winding AC Motor . . . . .	10
2.2.3 An Integral Battery Charger for a Four-Wheel Drive Electric Vehicle . . . . .	12
2.2.4 An Integrated Charger Based on a PM Motor for an Electric Scooter . . . . .	14
2.2.5 An Integrated Charger for a Fork Lift Truck . . . . .	15
2.2.6 Single-Phase Integrated Charger Based on a Switched Reluctance Motor Drive . . . . .	16
2.2.7 Single-Phase Integrated Charger Based on a Dual Converter Switched Reluctance Motor Drive . . . . .	17
2.2.8 Integrated Bidirectional AC/DC and DC/DC Converter for PHEVs . . . . .	18
2.2.9 Comparison of Integrated Chargers . . . . .	19

<b>3</b>	<b>Double dq Modeling of the Split-Phase PM Motor</b>	<b>23</b>
3.1	Voltage and Flux Equations . . . . .	24
3.2	Inductances as the Function of Rotor Position . . . . .	25
3.3	Electromagnetic Torque and Mechanical Dynamics . . . . .	27
3.4	Extended Park Transformation . . . . .	27
3.5	Dynamical Equations in the dq Reference Frame . . . . .	28
<b>4</b>	<b>An Isolated Integrated Charger Based on the Split-Phase PM Motor</b>	<b>31</b>
4.1	Proposed Isolated Integrated Charger . . . . .	31
4.2	System Operation in Traction and Charging . . . . .	33
4.2.1	Grid Synchronization and Battery Charge Control . . .	34
4.2.2	Battery Charge Strategy . . . . .	37
4.3	An Experimental Setup Based on a 20 kW Split-Phase IPMSM	38
4.3.1	PM Motor Design . . . . .	38
4.3.2	Traction Mode Operation . . . . .	40
4.3.3	Simulation Results of the 20 kW Motor in Charging Mode	40
4.3.4	Description of the 20 kW Experimental Setup . . . . .	45
4.3.5	Practical Results of the 20 kW System and Discussions	53
4.4	An Experimental Setup Based on a 1 kW Split-Phase PMSM .	57
4.5	A Trigonometric Velocity Estimator Using a Resolver Sensor .	62
4.5.1	Resolver and RD Converter for Position Measurement .	63
4.5.2	The Proposed Trigonometric Velocity Estimator . . . .	65
<b>5</b>	<b>Integrated Motor Drives and Non-Isolated Battery Chargers</b>	<b>71</b>
5.1	Non-Isolated Battery Chargers Based on the Dual-Windings Motor and a Switching Relay . . . . .	72
5.2	Non-Isolated Battery Chargers Based on the Split-Phase PM Motor and a Switching Relay . . . . .	76
5.2.1	Non-Isolated Integrated Charger Based on the Split-Phase PM Motor: FEM Simulation Results . . . . .	77
5.2.2	Non-Isolated Integrated Charger Based on the Split-Phase PM Motor: Practical System Results . . . . .	79
5.3	Integrated Motor Drive and Non-Isolated Battery Charger Based on a Split-Phase PM Motor and Dual Inverters . . . . .	82
5.3.1	System Operation in Traction Mode: FOC of Split-Phase PM Motor . . . . .	82
5.3.2	System Configuration in Battery Charging Mode . . . .	84
5.3.3	Simulation Results for Charging Mode . . . . .	87
<b>6</b>	<b>Modal Field-Oriented Control of a Split-Phase PM Motor with Dual Inverters</b>	<b>91</b>
6.1	Drive System of the Split-Phase PM Motor with Dual Inverters	92
6.2	Modal State-Space Model of the Split-Phase PM Motor . . . .	94
6.2.1	System State-Space Model Using Currents as States . .	95
6.3	FOC of the Drive System Using Decomposed Variables . . . .	98
6.3.1	MTPA Strategy for the Split-Phase PM Motor . . . . .	99
6.3.2	Design of Current PI Controllers . . . . .	102
6.4	Simulation Results for the Drive System . . . . .	103

---

<b>7</b>	<b>Conclusions and Future Work</b>	<b>109</b>
7.1	Conclusions . . . . .	109
7.2	Future Work . . . . .	111
7.2.1	Future Work Suggestions for Integrated Motor Drive and Isolated Battery Chargers . . . . .	111
7.2.2	Future Work Suggestions for Integrated Motor Drive and Non-Isolated Battery Chargers . . . . .	112
	<b>Bibliography</b>	<b>115</b>



# Chapter 1

## Introduction

Internal combustion engines provide the traction power for the vehicles through a fuel combustion process in which the carbon generation is inevitable. It turns out that a more electric transportation system is the most realistic solution for the next generation of the transport systems like vehicles. Battery as the energy storage device is the main challenge in this regard which still needs more research and development. They are still expensive and it takes some time to recharge them compared to a normal fuel based vehicle which needs 10-15 minutes for the refueling.

Compared to a normal vehicle, electric vehicles (EVs) have a range limitation problem so there has been limited EV production so far. Hybrid vehicles offer the promise of higher energy efficiency and reduced emissions when compared with conventional automobiles, but they can also be designed to overcome the range limitations inherent in a purely electric automobile by utilizing two distinct energy sources for propulsion. A plug-in hybrid electric vehicle (PHEV) is a hybrid vehicle with batteries that can be recharged by connecting a plug to an electric power source. It shares the characteristics of both conventional hybrid electric vehicles and battery electric vehicles, having an internal combustion engine and batteries for power. PHEVs have been considered as a significant advancement of the hybrid vehicle technology in both the industry and the academia and even by various government agencies around the world.

PHEVs and EVs use grid power to charge the battery while the vehicle is parked. Generally there are two types of battery chargers: on-board type and stand-alone (off-board) type. Moreover, these battery chargers can be galvanically isolated or non-isolated from the utility grid. Normally the traction circuit components including the electric motor, inverter, and sensors are not engaged during the battery charging. So there is a possibility to use them in the charger circuit to reduce the system volume, weight, and cost. That is called an integrated motor drive and battery charger or simply an integrated charger in this context.

In this thesis, different types of integrated motor drive and battery chargers, isolated and non-isolated, are reviewed and compared in detail. Moreover, some new isolated and non-isolated integrated chargers are presented including the design, analysis, simulation and experimental results. Some general backgrounds, aim of the thesis, the main contributions and the thesis outline

are briefly presented in this chapter.

## 1.1 Project Background

The battery has an important role in the development of EVs or PHEVs [1] as an energy storage device. The performance of battery modules depends not only on the design of modules, but also on how the modules are used and charged. In this sense, battery chargers play a critical role in the evolution of this technology.

The on-board battery charger gives flexibility to charge anywhere where there is an electric power outlet available. However, the on-board type has the drawback of adding weight, volume and cost to the vehicle, thus it is usually made for lower powers ( $< 3.5 \text{ kW}$ ). When higher charging power is needed, the size and weight of the charger is easier to handle with an off-board charger. Vehicles with a longer EV-range (e.g.  $> 100 \text{ km}$ ) may require filling large amounts of energy (e.g.  $> 20 \text{ kWh}$ ) in reasonably short time. Even a 30 minute charging time would require a charging power of  $40 \text{ kW}$  or more, which is on the high side and very well may be limited by the maximum allowed continuous battery power. With a significantly increased fleet of EV's, the need for long charging times, compared to filling e.g. gasoline, implies the need for an un-proportionally large amount of charging stations, that will be expensive. Then, high power on-board chargers are attractive if the weight, volume and cost can be handled. In that case the infrastructure requirement [2] would be reduced to rather simple high power outlets and thus the cost would be significantly lower than that off-board chargers.

Galvanic isolation from the utility grid is a favorable option in the charger circuits because of safety reasons [3–5], but isolated on-board chargers are usually avoided due to its cost impact on the system. As described in [4], if normal non-dedicated socket-outlets are being used for charging, a residual current device (RCD) should be used to monitor the earth current for safe operation. Moreover, with a dedicative socket-outlet, earth current monitoring is an optional function as mentioned in the standard. The electrical continuity of the earth conductor should be permanently monitored by the charger, and in the case of loss of electrical continuity of the earth conductor, the charger shall be switched off [5]. In addition, if the traction battery is bonded to the vehicle chassis, the charging system shall provide a galvanic isolation between the mains and the battery [4]. So electrical separation of the traction system and mains supply provides more convenience and freedom to fulfill the standard requirements, beyond increased safety in the system. For example, in non-isolated versions of chargers a lot of shielding and safety issues should be considered in the whole vehicle electrical system [3] to prevent unwanted earth fault protection trip due to the presence of common mode currents and noise. With galvanic isolation, impact of the high-power converter on the earth path will be drastically reduced.

Different types of integrated chargers are reported by academia or industry that are reviewed and compared in this thesis [6, 7]. Moreover, as a main result of this thesis, a high-power integrated motor drive and isolated battery charger based on a split-phase PM motor is presented and explained [8, 9]. The main

idea is to use the motor as a grid-connected generator with extra terminals. The concept of this rotary transformer or motor/generator for this application is the subject of a Swedish patent [10] that is extended to an international patent [11].

In the context of this application, the split-phase PM motor is investigated in more detail to provide a solid theoretical background for the proposed integrated chargers. The modeling, control and drive system of the split-phase PM motor are investigated for different configurations. As an example, a non-isolated integrated charger is proposed for a drive system based on the split-phase PM motor and dual inverter.

The non-isolated integrated chargers are important devices which are the dominant available type in the market. Beside the review and comparison of these integrated chargers, some new schemes are proposed that are explained in the thesis.

Different practical systems are designed and implemented to verify the proposed systems. The developed experimental systems are presented including the results, limitations and recommendations.

## 1.2 Purpose of the Thesis and Contributions

The main objective of the work reported in this thesis is to enhance the research area for the integrated motor drives and battery chargers. So different types of integrated chargers are proposed and described including experimental results to validate the proposed schemes. Moreover, in the context of the integrated chargers, modeling and control of the split-phase PM motors are investigated and explained.

In summary, the main contributions can be itemized as:

- A comprehensive review and comparison of available integrated chargers reported by industry or academia
- Mathematical modeling of the split-phase motor using a double  $dq$  approach with an extended Park transformation for an arbitrary phase-shift between two sets of stator three-phase windings
- Proposition, simulation, analysis, control development, and implementation of a high-power motor drive and isolated battery charger based on a split-phase PM motor
- Proposition, simulation, control development and partial implementation of high-power motor drives and non-isolated battery chargers for two different configurations of the drive system
- Proposition, analysis and simulation of a decoupled control strategy for a drive system based on a split-phase PM motor and dual inverters using the eigenvalue decomposition of the state-space model
- Development of a maximum torque per ampere control strategy for a drive system based on the split-phase PM motor and dual inverters using the double  $dq$  approach

## 1.3 Thesis Outline

After this introduction chapter, different types of integrated chargers reported by industry or academia are presented and compared. The mathematical modeling of the split-phase PM motor is described in the third chapter to provide a theoretical background for the rest of chapters. Chapter 4 is devoted to the proposed isolated integrated charger including the description of system functionality, developed controllers, simulation results, and experimental results. Chapter 5 is assigned to non-isolated integrated chargers where some new schemes are presented. A Maximum torque per ampere (MTPA) strategy for a split-phase PM motor drive system with dual inverters is described in chapter 6. Based upon, a decoupled field-oriented control (FOC) resulting from an eigenvalue decomposition transformation is presented in this chapter too. Conclusion and further work suggestions are provided in the last chapter, chapter 7.

## Chapter 2

# Integrated Motor Drives and Battery Chargers in Vehicle Applications: Review and Comparison

This chapter is started by a general introduction of battery chargers in vehicle applications. Different type of integrated motor drives and battery chargers are presented including a comprehensive reference list. The chapter is ended by a comparison table that summarizes different integrated chargers.

### 2.1 Battery Chargers in Vehicle Applications

There are different classifications for battery chargers in vehicle applications. They are divided in two main categories of on-board and off-board types. The on-board type gives the freedom to the user to charge everywhere that a plug is available and the second one has an advantage of high-power charging that is fast charging. The subject of this thesis is on-board battery chargers, so the off-board types are not addressed here.

Galvanic isolation from the utility grid divides the charger types to isolated or non-isolated types. At the first chapter, a short explanation is provided to give more insight regarding this topic.

Another widely used classification is according to charger power level. Three power levels are used in this classification [2, 12] in which a rough estimation of the charging time can be conceived.

- **Level 1:** Common household type of circuit in the US rated to 120  $V$  and up to 15  $A$ .
- **Level 2:** Permanently wired electric vehicle supply equipment used specially for electric vehicle charging and it is rated up to 240  $V$ , up to 60  $A$ , and up to 14.4  $kW$ .

- **Level 3:** Permanently wired electric vehicle supply equipment used specially for electric vehicle charging and it is rated greater than 14.4 kW.

Equivalently, above categories are known as emergency charger which charges the battery pack of a vehicle in six to eight hours, standard charger which charges the battery pack in two to three hours, and rapid charger which charges the battery pack in ten to fifteen minutes (fast chargers).

Chargers can also be described as either conductive or inductive. For a conductive charger, the power flow takes place through metal-to-metal contact between the connector on the charge port of the vehicle and charger (off-board charging) or grid (on-board charging). Conductive chargers may have different circuit configurations but the common issues concern safety and the design of the connection interface.

Inductive coupling is a method of transferring power magnetically rather than by direct electrical contact and the technology offers advantages of safety, power compatibility, connector robustness and durability to the users of electric vehicles but on the expense of a lower efficiency and the need of new equipment at charging sites. The electric vehicle user may physically insert the coupler into the vehicle inlet where the ac power is transformer coupled, rectified and fed to the battery, or the charging could be done almost without driver action by wireless charging [13]. For inductive charging, among the most critical parameters are the frequency range, the low magnetizing inductance, the high leakage inductance and the significant discrete parallel capacitance [14].

Different topologies and schemes are reported for both single-phase and three-phase input conductive battery chargers. Usually the three-phase input solutions are used in high power applications [15–19].

## 2.2 Examples of Integrated Motor Drives and Battery Chargers

Fig. 2.1 shows a schematic diagram of a PHEV with parallel configuration (both the internal combustion engine and the electric motor can drive the vehicle simultaneously) as an example of a vehicle with a grid-connected battery charger. The electrical part includes the grid connected battery charger, battery, inverter, motor and control system. It is here assumed that during charging time the vehicle is not driven and during driving time it is not possible to charge the battery pack except for regeneration at braking. In a classical electrical device arrangement in the vehicle, there are separate inverter and charger circuits for traction and charging from an external source. However, it is possible to integrate hardware to reduce the number of system components, space and weight which is equivalent to cost reduction. For instance, the three-phase three-wire boost AC/DC converter that can be used as a battery charger is very similar to what hardware is available in the traction system. See [15, 16] for different AC/DC rectifier schemes. Another example of the use of integration is to use the electric motor windings as inductors in the charger circuit. This reduces weight as high current inductors are large components compared to other components like switches for example. A traction system based on an ac motor and a three-phase inverter is shown in Fig. 2.2. In several

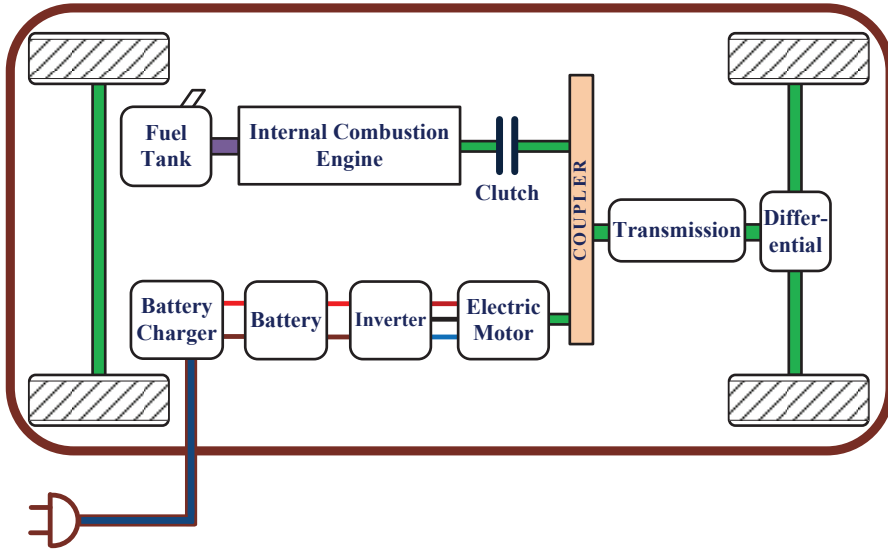


Figure 2.1: A simple diagram of the traction system of a parallel plug-in hybrid electric vehicle.

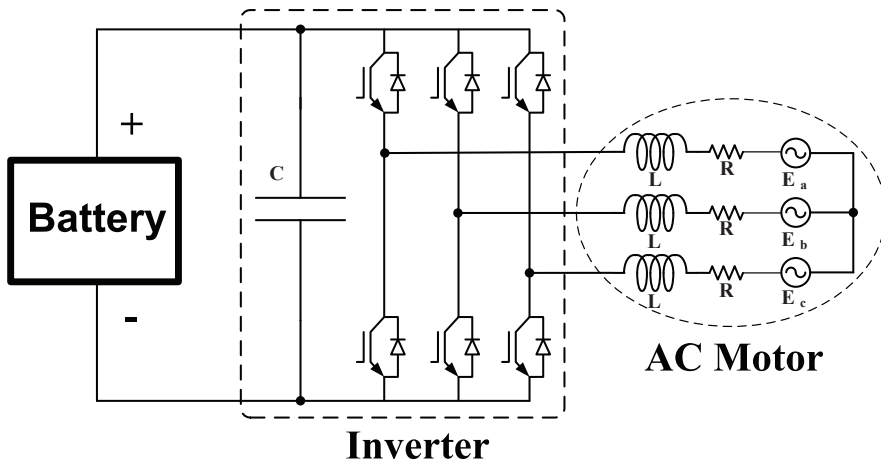


Figure 2.2: Electrical traction in a vehicle based on an ac motor and a three-phase inverter.

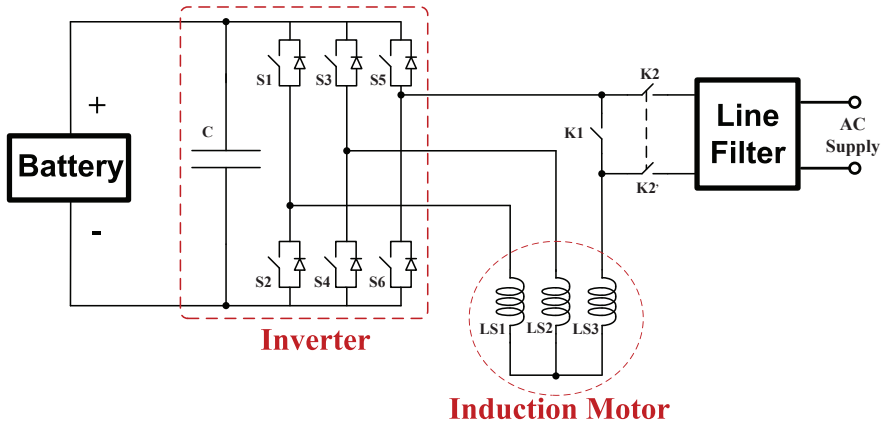


Figure 2.3: Non-isolated single-phase integrated charger based on an induction motor drive system.

schemes a DC/DC converter is used in the system also [20]. The battery power will be transferred to the motor through the inverter. Bi-directional operation of the inverter allows energy restoration to the battery during braking.

Different types of integrated chargers are reported by academia or industry [10, 11, 21–49]. Some of them that are more relevant to the current project are reviewed and compared in this chapter.

### 2.2.1 A Combined Motor Drive and Battery Recharge System Based on an Induction Motor

An integrated motor drive and charger based on an induction machine was patented 1994 by AC Propulsion Inc. [22] and is currently in use in the car industry [50]. The main idea is to use the motor as a set of inductors during charging time to constitute a boost converter with the inverter to have unity power factor operation. Fig. 2.3 shows the functional schematic diagram of this non-isolated integrated charger system. By the means of inexpensive relays the machine windings are reconfigured to be inductors in the charging mode.

For example for a single-phase ac supply, LS2 and LS3 shown in Fig. 2.3 are the induction motor phase to neutral leakage inductances of the windings that act as inductors in the single-phase boost converter circuit. The battery voltage should be more than maximum line-line peak voltage in the input to guarantee unity power factor operation. As an example they used a 336  $V_{dc}$  battery pack with a 220  $V_{ac}$  input. The relays K1, K2 and K2' shown in Fig. 2.3 are used to reconfigure the motor in motoring mode. Further, the inverter switches S1 and S2 are open in charging mode and switches S3-S6 are part of the boost converter. A common/differential mode filter is used to eliminate the switching ripples and spikes from the line side current. Moreover, a lot of electrostatic shielding is used to decrease the ground current and high voltage transitions. In traction mode, relays K2 and K2' are open and K1 is closed, yielding a classical three-phase drive system.

A conventional three-phase pulse width modulation (PWM) scheme is used

in drive mode operation of the system to generate the desired motor speed and torque. In battery charging mode, the PWM scheme with current control is employed to charge the battery with unity power factor capability.

It is possible to have a three-phase input supply with this scheme, but there will be developed torque in the machine during charging that should be considered. The one-phase charger can charge from any source,  $100 - 250 V_{ac}$ , from  $200 W$  up to  $20 kW$  and can be used in vehicle to grid (V2G) applications or for the backup power or energy transfer to other electric vehicles. The filter bank at the front of the ac supply will smooth the harmonic contents of the charger line current.

Other similar alternatives are patented in the US also [23, 24]. In some examples the motor, the inverter and the capacitor components are used in the charging system. All of these solutions are bidirectional non-isolated type of chargers with unity power factor operation and single-phase ac supply. In [23] two solutions are proposed by Rippel in 1990. In traction mode an inverter and a three-phase ac motor is used. In the first version the motor is not used in the charger circuit and instead an inductor is used to be the energy storage device in the front-end boost converter. The inverter switches are used in the system (part of the boost and DC/DC converter). In a later version, the inductors are eliminated and the machine leakage inductances are used as part of the charger circuit. When the machine is used as three inductors, the inductors have self and mutual couplings. So the inductance matrix should be considered in this case. The leakage inductances are the part of inductors that have no coupling to the other inductances. No switching devices like relays are used to reconfigure the circuit for traction and charging mode (with the same hardware in traction and charging mode).

Another solution patented by Rippel and Cocconi in 1992 (the patent assignee is General Motors Inc.) uses the same idea of integration but there are two independent inverters in the system [24]. They proposed two alternative methods. One with two induction motors and another one with one induction motor (with double stator windings).

In the first alternative two induction motors and inverters are used for the traction force. Each motor can be controlled by its dedicated inverter independently. Each motor can be connected to the wheel directly or through a gear that eliminates the need for a transmission and differential in the mechanical system. For the charging mode the supply will be connected to the neutral point of the motors after electro magnetic interference (EMI) filtering.

The second alternative is using an induction motor with double set of stator windings comprising two motor halves. The rotor can be coupled to a single wheel or to two wheels by means of a reduction-differential gear or a transmission-differential gear. Each winding set is connected to an inverter (each winding set includes three windings). In the charging mode the supply is similarly connected to the neutral points of the double set of windings after EMI filtering.

For these two alternatives the detail control scheme is also explained in [24]. Classical PWM control method is used for both the drive and the battery charging mode. In the drive mode, PWM control of each inverter is such that each phase current is maintained proportional to a sinusoidal reference waveform while the three-phase currents are symmetric with 120 degrees phase

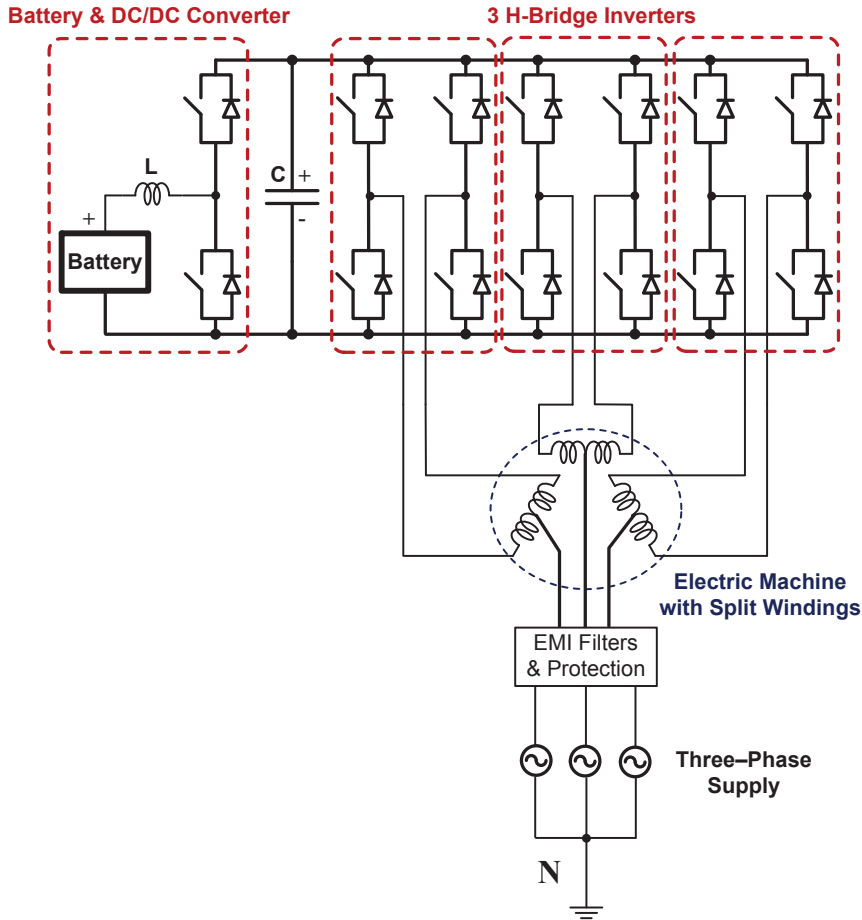


Figure 2.4: Three-phase non-isolated integrated charger based on a split-phase ac motor.

shift. The rotor position, currents of two phases and battery dc voltages are measured and used to generate three-phase reference currents for proper operation of voltage-fed inverters. Each inverter is controlled separately via its own controller. In the battery charging mode, modulation control is such that, within each inverter, one or more of the phase currents are kept close to the sinusoidal reference, which in turn is in phase with input line voltage for unity power factor operation.

### 2.2.2 Non-isolated Integrated Charger Based on a Split-Winding AC Motor

A non-isolated high power three-phase integrated charger is reported by Luis De Sousa et al. in Valeo Engine and Electrical Systems in 2010 [27–29]. Fig. 2.4

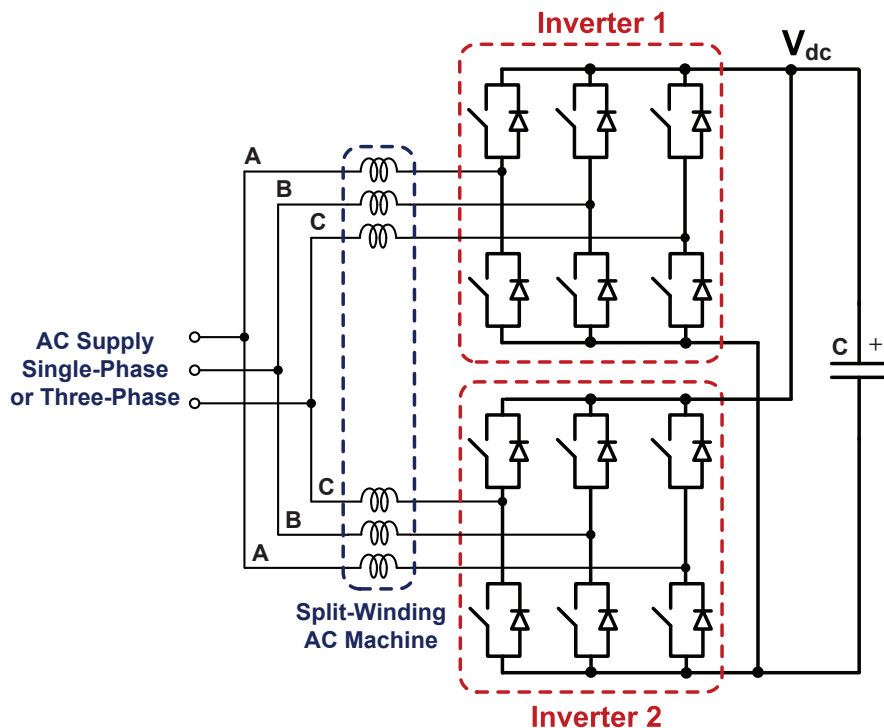


Figure 2.5: Charging mode equivalent circuit of the three-phase integrated charger based on a split-phase ac motor.

shows the proposed integrated charger. In traction mode a 3H-bridge topology is used with a DC/DC converter. The DC/DC converter consists of inductor  $L$  and two switches. The DC/DC converter inductor voltage is  $900 V_{dc}$  while the battery voltage is maximum  $420 V_{dc}$  for the proposed system. With the traction power of  $40 kW$  it is possible to charge the battery with  $30 kW$  power in this proposed scheme.

Fig. 2.5 shows the system equivalent circuit in charging mode. For charging, the three-phase supply is connected to the middle point of the stator windings. A small EMI filter is used to improve the grid current waveforms. As is shown in Fig. 2.5, there are two three-phase boost converters sharing a common dc bus. By using a split-winding configuration and regulating the same current in the same phases of two boost converters, developed stator magnetomotive force (MMF) of the machine is eliminated. So there is not any rotational magnetic field in the motor during charging.

The proposed charger is a high power non-isolated version capable of unity power factor operation. There is no need to use a switch like contactor for the charger to grid connection. A plug can be used for this purpose. Two international patents are granted for the proposed charger [25, 26].

It is shown that it is possible to use the same strategy for a single-phase supply by S. Lacroix et al. [29]. Fig. 2.6 shows the system in charging mode for the single-phase supply. Four legs of bridges in the inverter and inductances

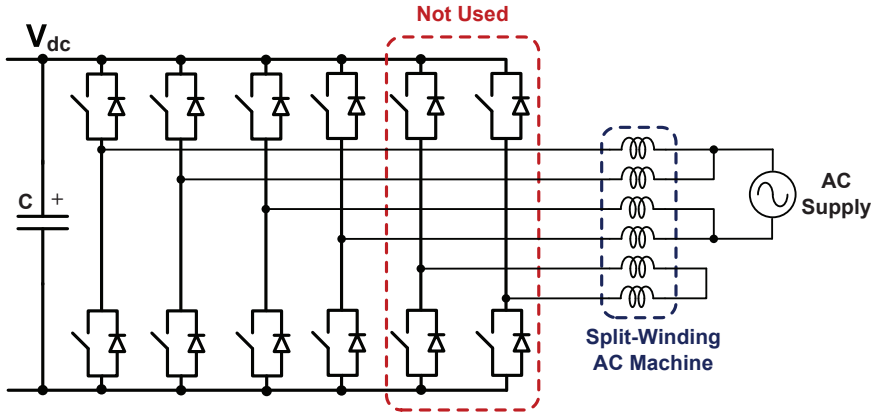


Figure 2.6: Charging mode equivalent circuit of the single-phase integrated charger based on a split-phase ac motor.

of two phases are used in this mode. As is shown in this figure, the third H-bridge inverter is not used. The currents will be regulated to be equal for each phase. Unity power factor operation is possible in this case also due to the boost converter topology.

In both the three-phase and single-phase supply, there are a front-end power factor correction (PFC) stage and a Buck type DC/DC converter. An analogue PFC is implemented in the first version and a digital PFC is under development using one cycle current control scheme [51, 52]. There is no multiplier stage in this control method and few components are used in the controller. For the Buck converter a current controlled PWM method is employed to control the battery charging. The PWM unit switching frequency is 16 kHz in the practical implementation where the system efficiency is more than 93% at a charging power of 3 kW with a single-phase supply.

### 2.2.3 An Integral Battery Charger for a Four-Wheel Drive Electric Vehicle

An integral battery charger has, in 1994, been reported for a four wheel-in motor driven EV by Seung-Ki Sul and Sang-Joon Lee [30]. The propulsion system includes four induction motors and four three-leg inverters with a battery on the system dc bus. By the use of an extra transfer switch the whole system will be reconfigured to a single-phase battery charger. Fig. 2.7 shows the system configuration in traction and charging mode. In traction mode, four inverters connected to the system dc bus drive motors (each motor neutral point is float in this mode). In charging mode (the transfer switch is in position 2) the single-phase ac source is connected between the neutral points of two motors. Utilizing the switches in inverter one and two, this configuration will be a single-phase boost converter with unity power factor operation capability. The third and fourth inverter with the use of two other motors constitute two buck-type converters. Fig. 2.8 shows the system equivalent circuit in charging mode where the motors are used as inductors. For each motor the winding

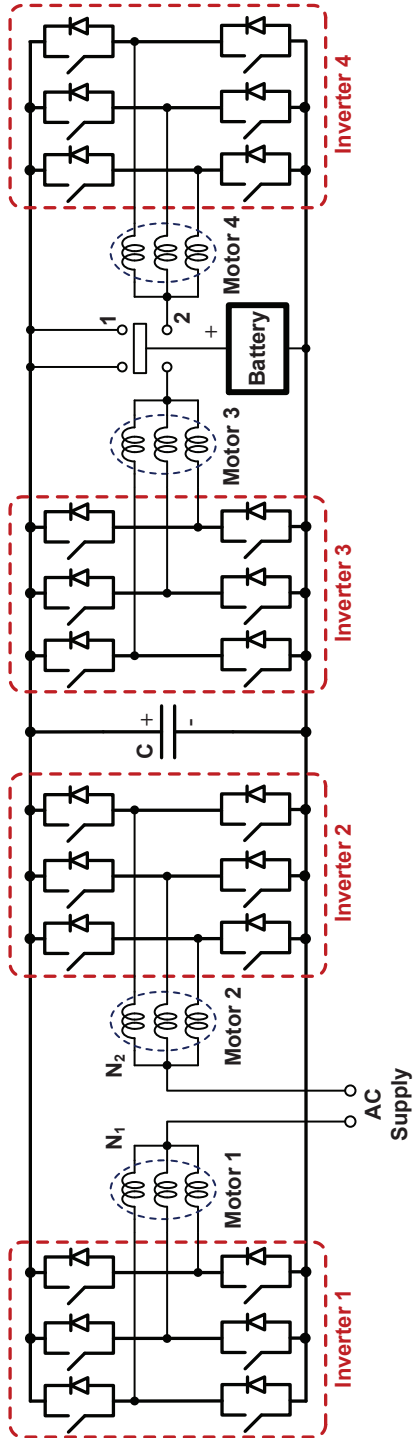


Figure 2.7: Single-phase integrated battery charger for a four wheel drive system.

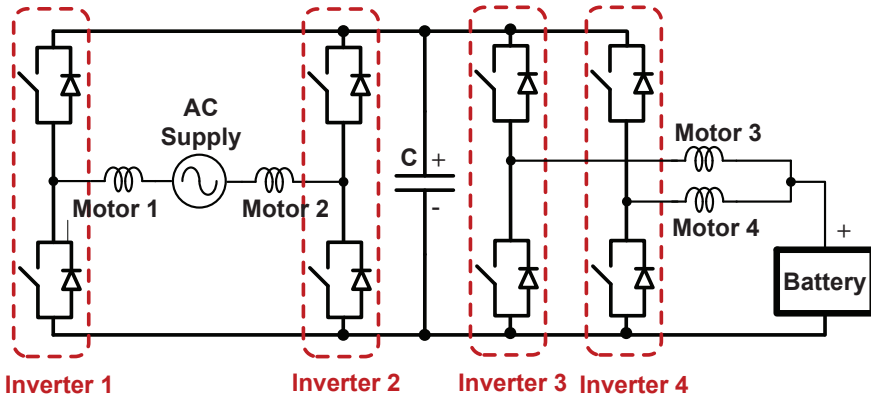


Figure 2.8: System equivalent circuit for the four wheel drive integrated charger during battery charging.

currents are the same for each phase so there is no developed electromagnetic torque in the motors during the charging time. Further, in the charging mode, by controlling the PWM boost converter, the dc link voltage is kept constant. The constant current battery charging profile is achieved by the control of the two buck-type choppers.

For the front-end boost converter, conventional current controlled PWM is employed to have rectification with unity power factor. A PI controller is used to regulate the dc bus voltage. An output feedforward is added to encounter the impact of the input power in current reference determination. The current error is fed to a triangular waveform to generate gate command signals.

A current controlled PWM scheme is also used for the two parallel step-down buck converters. To reduce the dc bus voltage ripple, the triangular wave is inverted in one converter. Moreover, the buck converters have two modes of operation for battery charging: constant current charging mode and constant voltage charging mode. In the experimental setup a PWM frequency of  $5\text{ kHz}$  is used for both the boost converter and the buck converter.

## 2.2.4 An Integrated Charger Based on a PM Motor for an Electric Scooter

A non-isolated single-phase ( $110\text{ V}_{ac}$  and  $60\text{ Hz}$ ) integrated charger for an electrical scooter is another example described in [31]. The authors use the three-phase inverter as a single switch in the charging mode, see Fig. 2.9. Thus, the switches S2, S4 and S6 seen in Fig. 2.9 are to be operated all together as a simple switch. In turn, the circuit is a single-phase boost converter. All three windings of the motor are used in the charging process. A power rectifier and line filter are also used as extra components for the charging operation. It is expected to have unity power factor operation as is expected for boost converters, and low total harmonic distortion (THD) in the ac line current due to use of the line filter. A  $180\text{ V}_{dc}$  lead acid battery ( $12\text{ Ah}$ ) is used as the traction power source and the motor is a  $6\text{ kW}$  axial flux permanent magnet motor. Moreover  $50\text{ A}$  and  $600\text{ V}$  IGBT modules are used with a switching

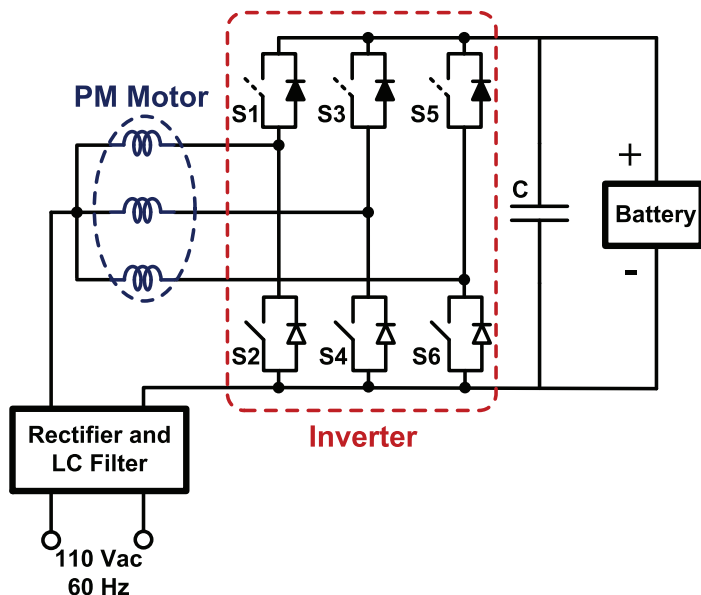


Figure 2.9: Single-phase integrated charger based on a PM motor for an electric scooter.

frequency of  $25\text{ kHz}$ . At charging mode, the motor is used as three parallel connected  $0.1\text{ mH}$  inductors. The currents through the inductances are thus unidirectional, thus no torque is developed in the motor, and the rotor can be at standstill.

To charge the battery, at first constant current is applied by the charger, while the battery voltage progressively rises in this operation. When the battery voltage reaches to a certain level, a constant voltage is applied to the battery as a holding voltage. Discontinuous current mode control is employed for proper charge operation in this system.

### 2.2.5 An Integrated Charger for a Fork Lift Truck

An integrated drive/charger system is reported in 2005 for a fork lift truck [32]. In traction mode a  $6\text{ kW}$  induction machine is used to drive the truck. The battery voltage and rated motor voltage is nominal  $48\text{ V}$ . A three-phase inverter is utilized for motor control based on the space vector modulation (SVM) scheme.

In charging mode (see Fig. 2.10), the motor is used as a low frequency step-down transformer. A wound-type rotor is used in the drive system and for the charging mode the rotor winding is used as a primary side of the transformer that is connected to the three-phase  $400\text{ Vac}$  grid. The stator windings constitute the secondary side of this grid-connected transformer that is connected to the inverter. The inverter serves as a three-phase PWM rectifier for this system in charging mode.

Naturally, there is galvanic insulation between the grid and battery by the means of this transformer. The air-gap in the motor (transformer in charging

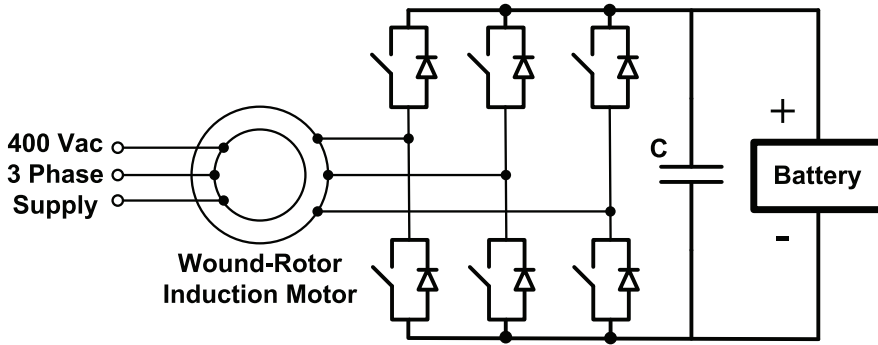


Figure 2.10: Three-phase isolated integrated charger based on a wound-rotor induction motor.

mode) will affect the system performance regarding the loss due to the need of large magnetization currents. Other disadvantages are the extra cost of the wound rotor (compared to a squirrel cage rotor), need of contactors and the need to adapt the motor windings to the charge voltage. Advantages include the possibility of bidirectional power flow, low harmonic distortion and a unit power factor. The rotor is at standstill during charging and a mechanical lock is used.

## 2.2.6 Single-Phase Integrated Charger Based on a Switched Reluctance Motor Drive

Switched reluctance motor (SRM) drive systems are interesting alternatives in vehicle applications due to motor robustness and control simplicity [53–56]. An integrated drive and charger system for a SRM is reported in [33] for an electric vehicle with voltage-boosting and on-board power-factor-corrected-charging capabilities. A boost DC/DC converter is used in the traction mode to boost and regulate the battery voltage for the motor driver. With slight modification of the traction mode, a single-phase non-isolated battery charger is arranged. The DC/DC converter is not used in the charging mode and by the use of a switch the system is reconfigured from charging mode to traction mode and vice versa. Fig. 2.11 shows a simplified diagram of the system in which the power flow in charging mode is through the SRM and its driver to the battery.

The SRM and its driver constitute a single phase buck-boost converter that ensures unity power factor operation. Two windings of the SRM are used as line filter inductors and the third one is used as the energy storage inductor in the buck-boost converter. Initially the battery is charged with a constant current until the voltage rises to a pre-determined voltage level. Afterwards, a constant voltage is applied to the battery as a holding voltage. The current controlled PWM scheme is used to keep the charger current in the continuous conduction mode. PWM switching frequency of  $12.5\text{ kHz}$  is used in the practical set up with  $500\text{ W}$  charging power.

The proposed integrated charger is a complicated solution in both hardware and control implementation. Moreover, the traction system is not fully utilized

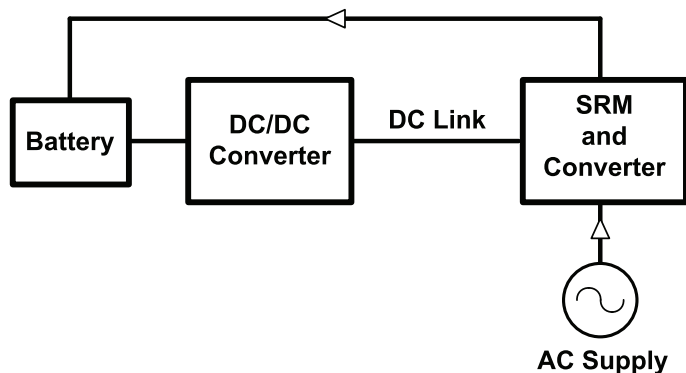


Figure 2.11: Single-phase integrated charger based on a SRM drive system.

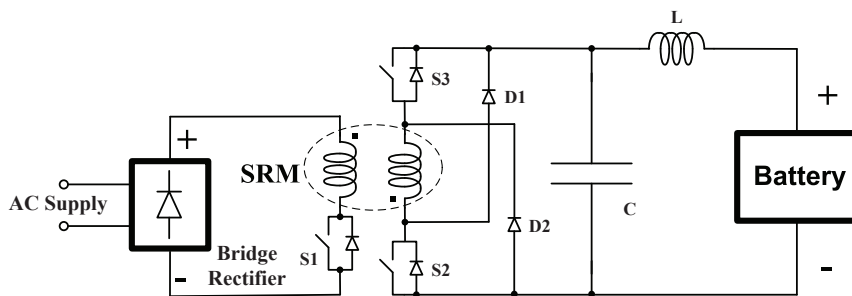


Figure 2.12: Single-phase isolated integrated charger based on a dual converter SRM drive.

in the charger circuit. The DC/DC boost converter and some parts of the SRM and its driver are not used in the charger circuit.

### 2.2.7 Single-Phase Integrated Charger Based on a Dual Converter Switched Reluctance Motor Drive

By adding an extra winding tightly coupled to the switched reluctance stator windings it is possible to use it as a step down transformer. Different versions of single-phase integrated chargers reported by C. Pollock et al. are based on this principle [34–36]. Fig. 2.12 shows a simple basic schematic diagram of the charger. The grid supply is rectified by a diode rectifier module to provide a dc link at the SRM grid side winding (high voltage winding). By switching S1, it is possible to have a flyback converter or a forward converter by the use of the SRM driver converter (switches S2 and S3 including their antiparallel diodes). The SRM grid side windings have more turns compared to its main winding to adjust battery voltage level and grid voltage.

The unity power factor operation is not feasible in this configuration. The machine core losses are high since the switching frequency is high compared to the 50 Hz nominal frequency. So the system efficiency is not high and in one

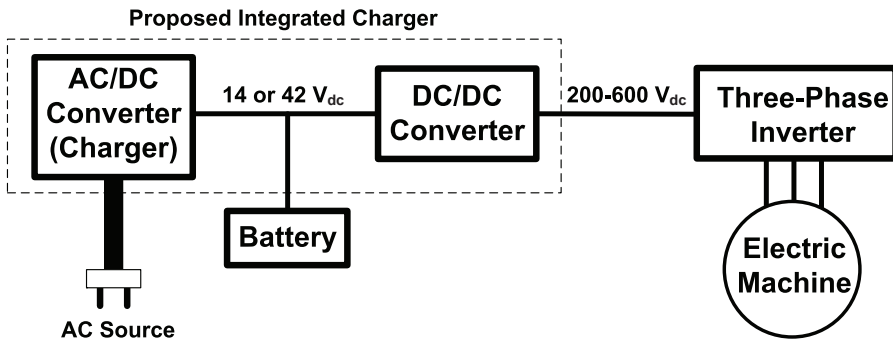


Figure 2.13: System diagram of proposed integrated charger based on the combined bidirectional AC/DC and DC/DC converter.

example it was reported to be 25% [36]. The switching frequency of the flyback converter is  $1.1 \text{ kHz}$  for charge operation. The motor iron lamination is not suitable for high-frequency operation, so an effort is made to keep the switching frequency low. The original application was low power applications like electric shavers, but the topology improved to be used in vehicle application too [36]. The extra winding and switch S1 can drive the machine from the main supply in the electric shaver application.

## 2.2.8 Integrated Bidirectional AC/DC and DC/DC Converter for PHEVs

Conventional hybrid electric vehicles usually have two different voltage levels [57]. A  $14 \text{ V}_{dc}$  bus supplied by a  $12 \text{ V}_{dc}$  battery and a high-voltage  $200 - 600 \text{ V}_{dc}$  bus that provides the propulsion power. Traditional loads like lightning systems and vipers are connected to the low voltage bus. The increasing number of additional loads motivates the car industries to replace the  $14 \text{ V}_{dc}$  bus with a  $42 \text{ V}_{dc}$  bus supplied by a  $36 \text{ V}$  battery [57]. The high voltage and low voltage buses are connected to each other by the means of an isolated bidirectional DC/DC converter. Also, a DC/AC inverter is used to supply and control the AC drive system.

By combining the DC/DC converter and the battery charger (AC/DC converter) an integrated battery charger was proposed by Young-Joo Lee et al. 2009 in [49]. Fig. 2.13 shows a simple schematic diagram of the system structure. Moreover the proposed integrated charger can be identified from this figure. The charger/converter is a non-isolated version with reduced number of inductors and current transducers for the single-phase input supply.

The proposed integrated converter has three modes of operation: battery charging from the grid, boost operation to increase the battery voltage for normal traction operation and braking operation mode to recover braking power in traction mode. The current mode PWM control is used in the system in which the detail control operation is explained in [49].

## 2.2.9 Comparison of Integrated Chargers

Since the reviewed integrated chargers are so different specially in hardware, it is difficult to find a common ground for a comprehensive comparison. A general comparison of before mentioned integrated chargers are presented in Table 2.1 with a short summary. Type of supply (three-phase or single phase), galvanic isolation of the grid, efficiency, and extra components for integration are considered in this comparison. As shown in the table, there is a column called traction component utilization in charger circuit. For a rough comparison of degree of traction/charger integration, a 5 step ranking is used as: poor, fair, average, very good, and excellent. Poor means a separate battery charger is used, and excellent means that the traction circuit can exactly be used as the charger circuit without any change or extra components (fully integrated).

The integrated motor drive and charger based on the induction motor by AC Propulsion Inc., explained in section 2.2.1, is available in the market. For example, at 2008, over 500 units have been used in the BWM Mini E electric vehicle. For the battery charging, the single-phase utility supply is supported that limits the maximum charge power by the available power in the plug. However, a charge power of 20 *kW* is claimed for the device by the manufacturer [50]. Moreover, the charger efficiency is more than 90% for this system at a charge level of 10 *kW*. Another aspect of this system is grid isolation. Since the system is not isolated from the utility grid, extensive shielding and safety issues are required that needs special consideration during the implementation and installation of the system.

The next solution explained in section 2.2.2 is an integrated charger based on the split-phase ac motor, a non-isolated single-phase or three-phase charger. This system is developed by a company in France. The interesting feature of the charger is that there is no extra switch or relay for the winding reconfiguration that makes the operation easier. On the other hand, there are two inverters in the system that reduce the system efficiency and increase the cost. There is a DC/DC converter in the system that provides an easier control of the battery voltage and current with an efficiency and complexity penalty.

The integrated charger for a four-wheel drive EV, section 2.2.3, has a complex structure with many components. It is expected to have a lower system efficiency due to a large number of components compared to a classical boost battery charger, for example.

The integrated charger based on a PM motor and a three-phase inverter proposed for a scooter, explained in section 2.2.4, is an interesting solution because of a low number of components. There is no extra components rather than the traction elements that implies the system has a high efficiency during the battery charging. This charging strategy is a mature solution for the case of a single-phase grid supply.

The isolated integrated charger based on the wound-rotor induction motor presented in section 2.2.4, imposes some limitations in the motor that it should be a wound-rotor type. Moreover, a mechanical lock is needed to hold the motor during the battery charging. Another disadvantage is the system efficiency that can be a low value due to the large airgap in the magnetization path. However, galvanic isolation is an interesting feature in this case.

Other solutions that are based on the SRM, are not commonly used in

Table 2.1: Comparison of integrated charger examples.

Solution	Supply	Isolation	Efficiency	Traction component utilization in charger circuit	Extra components for charging	Comments
A combined motor drive and battery recharge system based on an induction motor (2.2.1)	single-phase or three-phase	non-isolated	high	very good	few relays and a line filter	is currently used in car industry
Non-isolated integrated charger based on a split-winding ac motor (2.2.2)	single-phase or three-phase	non-isolated	high	very good	an extra inverter	will be used in car industry
An integral battery charger for a four-wheel drive electric vehicle (2.2.3)	single-phase	non-isolated	high	very good	a position switch	4 motors and inverters are used in traction mode
An integrated charger based on a PM motor in an electric scooter application(2.2.4)	single-phase	non-isolated	high	very good	a rectifier and a line filter	the battery voltage should be more than peak line voltage
An integrated charger based on a wound-rotor induction motor for a lift truck application (2.2.5)	single-phase or three-phase	isolated	depends on airgap length	very good	mechanical rotor lock	feasible for wound type rotor induction motor
Single-phase integrated charger based on a switched reluctance motor drive (2.2.6)	single-phase	non-isolated	high	fair	a static switch	both hardware and software are complicated
Single-phase integrated charger based on a dual converter switched reluctance motor drive (2.2.7)	single-phase	isolated	low	average	a bridge rectifier	suitable for low power applications
Integrated bidirectional AC/DC and DC/DC converter for PHEVs (2.2.8)	single-phase	non-isolated	high	fair	some power electronics components	hardware is complicated

the car industry. More work is needed for the SRM drive system for vehicle traction. Special converter for the SRM is the main barrier to make it feasible for these applications. However, further studies are required to come over with a realistic solution as an integrated motor drive and battery charger.

The concept of a more electric vehicle brings more integration possibilities within different parts of the electrical system. It turns out that these solutions are based on the heuristic approaches due to the electrical system configuration diversity for different vehicles. An example is presented in section 2.2.8 where the integration is proposed for the 12 V system and the main traction components.



## Chapter 3

# Double dq Modeling of the Split-Phase PM Motor

Multiphase machines have been studied for a long time, but recently they have gained attention in the research community and industry worldwide [58, 59]. The specific application areas are the main motivation of this increased interest. Electric ship propulsion, locomotive traction, electric and hybrid electric vehicles, more-electric aircraft, and high-power industrial applications can be counted as the main applications [58].

It has been shown that multiphase machines have higher efficiency than their three-phase counterparts [58]. Moreover, they naturally have a greater fault tolerance and a lower torque ripple compared to the three-phase systems [59]. Another advantage is reduced power electronics component rating that still is a challenge in high-power applications. In this respect, they can be used as an alternative to the systems using multi-level converters [59, 60].

For the multi-phase machines with  $n$  set of windings by using Clarke's transformation, the machine equations are decoupled into new variables [59]. If all windings are connected to the same neutral point, the order of equation can be reduced by one when the machine is supplied by a symmetrical voltage waveform [58]. There are fundamental components,  $dq$ , and higher order harmonic components in the obtained model enabling torque production using high-order harmonic variables as well as fundamental frequency components [59]. However, for the machines that have multiple three-phase windings with isolated neutral points, i.e. a machine with 3,6,9,... phases, another approach can be used, which comprises a reduced number of variables [58, 59, 61]. If each three-phase winding has an independent neutral point, two variables are enough to model each three-phase winding that can be separate  $dq$  variables for example. A machine with double set of three-phase windings is a typical example of using this double  $dq$  technique for modeling and control. A motor with double set of shifted three-phase windings has many names like split-phase, dual three-phase, double-star, dual-stator, and so on in which the first one is used in this thesis.

In the split-phase PM motor, each phase winding is divided into two equivalent parts and are shifted symmetrically around the stator periphery. Basically there will be six windings inside the stator instead of three for a two

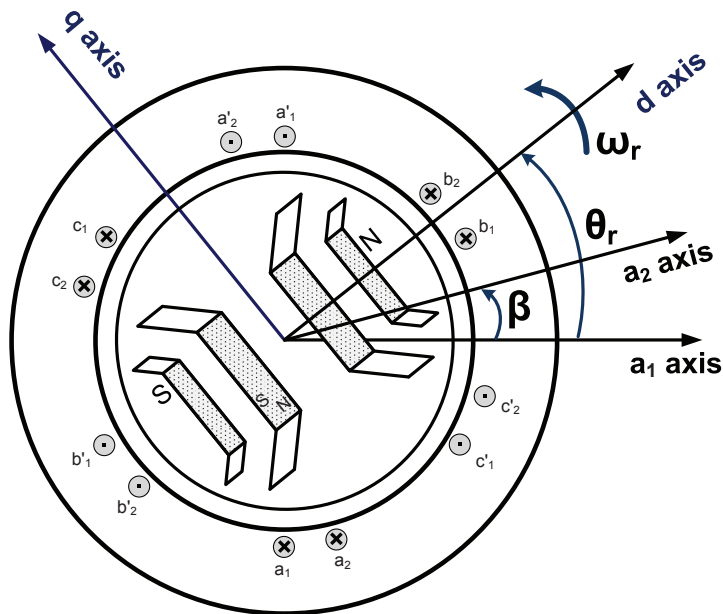


Figure 3.1: Cross section area of a split-phase PM motor with an arbitrary phase-shift angle between two sets of three-phase windings.

pole machine. These six windings can be considered as two sets of three-phase windings that are shifted. A double  $dq$  model of the split-phase PM motor is presented in this chapter including the motor dynamical equations. The presented model is the main theoretical framework for the rest of this thesis.

### 3.1 Voltage and Flux Equations

Fig. 3.1 shows the cross section of a PM motor with split windings in the stator. The motor is a PM type that can be a permanent magnet synchronous motor (PMSM), interior permanent magnet synchronous motor (IPMSM) or PM assisted type. The model is developed for IPMSM as a general case since it can be used for PMSM or PM assisted also. As is shown in this figure, there are six windings while the rotor has a two-pole configuration. These six windings can be considered as two sets of three-phase windings. Say that  $a_1$ ,  $b_1$  and  $c_1$  are the first set of windings (the same as classical three-phase windings) and  $a_2$ ,  $b_2$  and  $c_2$  are the second set of three-phase windings. These two sets of three-phase windings are shifted  $\beta$  electrical degrees (the angle between the magnetic axis of  $a'_1 a_1$  and  $a'_2 a_2$ ) where  $\beta$  is an arbitrary angle. For a phase shift of  $\pi/6$  the detailed modeling and dynamical equations are described in [62].

The voltage equations for six windings can be described by the following equations [62] as

$$v_{a_1} = r_s i_{a_1} + \frac{d}{dt} \psi_{a_1} \quad (3.1)$$

$$v_{b_1} = r_s i_{b_1} + \frac{d}{dt} \psi_{b_1} \quad (3.2)$$

$$v_{c_1} = r_s i_{c_1} + \frac{d}{dt} \psi_{c_1} \quad (3.3)$$

$$v_{a_2} = r_s i_{a_2} + \frac{d}{dt} \psi_{a_2} \quad (3.4)$$

$$v_{b_2} = r_s i_{b_2} + \frac{d}{dt} \psi_{b_2} \quad (3.5)$$

$$v_{c_2} = r_s i_{c_2} + \frac{d}{dt} \psi_{c_2} \quad (3.6)$$

where  $v_{a_1}$ ,  $v_{b_1}$ ,  $v_{c_1}$ ,  $v_{a_2}$ ,  $v_{b_2}$ ,  $v_{c_2}$ ,  $i_{a_1}$ ,  $i_{b_1}$ ,  $i_{c_1}$ ,  $i_{a_2}$ ,  $i_{b_2}$ ,  $i_{c_2}$ ,  $\psi_{a_1}$ ,  $\psi_{b_1}$ ,  $\psi_{c_1}$ ,  $\psi_{a_2}$ ,  $\psi_{b_2}$ ,  $\psi_{c_2}$  and  $r_s$  are windings voltages, currents, flux linkages and resistance subsequently.

The windings' flux linkages can be expressed as

$$\psi_{a_1} = L_{a_1 a_1} i_{a_1} + L_{a_1 b_1} i_{b_1} + L_{a_1 c_1} i_{c_1} + L_{a_1 a_2} i_{a_2} + L_{a_1 b_2} i_{b_2} + L_{a_1 c_2} i_{c_2} + \psi_{pm} \cos(\theta_r) \quad (3.7)$$

$$\psi_{b_1} = L_{b_1 a_1} i_{a_1} + L_{b_1 b_1} i_{b_1} + L_{b_1 c_1} i_{c_1} + L_{b_1 a_2} i_{a_2} + L_{b_1 b_2} i_{b_2} + L_{b_1 c_2} i_{c_2} + \psi_{pm} \cos(\theta_r - \frac{2\pi}{3}) \quad (3.8)$$

$$\psi_{c_1} = L_{c_1 a_1} i_{a_1} + L_{c_1 b_1} i_{b_1} + L_{c_1 c_1} i_{c_1} + L_{c_1 a_2} i_{a_2} + L_{c_1 b_2} i_{b_2} + L_{c_1 c_2} i_{c_2} + \psi_{pm} \cos(\theta_r + \frac{2\pi}{3}) \quad (3.9)$$

$$\psi_{a_2} = L_{a_2 a_1} i_{a_1} + L_{a_2 b_1} i_{b_1} + L_{a_2 c_1} i_{c_1} + L_{a_2 a_2} i_{a_2} + L_{a_2 b_2} i_{b_2} + L_{a_2 c_2} i_{c_2} + \psi_{pm} \cos(\theta_r - \beta) \quad (3.10)$$

$$\psi_{b_2} = L_{b_2 a_1} i_{a_1} + L_{b_2 b_1} i_{b_1} + L_{b_2 c_1} i_{c_1} + L_{b_2 a_2} i_{a_2} + L_{b_2 b_2} i_{b_2} + L_{b_2 c_2} i_{c_2} + \psi_{pm} \cos(\theta_r - \frac{2\pi}{3} - \beta) \quad (3.11)$$

$$\psi_{c_2} = L_{c_2 a_1} i_{a_1} + L_{c_2 b_1} i_{b_1} + L_{c_2 c_1} i_{c_1} + L_{c_2 a_2} i_{a_2} + L_{c_2 b_2} i_{b_2} + L_{c_2 c_2} i_{c_2} + \psi_{pm} \cos(\theta_r + \frac{2\pi}{3} - \beta) \quad (3.12)$$

where  $L_{a_1 a_1}$ ,  $L_{b_1 b_1}$ ,  $L_{c_1 c_1}$ ,  $L_{a_2 a_2}$ ,  $L_{b_2 b_2}$  and  $L_{c_2 c_2}$  are the self inductances of the windings. Moreover,  $L_{a_1 b_1}$ ,  $L_{a_1 c_1}$ ,  $L_{a_1 a_2}$ ,  $L_{a_1 b_2}$ ,  $L_{a_1 c_2}$ ,  $L_{b_1 b_2}$ ,  $L_{b_1 c_2}$ ,  $L_{c_1 b_2}$ ,  $L_{a_2 b_2}$ ,  $L_{a_2 c_2}$  and  $L_{b_2 c_2}$  are windings' mutual inductances.  $\psi_{pm}$  is the permanent magnet flux (the rotor flux) and  $\theta_r$  is the angle between the rotor d axis and the magnetic axes of winding  $a'_1 a_1$ .

## 3.2 Inductances as the Function of Rotor Position

The inductance values are calculates as

$$L_{a_1 a_1} = L_{ls} + \bar{L}_m - L_{\Delta m} \cos(2\theta_r) \quad (3.13)$$

$$L_{a_1 b_1} = L_{b_1 a_1} = -\frac{1}{2}\bar{L}_m - L_{\Delta m} \cos 2(\theta_r - \frac{\pi}{3}) \quad (3.14)$$

$$L_{a_1 c_1} = L_{c_1 a_1} = -\frac{1}{2}\bar{L}_m - L_{\Delta m} \cos 2(\theta_r + \frac{\pi}{3}) \quad (3.15)$$

$$L_{a_1 a_2} = L_{a_2 a_1} = \cos \beta \bar{L}_m - L_{\Delta m} \cos 2(\theta_r - \frac{\beta}{2}) \quad (3.16)$$

$$L_{a_1 b_2} = L_{b_2 a_1} = \cos(\frac{2\pi}{3} + \beta) \bar{L}_m - L_{\Delta m} \cos 2(\theta_r - \frac{\pi}{3} + \frac{\beta}{2}) \quad (3.17)$$

$$L_{a_1 c_2} = L_{c_2 a_1} = \cos(\frac{4\pi}{3} + \beta) \bar{L}_m - L_{\Delta m} \cos 2(\theta_r - \frac{2\pi}{3} - \frac{\beta}{2}) \quad (3.18)$$

$$L_{b_1 b_1} = L_{l_s} + \bar{L}_m - L_{\Delta m} \cos 2(\theta_r - \frac{2\pi}{3}) \quad (3.19)$$

$$L_{b_1 c_1} = L_{c_1 b_1} = -\frac{1}{2}\bar{L}_m - L_{\Delta m} \cos 2\theta_r \quad (3.20)$$

$$L_{b_1 a_2} = L_{a_2 b_1} = \cos(\frac{2\pi}{3} - \beta) \bar{L}_m - L_{\Delta m} \cos 2(\theta_r - \frac{\pi}{3} - \frac{\beta}{2}) \quad (3.21)$$

$$L_{b_1 b_2} = L_{b_2 b_1} = \cos \beta \bar{L}_m - L_{\Delta m} \cos 2(\theta_r - \frac{2\pi}{3} - \frac{\beta}{2}) \quad (3.22)$$

$$L_{b_1 c_2} = L_{c_2 b_1} = \cos(\frac{2\pi}{3} + \beta) \bar{L}_m - L_{\Delta m} \cos 2(\theta_r - \frac{\beta}{2}) \quad (3.23)$$

$$L_{c_1 c_1} = L_{l_s} + \bar{L}_m - L_{\Delta m} \cos 2(\theta_r + \frac{2\pi}{3}) \quad (3.24)$$

$$L_{c_1 a_2} = L_{a_2 c_1} = \cos(\frac{2\pi}{3} + \beta) \bar{L}_m - L_{\Delta m} \cos 2(\theta_r - \frac{2\pi}{3} - \frac{\beta}{2}) \quad (3.25)$$

$$L_{c_1 b_2} = L_{b_2 c_1} = \cos(\frac{2\pi}{3} - \beta) \bar{L}_m - L_{\Delta m} \cos 2(\theta_r - \frac{\beta}{2}) \quad (3.26)$$

$$L_{c_1 c_2} = L_{c_2 c_1} = \cos \beta \bar{L}_m - L_{\Delta m} \cos 2(\theta_r - \frac{\pi}{3} - \frac{\beta}{2}) \quad (3.27)$$

$$L_{a_2 a_2} = L_{l_s} + \bar{L}_m - L_{\Delta m} \cos 2(\theta_r - \beta) \quad (3.28)$$

$$L_{a_2 b_2} = L_{b_2 a_2} = -\frac{1}{2}\bar{L}_m - L_{\Delta m} \cos 2(\theta_r - \frac{\pi}{3} - \beta) \quad (3.29)$$

$$L_{a_2 c_2} = L_{c_2 a_2} = -\frac{1}{2}\bar{L}_m - L_{\Delta m} \cos 2(\theta_r - \frac{2\pi}{3} - \beta) \quad (3.30)$$

$$L_{b_2 b_2} = L_{l_s} + \bar{L}_m - L_{\Delta m} \cos 2(\theta_r - \frac{2\pi}{3} - \beta) \quad (3.31)$$

$$L_{b_2 c_2} = L_{c_2 b_2} = -\frac{1}{2}\bar{L}_m - L_{\Delta m} \cos 2(\theta_r - \beta) \quad (3.32)$$

$$L_{c_2 c_2} = L_{l_s} + \bar{L}_m - L_{\Delta m} \cos 2(\theta_r - \frac{2\pi}{3} - \beta) \quad (3.33)$$

where  $\bar{L}_m$ ,  $L_{\Delta m}$  and  $L_{l_s}$  are average value of the magnetization inductance, half-amplitude of the sinusoidal variation of the magnetization inductance and

the leakage inductance of each winding. It is assumed that all windings have the same number of turns.

If the  $6 \times 6$  inductance matrix, the  $6 \times 1$  current vector, the  $6 \times 1$  voltage vector, the  $6 \times 1$  flux vector, and the  $6 \times 6$  resistance matrix are defined as

$$\mathbf{L}_s = \begin{bmatrix} L_{a_1 a_1} & L_{a_1 b_1} & \dots & L_{a_1 c_2} \\ L_{b_1 a_1} & L_{b_1 b_1} & \dots & L_{b_1 c_2} \\ \dots & \dots & \dots & \dots \\ L_{c_2 a_1} & L_{c_2 b_1} & \dots & L_{c_2 c_2} \end{bmatrix},$$

$$\mathbf{i}_s = [i_{a_1} \quad i_{b_1} \quad i_{c_1} \quad i_{a_2} \quad i_{b_2} \quad i_{c_2}]^T,$$

$$\mathbf{v}_s = [v_{a_1} \quad v_{b_1} \quad v_{c_1} \quad v_{a_2} \quad v_{b_2} \quad v_{c_2}]^T,$$

$$\psi_s = [\psi_{a_1} \quad \psi_{b_1} \quad \psi_{c_1} \quad \psi_{a_2} \quad \psi_{b_2} \quad \psi_{c_2}]^T \text{ and}$$

$\mathbf{R}_s = r_s I_6$ , where  $I_6$  is the  $6 \times 6$  identity matrix, the voltage and flux equations can be written as [63]

$$\mathbf{v}_s = \mathbf{R}_s \mathbf{i}_s + \frac{d}{dt} \psi_s. \quad (3.34)$$

### 3.3 Electromagnetic Torque and Mechanical Dynamics

The developed electromagnetic torque in the machine can be calculated as [63]

$$T_e = \frac{P}{2} \left( \frac{1}{2} \mathbf{i}_s^T \frac{\partial \mathbf{L}_s}{\partial \theta_r} \mathbf{i}_s + \mathbf{i}_s^T \frac{\partial \psi_{pm}}{\partial \theta_r} \right) \quad (3.35)$$

where  $P$  is the machine number of poles and  $\psi_{pm}$  is stator winding fluxes due to rotor magnets. The mechanical dynamical equations describing the machine are

$$\frac{d\omega_r}{dt} = \frac{P}{2J} \left( T_e - \frac{2B_m}{P} \omega_r - T_L \right) \quad (3.36)$$

$$\frac{d\theta_r}{dt} = \omega_r \quad (3.37)$$

where  $J$ ,  $B_m$ ,  $T_L$  and  $\omega_r$  are the moment of inertia, viscous friction coefficient, load torque and speed of the machine.

### 3.4 Extended Park Transformation

To simplify the machine equations a special version of the Park transformation (it is called extended Park transformation here) is used to reduce the system order and remove all sinusoidal terms. The transformation matrix,  $\mathbf{K}_s$ , is applied to machine equations to transform them to the synchronous  $dq0$  reference frame. This matrix is defined as

$$\mathbf{K}_s = \frac{2}{3} \begin{bmatrix} \cos\theta_r & \cos(\theta_r - \frac{2\pi}{3}) & \cos(\theta_r + \frac{2\pi}{3}) & \dots \\ -\sin\theta_r & -\sin(\theta_r - \frac{2\pi}{3}) & -\sin(\theta_r + \frac{2\pi}{3}) & \dots \\ \frac{1}{2} & \frac{1}{2} & \frac{1}{2} & \dots \\ 0 & 0 & 0 & \dots \\ 0 & 0 & 0 & \dots \\ 0 & 0 & 0 & \dots \end{bmatrix}$$

$$\begin{bmatrix} 0 & 0 & 0 \\ 0 & 0 & 0 \\ 0 & 0 & 0 \\ \cos(\theta_r - \beta) & \cos(\theta_r - \frac{2\pi}{3} - \beta) & \cos(\theta_r + \frac{2\pi}{3} - \beta) \\ -\sin(\theta_r - \beta) & -\sin(\theta_r - \frac{2\pi}{3} - \beta) & -\sin(\theta_r + \frac{2\pi}{3} - \beta) \\ \frac{1}{2} & \frac{1}{2} & \frac{1}{2} \end{bmatrix}.$$

The inverse of the matrix  $\mathbf{K}_s, \mathbf{K}_s^{-1}$ , can be calculated as

$$\mathbf{K}_s^{-1} = \begin{bmatrix} \cos\theta_r & -\sin\theta_r & 1 & \dots \\ \cos(\theta_r - \frac{2\pi}{3}) & -\sin(\theta_r - \frac{2\pi}{3}) & 1 & \dots \\ \cos(\theta_r + \frac{2\pi}{3}) & -\sin(\theta_r + \frac{2\pi}{3}) & 1 & \dots \\ 0 & 0 & 0 & \dots \\ \cos(\theta_r - \beta) & -\sin(\theta_r - \beta) & 1 & \dots \\ \cos(\theta_r - \frac{2\pi}{3} - \beta) & -\sin(\theta_r - \frac{2\pi}{3} - \beta) & 1 & \dots \\ \cos(\theta_r + \frac{2\pi}{3} - \beta) & -\sin(\theta_r + \frac{2\pi}{3} - \beta) & 1 & \dots \end{bmatrix}.$$

### 3.5 Dynamical Equations in the dq Reference Frame

By transforming the phase variables to the rotor reference frame by applying the transformation matrix  $\mathbf{K}_s$ , the machine equations will be simplified with a reduced number of equations. In the rotor reference frame, the variables are superscripted by the letter  $r$  and are defined as

$$\begin{aligned} \mathbf{i}_s^r &= [ i_{d_1} \quad i_{q_1} \quad i_{0_1} \quad i_{d_2} \quad i_{q_2} \quad i_{0_2} ]^T, \\ \mathbf{v}_s^r &= [ v_{d_1} \quad v_{q_1} \quad v_{0_1} \quad v_{d_2} \quad v_{q_2} \quad v_{0_2} ]^T \text{ and} \\ \boldsymbol{\psi}_s^r &= [ \psi_{d_1} \quad \psi_{q_1} \quad \psi_{0_1} \quad \psi_{d_2} \quad \psi_{q_2} \quad \psi_{0_2} ]^T. \end{aligned}$$

The indexes  $d$ ,  $q$  and  $0$  denote the direct axis, quadrature axis and zero component of the variables. Moreover, there are two sets of three-phase quantities that are denoted by the numbers 1 and 2 respectively. For example the voltage can be transformed from the abc domain to the  $dq$  domain by  $\mathbf{v}_s^r = \mathbf{K}_s \mathbf{v}_s$ .

By transforming machine voltage, flux linkage and torque equations to the  $dq$  reference frame, the equations (3.38-3.46) describe the dynamical model.

The dynamic model of the electrical part of this machine with split-phase stator windings can be described by the following equations [62] as is calculated above:

$$v_{d_1} = r_s i_{d_1} + \frac{d}{dt} \psi_{d_1} - \omega_r \psi_{q_1} \quad (3.38)$$

$$v_{q_1} = r_s i_{q_1} + \frac{d}{dt} \psi_{q_1} + \omega_r \psi_{d_1} \quad (3.39)$$

$$v_{d_2} = r_s i_{d_2} + \frac{d}{dt} \psi_{d_2} - \omega_r \psi_{q_2} \quad (3.40)$$

$$v_{q_2} = r_s i_{q_2} + \frac{d}{dt} \psi_{q_2} + \omega_r \psi_{d_2} \quad (3.41)$$

$$\psi_{d_1} = L_d i_{d_1} + L_{md} i_{d_2} + \psi_{pm} \quad (3.42)$$

$$\psi_{q_1} = L_q i_{q_1} + L_{mq} i_{q_2} \quad (3.43)$$

$$\psi_{d_2} = L_{md} i_{d_1} + L_d i_{d_2} + \psi_{pm} \quad (3.44)$$

$$\psi_{q_2} = L_{mq} i_{q_1} + L_q i_{q_2} \quad (3.45)$$

where  $L_d$ ,  $L_q$ ,  $L_{md}$ ,  $L_{mq}$  are the direct and quadrature axis winding self and mutual inductances, respectively. Moreover,  $L_d = L_l + L_{md}$  and  $L_q = L_l + L_{mq}$ . It is assumed that the zero components are zero due to symmetrical three-phase quantities.

The developed electromagnetic torque can be expressed as

$$T_e = \frac{3P}{2} [\psi_{pm}(i_{q_1} + i_{q_2}) + (L_d - L_q)(i_{d_1} i_{q_1} + i_{d_1} i_{q_2} + i_{d_2} i_{q_1} + i_{d_2} i_{q_2})]. \quad (3.46)$$

For a PMSM,  $L_d = L_q$  so the developed electromagnetic torque simplifies to

$$T_e = \frac{3P}{2} \psi_{pm}(i_{q_1} + i_{q_2}). \quad (3.47)$$



## Chapter 4

# An Isolated Integrated Charger Based on the Split-Phase PM Motor

An integrated motor drive and isolated battery charger based on a split-phase PM motor is presented in this chapter. The proposed charger is a high-power bidirectional device that can operate with unity power factor. The system functionality in both traction and charging, simulation results and practical implementation is presented in this chapter.

### 4.1 Proposed Isolated Integrated Charger

Fig. 4.1 shows the power stage of a three-phase non-isolated boost rectifier [64]. This circuit topology is one of the well-known schemes used for battery charging applications [18, 65]. Comparing this circuit to the traction circuit, Fig. 2.2, it implies that they are very similar. If the motor in Fig. 2.2 is replaced by a three-phase source and series-connected inductors, then the two schemes are identical. The purpose of the proposed integrated charger is thus to reconfigure the motor windings to emulate a three-phase source with three series-connected inductors for the inverter to constitute a three-phase boost battery charger.

Further, by reconfiguration of the electric motor windings, an integrated charger scheme is proposed where the machine is used as a special grid connected generator. The main idea is to introduce a multi terminal device called motor/generator set to act like a motor in traction mode and like an isolated generator/transformer in charging mode. The so called motor/generator acts as an isolated three-phase power source after synchronization with the utility grid in charging mode. All machine windings are used in traction mode and are then reconnected in charging mode through a simple switching device.

Fig. 4.2 shows a simple schematic diagram of this integrated motor drive and isolated battery charger for a PHEV first proposed in [8]. Different motor topologies are possible both concerning motor types and winding arrangements. One option with an internal permanent magnet synchronous motor



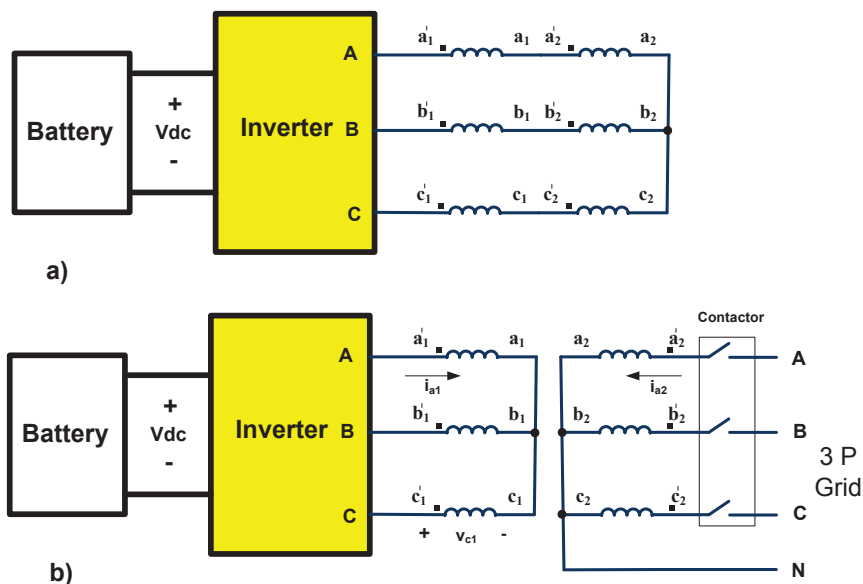


Figure 4.3: Circuit diagram of the proposed isolated integrated charger for a conceptual two pole motor: (a) traction mode and (b) charging mode.

voltage source and the inverter can control the dc voltage and current at the battery side. One control objective is to keep the motor stable during the charge operation while rotating at synchronous speed. Another control objective is unity power factor operation.

To have proper boost converter operation, the dc bus voltage should be more than the peak ac line voltage. This can be solved in two ways: using an extra DC/DC converter or  $Y - \Delta$  connection of the stator windings to reduce the voltage at the inverter side. The second approach has been selected to reduce the system hardware in this case [66].

## 4.2 System Operation in Traction and Charging

In a two-pole three-phase PM motor there are three windings in the stator shifted 120 electrical degrees [63]. For the proposed integrated charger each phase winding is divided into two equivalent parts and moreover they might be shifted symmetrically around the stator periphery. Basically there will be six windings inside the stator instead of three for a two pole machine that is called a split-phase motor. These six windings can be considered as two sets of three-phase windings. Let say  $a_1$ ,  $b_1$  and  $c_1$  are the first set of windings (the same as classical three-phase windings) and  $a_2$ ,  $b_2$  and  $c_2$  are the second set of three-phase windings. An electro mechanical model of the split-phase PM motor is presented in the previous chapter.

Fig. 4.3 shows the system in traction and charging modes for a conceptual two pole machine. In traction mode, each two windings are connected in

series to constitute a three-phase winding set. These three windings can be connected in  $\Delta$  or Y to form a classical three-phase machine. Moreover, the motor is powered by the battery through the inverter. Fig. 4.3.a shows the system diagram in this mode. Sensorless schemes for example can be employed to run the motor in traction mode [67, 68]. For the charging mode, the system is reconfigured according to the scheme shown in Fig. 4.3.b. A simple relay based device re-connects the windings and a contactor is needed to connect the system to the utility grid.

If the machine would be kept in standstill as in [32], the magnetization current will be high due to the air-gap. So it is expected to have lower system efficiency depending on the air-gap length. However, if the machine rotates with the grid synchronous speed, the magnets will induce voltages in the inverter-side windings that emulates an isolated PM ac generator for the inverter. The idea is thus to connect the machine to the grid via the grid-side three-phase windings,  $a_2$ ,  $b_2$  and  $c_2$ . These three windings can be used to run the machine as a classical motor. The inverter side windings,  $a_1$ ,  $b_1$  and  $c_1$  pick up the induced voltage due to the developed flux inside the machine (since they are located on the same pole-pair as are the grid-side windings). The inverter uses this isolated voltage source to charge the battery by the means of machine leakage inductances as the converter energy storage component (yielding a three-phase boost converter).

#### 4.2.1 Grid Synchronization and Battery Charge Control

Assume that the vehicle is parked, the engine and electric motor are turned off, and the clutch between the electric machine and mechanical transmission is opened before charging. Moreover, the machine windings are reconfigured by the switching device to charging mode as is shown in Fig. 4.3.b. At first the grid contactor is open and the motor is in stand still. Then, the electric motor starts to rotate at the synchronous speed by the proper inverter control action. The dc link voltage, motor/generator primary-side currents (two phases), and the rotor position are measured to have a classical FOC of the PM motor [69]. The speed signal is estimated using a trigonometric estimator which is explained later on. Hence, it is assumed that accurate position and speed signals are available.

The two sets of the three-phase windings share the same magnetic path, hence the second set of windings, connected to the contactor, have induced voltages while the motor is rotating by the proper inverter operation. To be able to close the contactor, the grid voltage and the motor/generator secondary side windings voltage should be equal in both magnitude and phase. It is possible to control the voltage magnitude by adjusting the motor flux level that is control of  $i_d$ . Nevertheless, it is assumed that the motor back EMF is equal to the grid voltage at the synchronous speed. By controlling the motor speed, it is possible to change the voltage phase.

After closing the contactor, the grid voltage is forced on the secondary side windings of the motor/generator. Now, it is possible to transfer active and reactive power between the grid and motor/generator in both directions. However, in this application just the active power transfer is considered. In this way, the vehicle battery is charged and that is called battery charge control.

Fig. 4.4 shows the control strategy of the system in the battery charging mode. There is a virtual switch indicating the grid synchronization or charge control modes. After winding reconnection, the switch is positioned in the synchronization mode and the grid contactor is off. In this case the system is like a normal FOC based speed control system, but there is no mechanical load. The dc bus voltage, two phase motor currents,  $i_{A1}$  and  $i_{B1}$ , and the rotor position are measured for the speed control. The speed is estimated by using a trigonometric estimator developed for this application. Nevertheless, the grid voltage and motor voltage are measured too for the sake of synchronization. After the grid synchronization and closing the contactor, the switch will be placed in position 2 automatically (in software) for battery charging. The charge power is controlled by a predefined reference value of  $i_{qch}^*$  that is explained in the following.

In the FOC of the PM motor, there is one speed  $PI$  control loop that determines the required reference values for the  $dq$  components of the current. Basically, the speed control  $PI$  output is the motor torque requirement. The  $dq$  current reference values are specified according to the motor type and control strategy in response to the requested torque. For example, it can be an online calculation or a switching table search approach. For this application, the reference value for the  $d$  component of the current is set to zero in the charging mode because it is assumed that the motor back EMF is equal to the grid voltage and there is no need to adjust the motor flux level. The zero  $d$  current means that the motor reluctance torque is not utilized in battery charging mode, which is not necessary because there is no mechanical load connected to the shaft. Moreover, this simplifies the controller for the practical implementation.

There are two  $PI$  controllers to regulate the currents,  $i_{d1}$  and  $i_{q1}$ . The aim of the control is to regulate the  $dq$  components of the motor currents according to the reference values determined by the control strategy in response to the speed control loop. To summarize the control strategy to determine the reference values,  $i_{d1}$  is set to zero and  $i_{q1}$  is determined by some control action that is different for the grid synchronization and battery charge control. Moreover, there are feedforward terms modifying the current controllers outputs to enhance the control performance. The output is a reference value of the voltage in the rotor reference frame ( $v_{d1}^*$  and  $v_{q1}^*$ ). The  $dq$  voltages are transformed to  $\alpha\beta$  quantities by using the rotor position and the before mentioned Park transformation to provide  $v_{\alpha1}^*$  and  $v_{\beta1}^*$  for the inverter.

For the grid synchronization, the drive system rotates the motor at the synchronous speed. The produced voltage at the second set of windings,  $v_{a2}$ ,  $v_{b2}$  and  $v_{c2}$ , are ideally the same as grid voltage,  $v_{ag}$ ,  $v_{bg}$  and  $v_{cg}$ , in magnitude. To synchronize the two sets of voltages, they are transformed to  $dq$  values regarding the rotor position. The  $d$  component of the voltages are equal and also close to zero when the phase angles are identical. By a slight change of the motor speed it is possible to change the motor voltage phase angle. Hence, a  $PI$  controller is used to use the  $d$  components voltage error to modify the speed reference value. The speed reference is originally  $2\pi 50 \text{ rad/s}$ . However, for the sake of synchronization it can vary in a range of  $\pm 4\%$  of the original value. When the synchronization is finished, the contactor is closed and the grid voltage is applied to the second set of the motor windings. The virtual

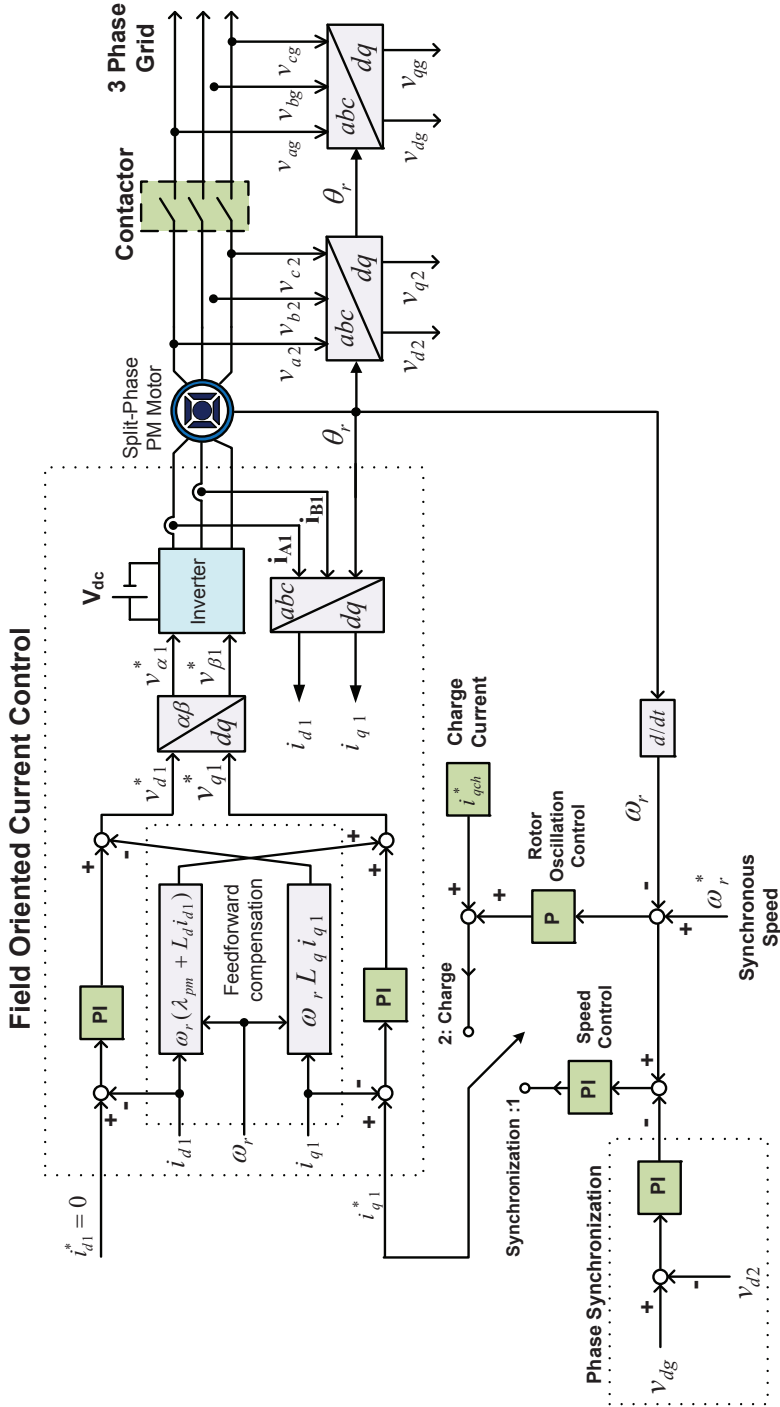


Figure 4.4: System operation in battery charging mode: grid synchronization and charge control.

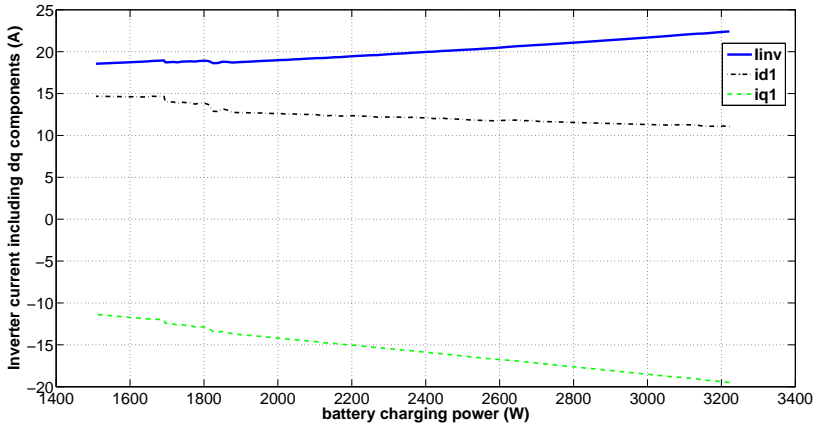


Figure 4.5: The inverter reference current as a function of charging power.

switch changes to position 2 which means that the reference value of  $i_{q1}^*$  is determined by another mechanism that is called charge level control.

## 4.2.2 Battery Charge Strategy

As explained earlier, the inverter  $dq$  current control is utilized to control the battery charging. After closing the contactor and applying the grid voltage to the machine windings, the  $dq$  voltages are not constant despite the fact that the grid voltage is ideally constant. The rotor position determines how the constant magnitude grid voltage is projected in the  $dq$  voltages,  $v_{d2}$  and  $v_{q2}$ . To meet unity power factor requirement at the grid side, the following conditions should be satisfied:  $v_{d2} = K i_{d2}$  and  $v_{q2} = K i_{q2}$  where the constant  $K$  determines the load power. Because of grid  $dq$  voltage dependence to the rotor angle, the motor dynamical equations (3.38-3.46) (the double  $dq$  model) are solved to obtain the reference currents. By using Matlab these equations are solved for a PM motor, which parameters are presented later on, to extract the inverter  $dq$  reference currents,  $i_{d1}$  and  $i_{q1}$ . The results of the reference current trajectory for the measured power level interval are shown in Fig. 4.5. In the proposed charge control strategy, the power control needs another control mechanism to be converted to the  $dq$  current control which is a function of motor parameters. This control stage, power to current, can be an online estimator or a look up table.

The transferred active power from the inverter to the motor can be written as  $p = \frac{3}{2} v_{q1} i_{q1}$  by assumption of  $i_{d1} = 0$ . So, as is shown in this equation, the power can be controlled by controlling  $i_{q1}$ . However, there might be rotor oscillations during transients. A separate  $P$  controller is used in the scheme to avoid this problem. The speed error from the synchronous speed is accumulated to the charge current to make the power level change smoothly. By changing the  $d$  component of the current,  $i_{d1}$ , it is possible to control reactive power too. Moreover, the condition  $i_{d1} = 0$  implies that there is no need to change the  $d$  current in the synchronization and charge mode which makes the

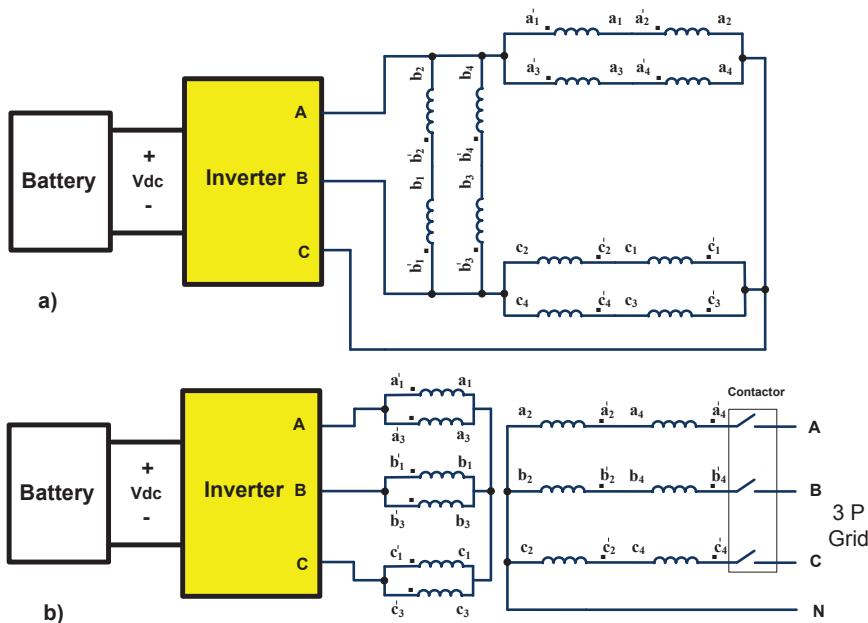


Figure 4.6: 20 kW system modes of operation: a) traction and b) charging.

implementation easier.

For the grid synchronization, the phase angle synchronization is much more important than the amplitude synchronization. For example, if the motor voltage is within 20% of the grid voltage but with the synchronized phase, it is safe to close the contactor. There will be some magnetization current to compensate the voltage difference in this case.

### 4.3 An Experimental Setup Based on a 20 kW Split-Phase IPMSM

A 4 pole IPM machine is designed, optimized and constructed for a 20 kW traction system with a possibility to reconnect the windings for charging [66]. Fig. 4.6.a shows the windings configuration (in delta) in traction mode. The dc bus voltage (battery voltage) is 400 V in this case. The machine base speed is 1500 rpm while the maximum speed is 6500 rpm. For charging, the windings are re-arranged according to Fig. 4.6.b. The charge power is limited to 10 kW due to the machine thermal limit.

#### 4.3.1 PM Motor Design

A three-phase PM assisted synchronous reluctance machine is designed for this application by Kashif Khan et al. [70]. The geometry of the designed machine is illustrated in Fig. 4.7. Fig. 4.8 shows a cross section of the motor including the phase conductor arrangement. The PM assisted synchronous reluctance

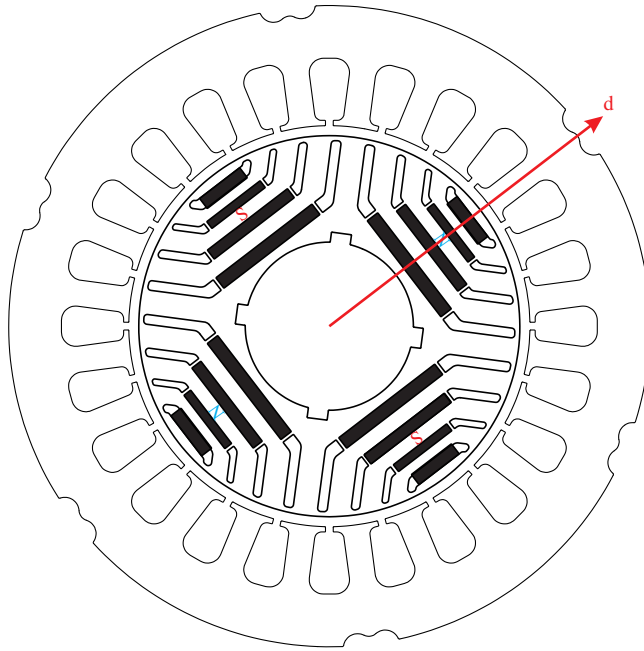


Figure 4.7: Geometry of the prototype 20 kW PM motor.

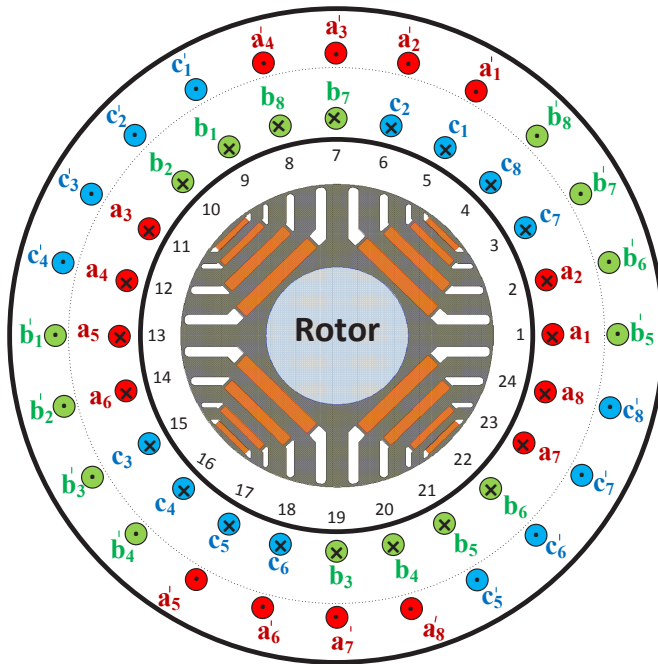


Figure 4.8: A simplified diagram of the 20 kW PM motor cross section including slot numbering and conductors arrangement.

Table 4.1: Design summary of the 20 kW PM motor.

	Value	Unit
Number of phases	3	-
Number of poles	4	-
Number of slots	24	-
Outer stator diameter	180	mm
Total axial length	330	mm
Rotor outer diameter	112	mm
Shaft diameter	51	mm
Air-gap height	0.35	mm
Thickness of tangential rib	1	mm
Magnet material	NdFeB	-
Rated torque	127	Nm
Rated speed	1500	r/min
Current density,(rms)	10	A/mm <sup>2</sup>

machine (PMaSynRM) is designed following a classical approach in which initially the machine geometry is designed to maximize the reluctance torque and later magnets are introduced to increase the torque further. However, the reluctance torque and magnet torque are equal for this machine and the motor is called IPMSM in the rest of this thesis. A transverse laminated rotor is selected because of its low cost and durability. The detailed machine design and the parametric study are reported in [70]. A brief summary of the design is presented in Table 4.1.

### 4.3.2 Traction Mode Operation

For the traction operation, the motor windings are reconfigured according to Fig. 4.6.a. The proposed design is optimized to obtain high torque and high efficiency in traction mode by means of having a salient and permanent-magnet assisted rotor. Shuang Zhao et al. at KTH have designed and implemented the sensorless operation of the drive in traction mode [71].

### 4.3.3 Simulation Results of the 20 kW Motor in Charging Mode

The whole system has been simulated by the use of Matlab/Simulink software based on the before mentioned system equations. An ideal converter is used in the simulation (no PWM or SVM is used for the inverter). Before the simulation starts, it is assumed that the system is reconfigured for charging but the grid contactor is open. The charging process starts when the inverter starts to rotate the motor by the means of battery and inverter side motor windings. The motor then rotates at grid synchronous speed.

The simulation results provided here are presented for the condition that the practical system was tested. So, the charging power levels are adjusted to be identical to the measured levels. Table 4.2 presents the motor parameters.

When the motor speed is close to synchronous speed, it is assumed that the motor voltage magnitude is close to the grid voltage magnitude, but the

Table 4.2: 20 kW PM motor parameters respect to the terminals connected to the inverter.

Rated power ( $kW$ )	20
Rated phase current ( $A$ )	30
Rated speed ( $r/min$ )	1500
No of poles	4
Permanent magnet flux ( $Wb$ )	0.27
Stator resistance ( $Ohm$ )	0.3
d axis inductance ( $mH$ )	14.9
q axis inductance ( $mH$ )	39.4
Inertia ( $kg.m^2$ )	0.04
Viscous friction coefficient (Nms/rad)	0.01

phases may not be identical. Afterwards, the voltage phase is adjusted by speed control of the motor (equivalently torque control). This control action is provided by controlling the q component of the current in this case. After adjusting the both voltage amplitude and angle, the contactor is closed and the machine grid-side windings are directly connected to the grid. At this moment the system starts to charge with a power level of 2 kW. In order to show the transient response of the system, the charge power is reduced to  $-500 W$  after five seconds.

The system operation during different time intervals can be summarized as:

- $t = 0 s$  till  $t = 0.8 s$ : The speed is regulated close to the synchronous speed,  $2\pi 50 rad/s$ . The system is in synchronization mode and the contactor is open.
- $t = 0.8 s$  till  $t = 5 s$ : The voltage of the grid-side winding is synchronized to the grid voltage (phase synchronization). The system is in synchronization mode and the contactor is open.
- $t = 5 s$  till  $t = 10 s$ : Synchronization is finished and the contactor is closed at  $t = 5 s$ . Then the dc bus is charged with a 2 kW power level.
- $t = 10 s$  till  $t = 14 s$ : At time  $t = 10 s$  the charge power level is commanded to  $-500 W$ . The system is charging with  $-500 W$  which is battery discharging.

Fig. 4.9 shows the power from the grid to the charger system. At first, while the motor/generator is in synchronization mode (the first five seconds), the grid power is zero. Then the contactor is closed and charging is started ( $t=5 s$ ) with a power level of 2 kW. After five seconds ( $t=10 s$ ), the charging power is reduced to  $-500 W$ . The electrical speed is shown in Fig. 4.10. As is shown in this figure, the rotor speed oscillations are damped quickly by the proper operation of the controller that is a  $P$  controller where is presented in Fig. 4.4 and explained before.

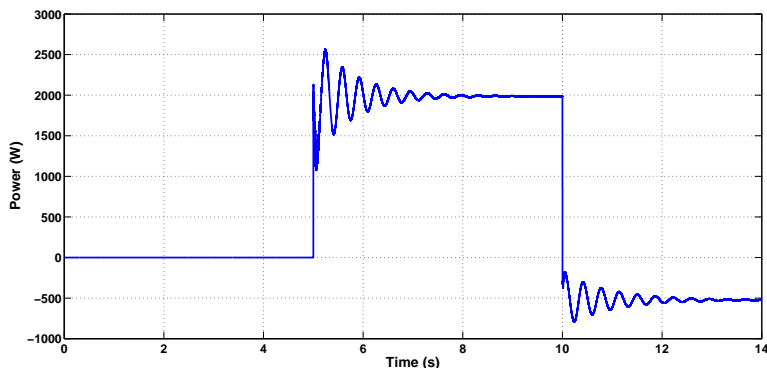


Figure 4.9: Simulation result: grid power to the charger system.

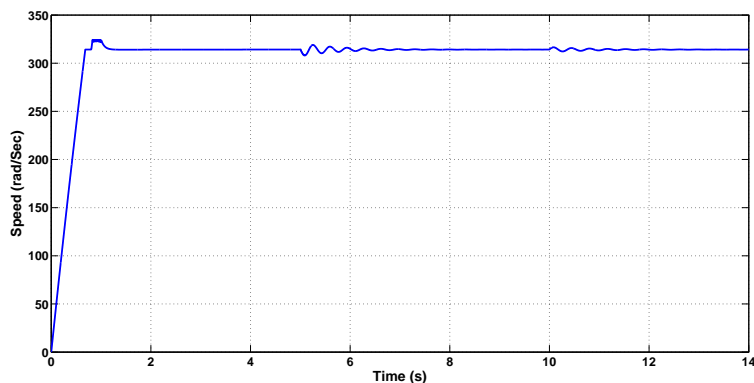


Figure 4.10: Simulation result: electrical speed of the motor/generator.

The motor/generator torque is shown in Fig. 4.11. The machine develops constant torque in the first 0.68 s to increase the speed to become close to the synchronous speed ( $2\pi 50 \text{ rad/s}$  in this case). Then there are some oscillations around times  $t = 0.68 \text{ s}$  and  $t = 1.2 \text{ s}$ . In this time interval, the motor voltage is synchronized with the grid voltage. Moreover, before closing the contactor, there is a short delay in the software to make sure that the motor voltage is stable. In addition there are some oscillations in torque around the times that the contactor is closed ( $t = 5 \text{ s}$ ) and the step change of the charge power level ( $t = 10 \text{ s}$ ). The developed torque compared to its nominal value is almost negligible (less than 1%) because there is no mechanical load connected to the machine during charging.

Fig. 4.12 shows the motor and grid voltage close to the time that the contactor is closing. As is shown in this Fig., the motor voltage is slightly lower than the grid voltage, but after closing the contactor the motor voltage is forced to a higher value, i.e. the grid voltage. This level is very close to the voltage values used in the experimental system. So, it has been tried to run the simulations close to the practical situation. Higher voltage values enabling higher power transfer assuming the maximum currents are fixed due

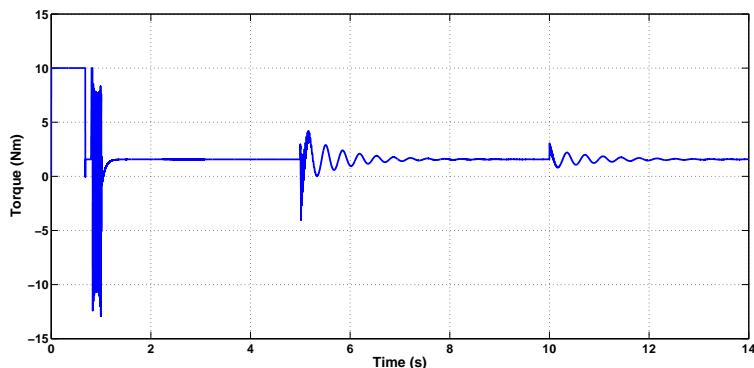


Figure 4.11: Simulation result: motor/generator torque during charge time.

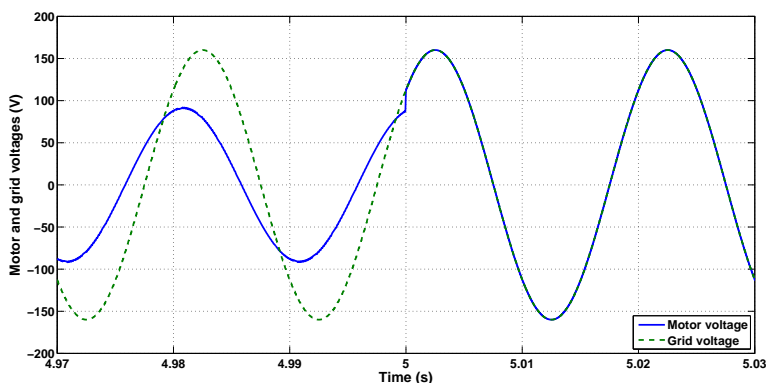


Figure 4.12: Simulation result: phase A of the motor and grid voltages during the synchronization and contactor closing time.

to thermal limits. The motor open terminal voltage at synchronous speed is not according to what is expected regarding the initial design goals, so that is the reason that instead of 230 V, a 100 V voltage is applied to the motor. The voltage difference between the motor and grid is not critical for closing the contactor if the difference is not a large value. Both simulation and practical results that are explained later on confirm that the system is not sensitive to the voltage variations. Some simulation results are shown in [9] describing the system functionality for the standard defined condition of the grid voltage variation in a normal mode or a transient period.

Fig. 4.13 shows the phase A current of the grid during the whole simulation time. At first, before closing the contactor, the current is zero. Afterwards, the current increases to reach 2 kW charging, and then it is reduced to a charge power level of  $-500$  W. Fig. 4.14 and Fig. 4.15 show the three-phase grid currents during the transients.

As is mentioned before, unity power factor operation is possible for the charger. Fig. 4.16 shows the grid side phase A winding voltage and current. The current is multiplied by a factor of 20 for more figure clarity. The reference

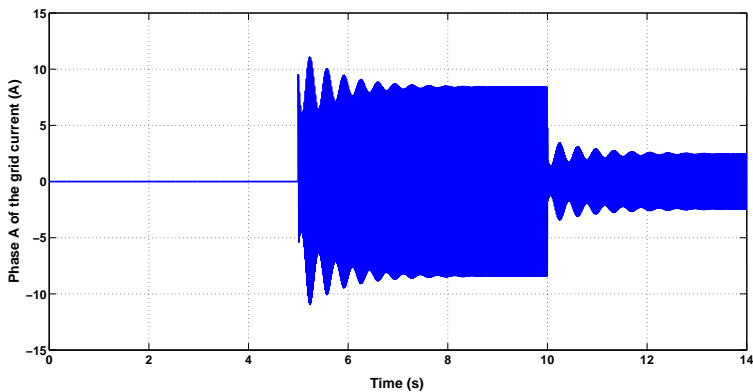


Figure 4.13: Simulation result: phase A of the grid current during charge operation.

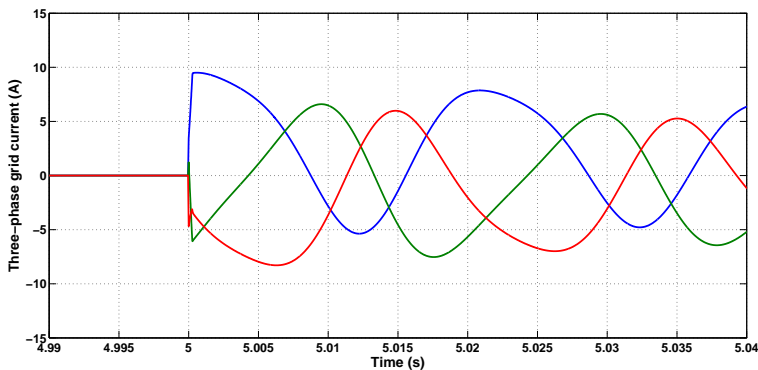


Figure 4.14: Simulation result: three-phase grid currents during the start of high-power charging.

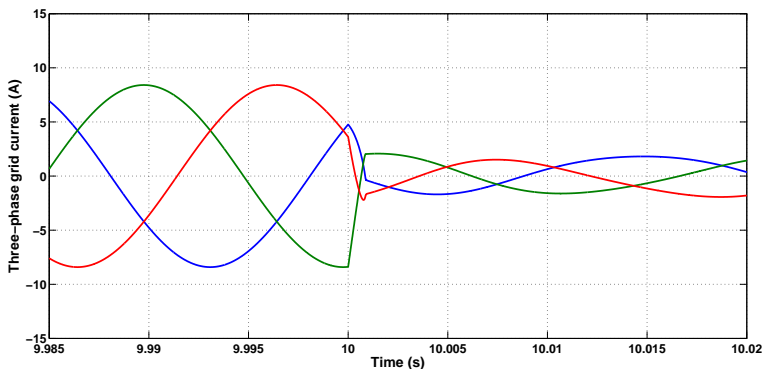


Figure 4.15: Simulation result: three-phase grid currents during the step change in the charging power from 2 kW to -500 W.

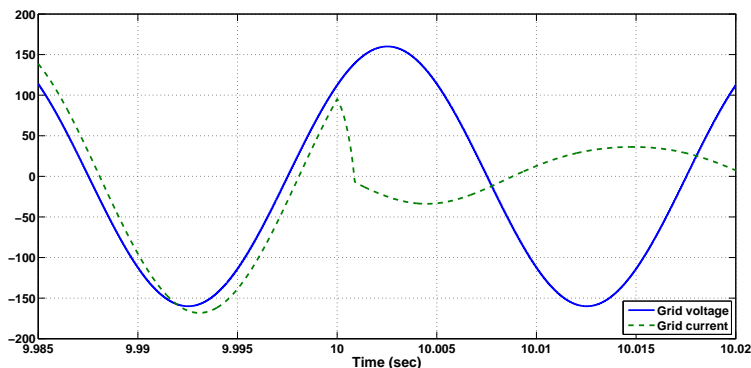


Figure 4.16: Simulation result: phase A grid voltage (V) and scaled grid current ( $1/20A$ ) during the step change in the charging power from  $2\text{ kW}$  to  $-500\text{ W}$ .

value of the  $d$  component of the current,  $i_d$ , is set to zero. By changing this value it is possible to slightly change the power factor. However, here the value is kept to zero. Due to the voltage drop in the leakage inductor, there is small phase-shift between the phase voltage and current yielding that the current lags the voltage. After changing the power level to the negative value of  $-500\text{ W}$ , the current phase-shift is changed to a  $-\pi$  indicating negative power as the battery sends the power back to the grid.

#### 4.3.4 Description of the 20 kW Experimental Setup

To verify and assess the proposed integrated motor drive and isolated battery charger, a practical set up is designed and implemented based on a  $20\text{ kW}$  split-phase IPMSM. The dSPACE DS1103 controller is used in the setup which is a real-time fast prototype developing control system. The controller and some auxiliary devices are installed on a stand-alone rack placed beside the vehicle. Fig. 4.17 shows the developed experimental system, which is explained in detail in the following [72].

##### The Main Structure of the Setup

Fig. 4.18 shows a basic diagram of the experimental system. The main parts of the system are the motor, the inverter, the relay-based switching device for the motor winding reconnection, the controller, the measurement devices and interfaces, the protection systems and some auxiliary devices. For the sake of system study, different ac and dc digital and analogue signals are measured or controlled including the motor speed.

The motor is installed under a Ford Escape vehicle provided and prepared by Volvo Cars Corporation. The motor is connected to a mechanical brake that makes it possible to load the motor by pressing the brake pedal. The inverter, the switching device, the voltage/current measurement devices and some other circuits are installed in a box mounted inside the vehicle over the

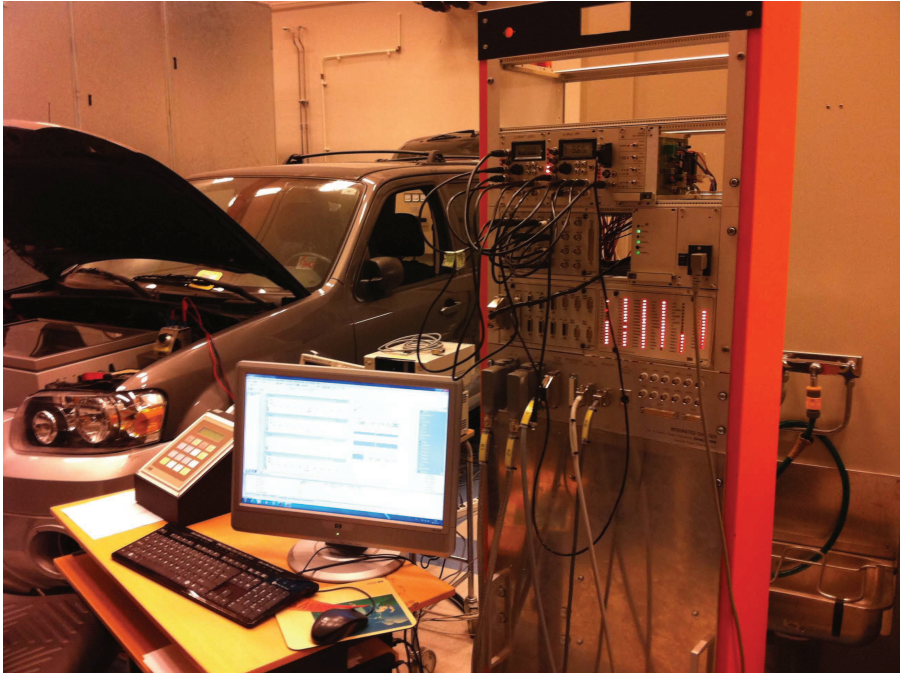


Figure 4.17: The experimental setup including the vehicle.

motor. Fig. 4.19 shows the motor installation and Fig. 4.20 shows the box including the inverter, relays and other circuits.

### The Motor and Inverter

The motor is a water cooled 4 pole IPMSM machine that is explained in section 4.3.1. The motor power is 20 kW in traction mode with a possibility to reconnect the windings for charging. The maximum winding thermal limit of the motor for charging is ideally 10 kW. During the experiments, the dc bus voltage (battery voltage) is 350 V in this case. The motor parameters for the three-phase windings connected to the inverter and with a winding arrangement according to Fig. 4.6.b is summarized in Table 4.2. The motor geometrical information is presented in Table 4.1.

A water-cooled inverter is designed and implemented based on the Mitsubishi PM600DSA060 intelligent power modules (IPMs). Each module includes two IGBT devices and anti-parallel diodes that is one leg of the inverter. The modules are capable of handling 600 A and a peak current of 1200 A while withstanding 500 V. Built-in control circuits provide optimum gate drive and protection for the IGBT and free-wheel diode power devices. Each IPM has a built-in protection logic providing the short circuit protection, over current protection, over temperature protection and under voltage protection. However, to reduce the impact of the environment noises on the gate signals, an optical cable is used between the controller and IPMs including related hardware and supplies.

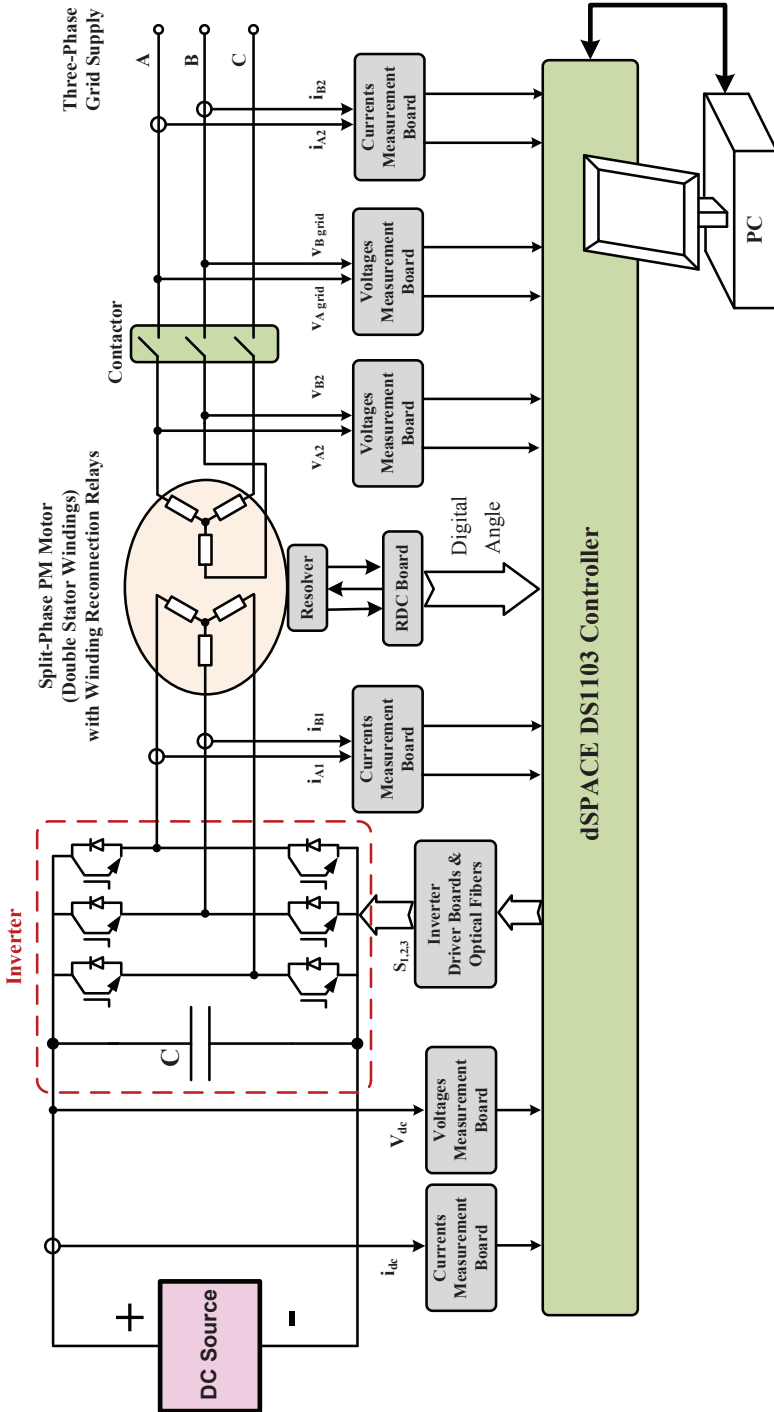


Figure 4.18: Block diagram of the experimental system: integrated 20 kW motor drive and isolated battery charger.



Figure 4.19: Motor installation inside the vehicle.

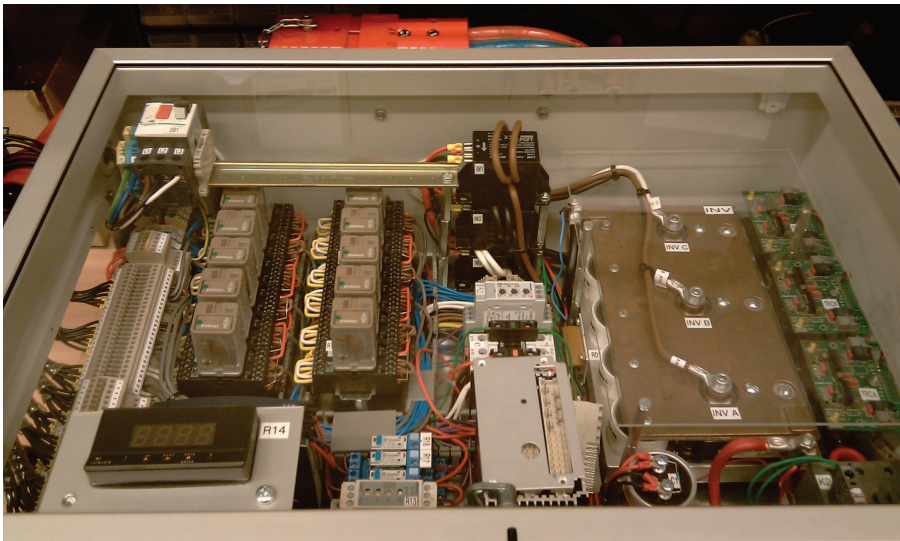


Figure 4.20: Installed panel inside the vehicle including the inverter, switching relays, sensors and so on.

## Relay-Based Switching Circuit for Windings Reconfiguration

Fig. 4.21 shows a schematic diagram of the relay-based switching device. There are 12 relays and one three-phase contactor in the switching device, which are used to change the system configuration from charging to traction and vice versa. The relays and related driver circuits are installed in the box.

## Position Measurement Using Resolver

The rotor position is measured using a resolver installed on the motor shaft, and a resolver-to-digital converter (RDC) [73]. The resolver is composed of three coils: one excitation coil mounted on the rotor and two pick up coils mounted on the stator with  $90^\circ$  shift from each other. A printed circuit board (PCB) is designed and implemented for the position measurement. The excitation signals, angle measurement processing, and angle analogue to digital conversion are provided by the RDC. To read the digital rotor angle, a digital request signal is sent to the board by the controller that starts the angle conversion. Consequently, the angle data that is a digital word will be available at the RDC buffer ports.

The sinusoidal reference wave, with a frequency of  $6.6\text{ kHz}$  in this case, can be adjusted by the user by setting some jumpers and changing some circuit components of the RDC. The reference signal is applied to the resolver's rotor coil and the induced voltage in the stator coils are sent back to the RDC. The RDC board processes these signals and obtains the rotor angle by the use of an AD2S83 converter. Afterwards the analog signal containing the angle is translated into a digital word with a selectable resolution of 10, 12, 14 or 16 bits. Finally, the RDC board sends the digital word that is 12 bits in this case to the digital I/O port of the dSPACE controller.

To tune the measured angle, the motor was rotated by another motor as a generator while the terminals were open. The measured back EMF was used to adjust the measured position by adding an offset. However, by looking at the motor  $dq$  voltage in this situation it is possible to do this calibration. For the before mentioned  $dq$  transformation and rotor angle definition, the  $d$  voltage is zero in this case. As is mentioned earlier, this principle is used to perform the grid synchronization by comparing the  $d$  voltages of the motor and the grid.

## The dSPACE Controller

The control is implemented using dSPACE 1103. This rapid control prototyping system consists of both hardware and software. The hardware is composed of the CP1103 controller board with analogue and digital I/O. The analogue I/O can send or receive signals within the range of  $\pm 10\text{ V}$  and the digital I/Os operate within TTL(Transistor-Transistor Logic) range. All signals in CPL1103 can be monitored by status LEDs.

Using the dSPACE Real-Time Interface (RTI), it is possible to fully develop the programs from the Simulink block diagram environment. So, the whole software is developed in the Simulink environment. The PWM frequency of the FOC is  $11\text{ kHz}$  which is synchronized to the voltages and currents measurement instants. This synchronization is vital in order to have a robust control system, especially for the current control loops.

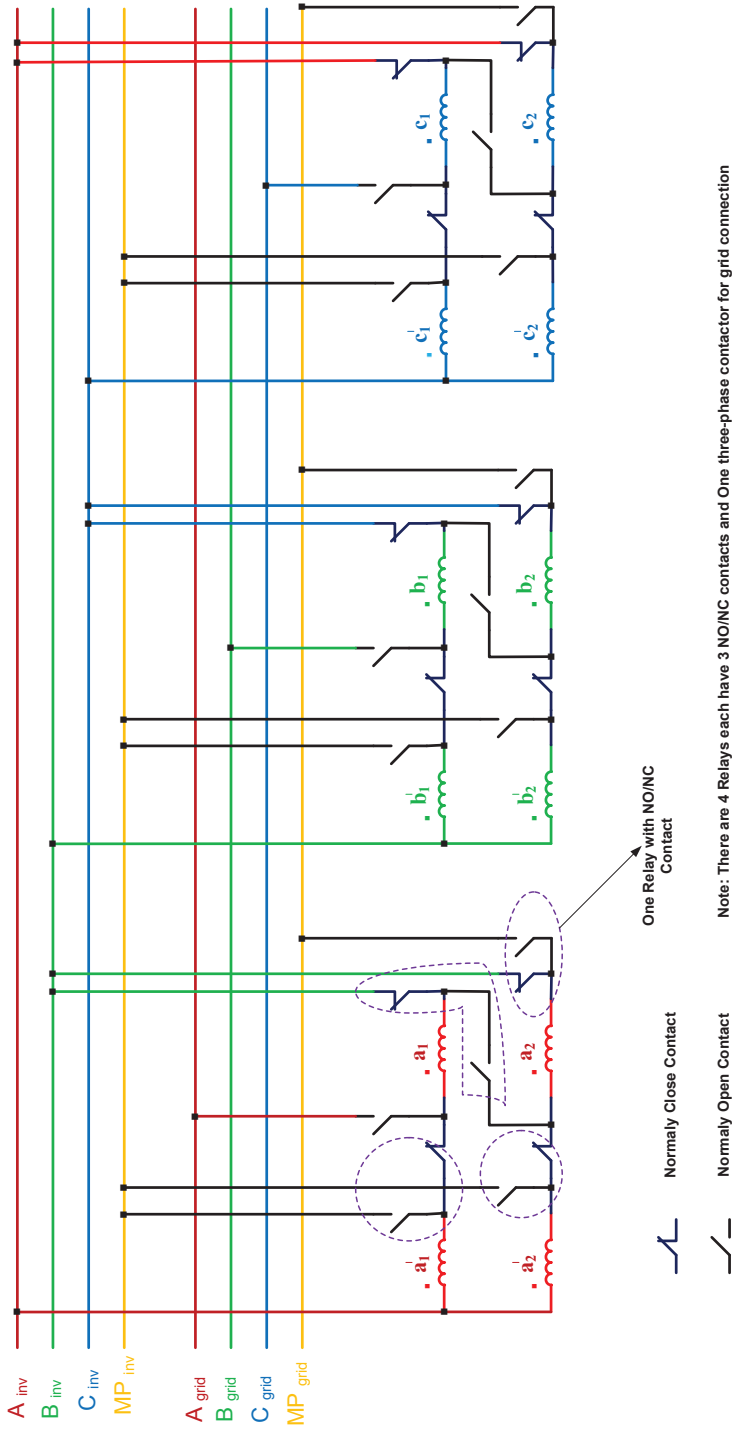


Figure 4.21: Circuit diagram of relay-based switching device for windings re-configuration from the traction mode to charging mode and vice versa.

## Electrical Measurement Interfaces

To measure the voltages, voltage transducer boards with the isolation amplifier AD210JN are used. The input voltage is reduced by a resistive divider to a value that is proper for dSPACE, i.e.  $\pm 10$  V. The transducers are designed to convert  $\pm 400$  V to  $\pm 10$  V. Afterwards, the signal reaches to the output of the transducer through an isolation amplifier that protects the dSPACE system against over voltages.

For the current measurements, LEM LT300-S current transducers are used. This device comes with galvanic isolation between the primary and secondary circuits and it provides a secondary current proportional to the measured current. This secondary is equipped with a resistor to make sure that the signal at the receiving end of the dSPACE is always kept within the range of  $\pm 10$  V.

The output signal reaches a printed board that compares the actual value of the current with a limit value set by the user. In case that the measured value exceeds the limit, the device generates an error signal that stops the PWM pulses, and therefore the whole system. Fig. 4.22 shows the stand alone rack containing the dSPACE I/O interface, the PWM protection units, some auxiliary devices like power supplies and some distribution terminals.

## The Software Development and Control Implementation

The whole control program is performed in Simulink. The main reason was to be able to study and investigate different aspects of the system. For example, it is possible to change a controller gain in real-time while the motor is running. However, there are more blocks in the software like saturation, integrator anti-windups, filters and so on that are not explained here. There are both automatic and manual control on some parts of the system for the protection purposes. For example, it is possible to connect/disconnect the grid contactor by software or manually.

During the system design more quantities than necessary ones were measured for study purposes. For example, both the dc bus current and voltage are measured by the system. So it is possible to see the system efficiency online.

The measurement capture is synchronized with PWM pulses to ensure data validity. After the measurement, a software programmed interrupt initiates the control process. First the speed regulator and then the currents regulators operate to generate a voltage vector. This vector results into a PWM duty cycle by means of the PWM3 RTI block. One important issue is that current measurement should be synchronized with PWM signals. If the current measurement occurs during the inverter switching, the measured value may include some ripple that can drastically degrade the system performance. The current controllers regulating the fastest dynamics in the system and their performance have a critical impact on the whole system. Because of the slower dynamics of the mechanical system compared to the electrical part, it is not necessary to measure the angle with a high sampling rate, so the angle measurement is reduced to  $1.1$  kHz due to the RDC design.

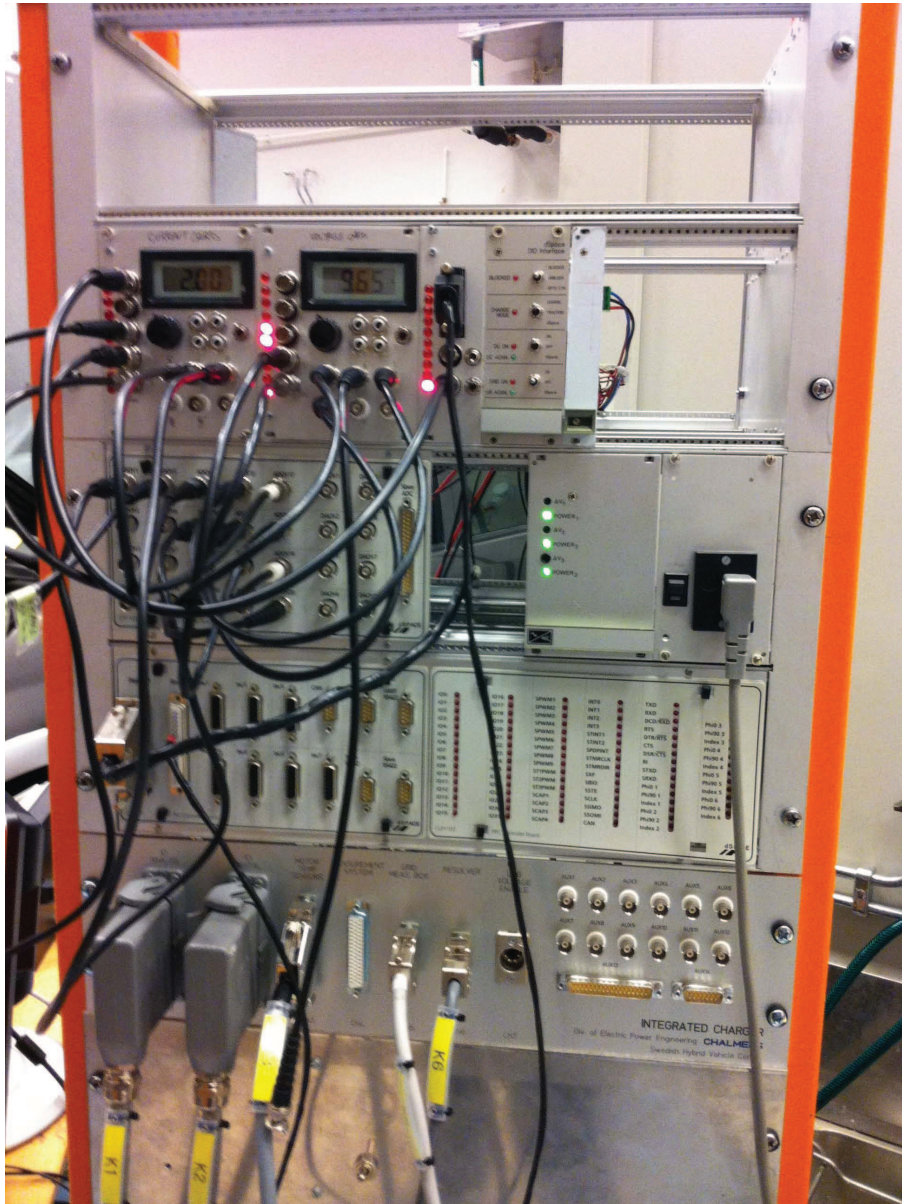


Figure 4.22: Standalone rack including the dSPACE interfaces, resolver, fast protection and other auxiliaries.

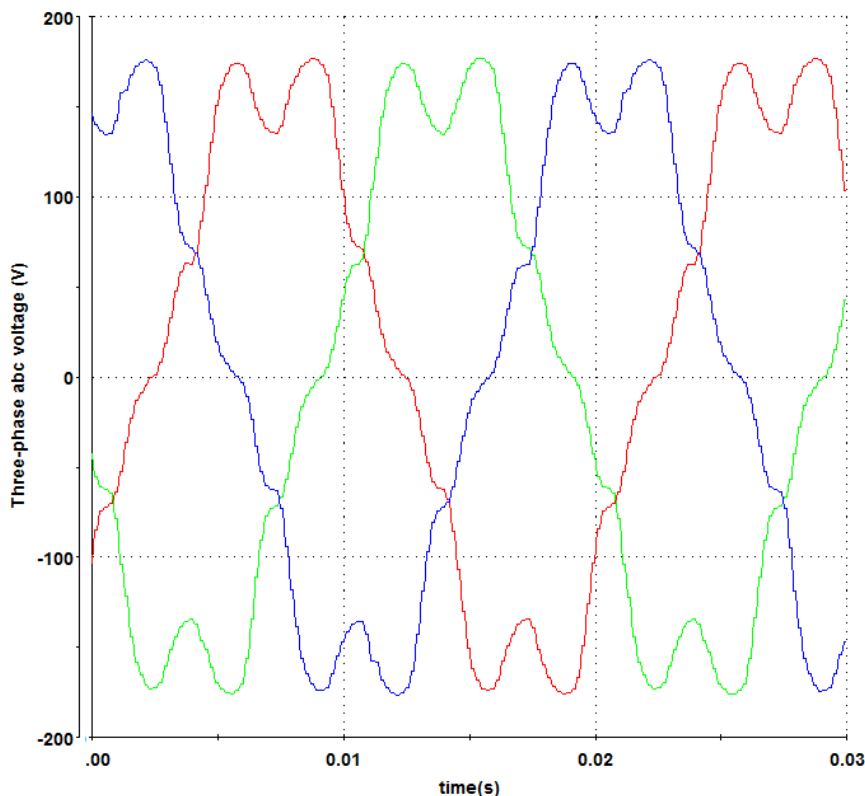


Figure 4.23: Measurement: back EMF voltage of the motor windings in the charging mode.

### 4.3.5 Practical Results of the 20 kW System and Discussions

To determine the motor flux constant and to evaluate the quality of harmonic contents, the motor back EMF is measured at different speeds. For example, Fig. 4.23 shows the three-phase voltage at synchronous speed while the motor terminals are open. This voltage will be connected to the utility grid after synchronization in charging mode. For the constructed motor, the back EMF was lower than that of the expected value. This voltage needs to be close to the grid voltage otherwise a large amount of magnetization current is drawn by the grid after closing the contactor. However, in this system the grid voltage is reduced to half of the rated value by using an autotransformer to match the motor back EMF. So, the motor back EMF needs to be carefully controlled in the design stage for the proposed system. Moreover, the motor design is optimized for traction mode. As can be seen from the back EMF, the harmonic content is high. As a recommendation for the next design, more emphasize to the motor performance in charging mode is needed in the design stage.

As mentioned earlier, the motor grid-side winding voltages, and the grid voltages are synchronized by adjusting the motor speed. Fig. 4.24 shows phase

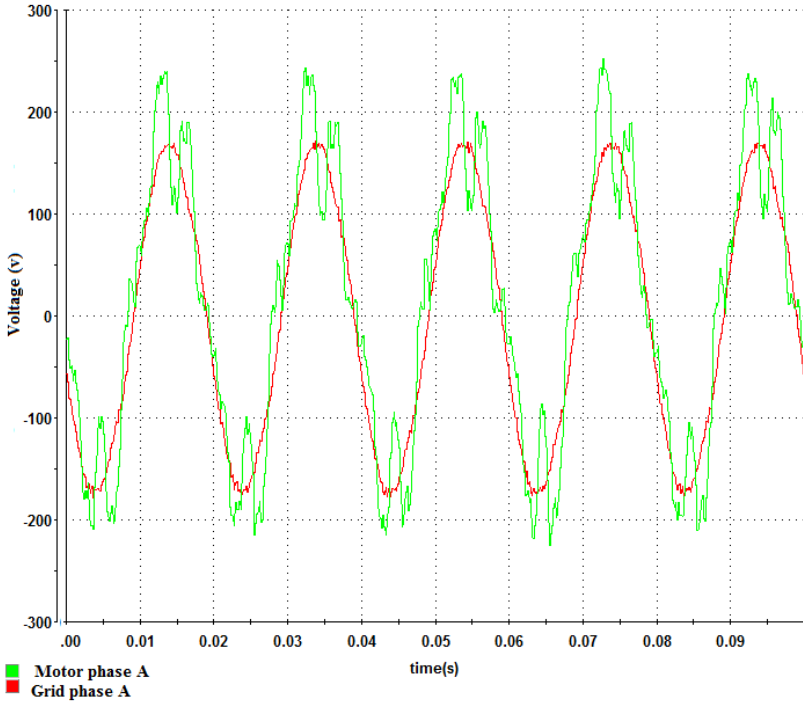


Figure 4.24: Measurement: phase A voltage of the grid and motor during synchronization and before closing the contactor.

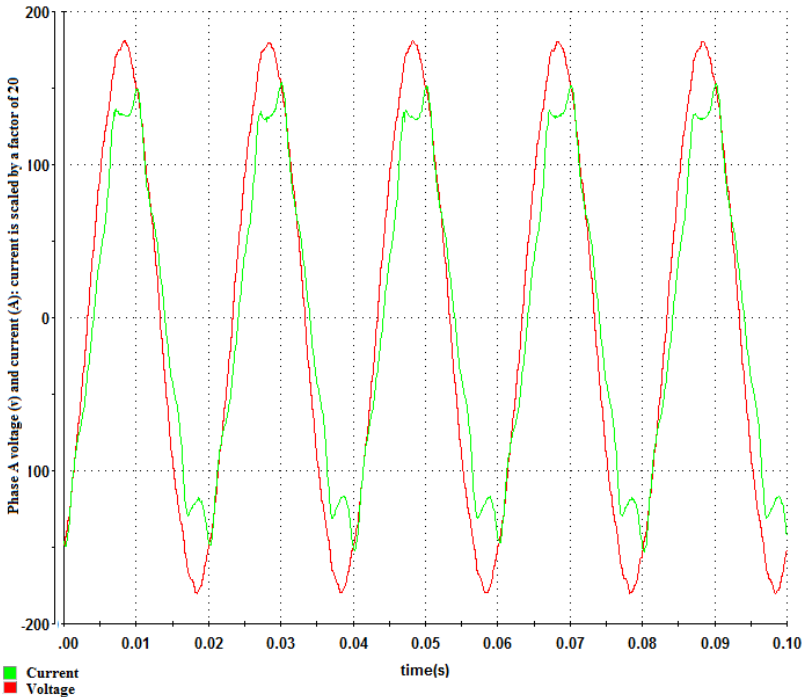


Figure 4.25: Measurement: phase A of the grid voltage and current during the battery charging operation.

A of the motor and grid voltages during synchronization and before closing the contactor. The  $d$  component of the motor current is set to zero. By changing this value, it is possible to adjust the motor voltage due to the change of the flux level. Nevertheless, this voltage variation is limited by practical limitations like efficiency or speed stability. If the motor voltage is not exactly the same as the grid voltage, after closing the contactor, the motor draws required magnetization current from the grid to reach a steady-state working point at synchronous speed. If the magnetization current is too high, the efficiency goes down mainly due to the stator copper losses.

The motor phase A voltage and current at the grid side is shown in Fig. 4.25 during the battery charging operation. The power factor is very close to one. By changing the  $d$  component of the current it is possible to change the power factor. Fig. 4.27 shows the measured system response to the step change of the charging power from a power level of  $-500\text{ W}$  to a power level of  $1300\text{ W}$ . The inverter current is changed from  $4\text{ A}$  to  $-7\text{ A}$ . As is shown in the figure, the dynamic response is fast (less than half of a second) and the oscillations are damped quickly where negative (vehicle to grid) to positive (battery charging) operation is depicted.

- System performance: efficiency

The system efficiency in charging mode is less than the one in traction mode, because with the same amount of loss, the output power is reduced more than half. The total loss in the charging mode is the inverter loss and the motor loss. The inverter loss is divided into the switching loss and conduction loss for this PWM-based inverter [74, 75] which is a complicated function of the current. For this system, the inverter loss is measured  $80\text{ W}$  for the case that the motor is running at the synchronous speed without charging. So, as a rough estimation,  $100\text{ W}$  is assumed for the total inverter loss in all cases.

Motor loss is mainly copper loss and iron loss. The iron loss is almost a constant value since the motor is running at a constant speed which is measured  $200\text{ W}$  for this system. The copper loss is a function of output power. For the optimal current trajectory that is shown in Fig. 4.5, the efficiency is calculated to be  $82.7\%$  for a charging power level of  $500\text{ W}$  to  $3000\text{ W}$  considering only the copper loss. However, in the measurement setup  $i_{d1} = 0$  and it is different from the optimal case as described earlier.

The measured system efficiency is shown in Fig. 4.26 for different power levels. The measured efficiency is slightly lower than the expected one, and the main reason is the deviation from the optimal current trajectory and inaccurate inverter loss. The efficiency is measured from the dc source port to the ac line source. For the dc and ac sources, the laboratory sources are used. The vehicle battery is not used in this phase of the project due to safety reasons.

- System performance: dynamic response

The charger response to the load disturbance is an important characteristic of the system. For example, if there is a fault in term of over-current in a short duration of time, the charger may need to be able to recover itself after the fault clearance or it may be needed to shut down the charger and wait for the operator maintenance. The charger response in these cases, are according

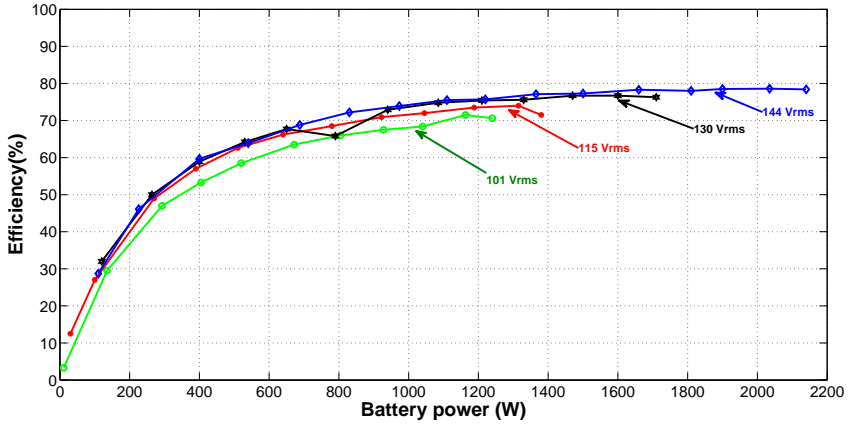


Figure 4.26: Measurement: system efficiency in charging mode.

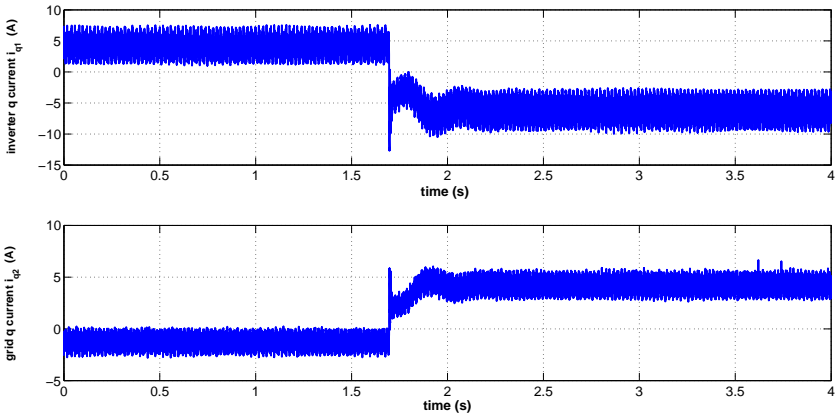


Figure 4.27: Measurement: system dynamic response to the step change of the charging power.

to the claimed specifications by the manufacturer or the covered class of the related standard [76]. For this application, vehicle battery charger, it is not expected to have a step change in the load since the battery is a continuous load. So, it is not expected to have a step change in the load during the charge operation. Nevertheless, as mentioned earlier, Fig. 4.27 shows the system response to a step change in the charging power level of  $-500\text{ W}$  to a power level of  $1300\text{ W}$ . Usually the battery is charged with a constant current (bulk charge) and after reaching a certain amount of state of charge, the current control converts to a fixed voltage mode (holding voltage). So, as is shown in this figure, the charger dynamic response is fast enough in the context of the application.

- System performance: limitations and improvements

To be able to charge the battery with high power, the controlled inverter operation is needed. The charging power of 10 kW was the design goal. However, the back EMF was not according to what was expected (it was half of the desired value). So the charging power was limited to 5 kW for this motor. A charge power of up to 3 kW is tested. After this power level, the rotor started to oscillate. By increasing the system switching frequency it was possible to increase the charge level. The dSPACE controller could not handle more switching frequency in this case. The harmonic content of the back EMF was a limiting factor. By looking to the current waveform, it was realized that the current waveform has some nonlinearities that is mainly due to the motor harmonics. So, it is recommended to design the motor with a waveform closer to sinusoidal in charging mode.

## 4.4 An Experimental Setup Based on a 1 kW Split-Phase PMSM

As the second example, a set up is designed and implemented based on a 1 kW split-phase permanent magnet synchronous motor where two sets of three-phase windings are not shifted. Each phase winding is simply divided into two identical parts in this case [77]. Fig. 4.28 shows a basic diagram of the second experimental system. An available PMSM is re-wound to have two sets of windings, so the motor is not optimized for this application. Nevertheless, it is possible to verify the system functionality with this set up.

First, the contactor is open and the dc source powers the motor through the inverter. The motor grid-side windings are open and they pick up the induced voltage due to the rotational back EMF in the stator. A classical SPWM-based FOC is used to control the motor with the inverter-side windings. By proper controlling of the motor flux and speed, it is possible to synchronize the motor with the grid in phase and amplitude. When synchronization is finished, the contactor is closed and grid voltage is applied to the motor. Afterwards, it is possible to feed power from the grid to the battery. The inverter currents and dc bus voltage are measured to have FOC of the drive system. The rotor angle is also measured by a RDC for the proper voltage vector calculation.

The dSPACE DS1103 controller is used in the setup which is a real-time fast prototype developing control system. The controller is linked to a PC via an ISA extension bus. The controller digital signals are TTL compatible, and the analog input signals are  $\pm 10$  V. Hence, suitable measurement interfaces or signal drives are used to adapt different devices to those values.

The inverter type used in the practical setup is SEMISTACK-IGBT, a SEMISTACK family product, from Semikron. The inverter rated values are 400 V<sub>ac</sub>/600 V<sub>dc</sub> and 30 A. The gate signals are isolated from the main power circuit and are triggered by the CMOS level voltages, so a level shifter is used to boost the controller TTL signal to the CMOS level.

The motor is a 6 pole machine with nominal mechanical speed of 1000 r/min. The inertia is  $5.8 \cdot 10^{-4}$  kg.m<sup>2</sup>, and the viscous factor is 0.002 Nm.s. The motor inductance value is 30 mH, and the rated current is 1 A for this machine. A

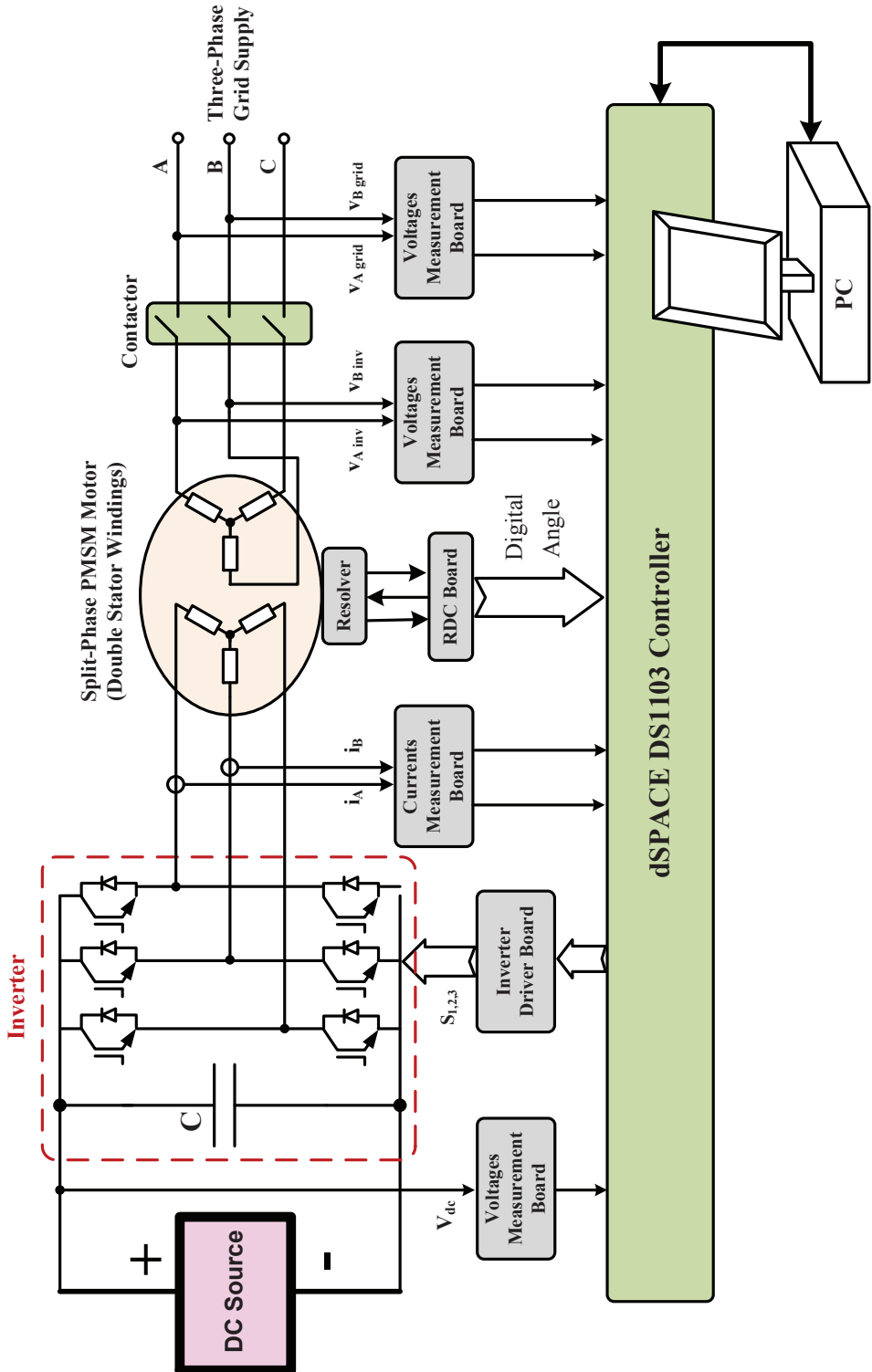


Figure 4.28: Block diagram of the experimental system: integrated 1 kW motor drive and battery charger.

resolver transducer is attached to the motor since the machine was originally designed for a servo system.

The dc bus voltage, motor grid-side winding voltages and grid voltages are measured by designed interface boards. The hardware is based on the AD210 isolated amplifiers. These voltage transducers convert  $\pm 400\text{ V}$  signals to  $\pm 10\text{ V}$  signals.

Two phases of the inverter currents and the grid currents are measured by current measurement cards. For the current measurement, LEM LA 50-S/SP1 modules are used. This device, with galvanic isolation between the primary and the secondary circuit, outputs a secondary current proportional to the measuring current. A resistor is used to convert this current to a voltage signal suitable for the dSPACE system. The main current in the  $\pm 10\text{ A}$  range is converted to a  $\pm 10\text{ V}$  voltage signal in these boards.

A printed circuit board is designed and fabricated to measure the rotor angle by the resolver. A sinusoidal  $6.6\text{ kHz}$  reference waveform is generated and fed to the resolver rotor coil. The induced voltages on the stator coils are measured and fed to the RDC converter, that is AD2S83 in this case, by some interface circuits. The angle is converted to a programmable resolution digital word, 12 bit in this case, within RDC operation. The resolution is programmable by the device. The angle in digital form is available at the output port after suitable handshaking operation by the dSPACE system.

Some other hardware components are used in the system that are not explained here such as inverter current protection card, grid connection relay, auxiliary supplies and so on. Fig. 4.29 shows a physical layout of the experimental system, and Fig. 4.30 shows the RDC board.

Using the dSPACE RTI, it is possible to fully develop the programs from the Simulink block diagram environment. So, the whole software is developed in the simulink environment. The PWM frequency of the FOC is  $12\text{ kHz}$  that is synchronized to the voltages and currents measurement instants. This synchronization is vital to have a robust control system especially for the current control loops.

The position is read by the dSPACE system as a digital word. This measured angle is converted to an electrical angle by pole pair multiplication compensation. Moreover, the measured angle is calibrated by offset compensation. In this case there are two sets of stator windings, so it is possible to measure the grid-side winding voltages for this calibration process.

As mentioned earlier, the motor grid-side winding voltages, and the grid voltages are synchronized by adjusting the motor speed. Phase A of the voltage for both motor and grid are shown in Fig. 4.31 before and after closing the contactor during the synchronization. At grid synchronous speed, the motor voltage is not equal to the grid voltage since the motor is not designed for this application. So, a step down transformer is used to reduce the grid voltage level close to the motor voltage. The synchronization controller output is a velocity reference signal for the drive system that is converted to the reference values for  $d$  and  $q$  components of the current by proper control within FOC. When the contactor is closed, the motor is rotating with grid frequency.

The dc source has been charged with a power level of  $300\text{ W}$  at unity power factor operation condition. Moreover, the power transfer from the battery to the grid is also verified.

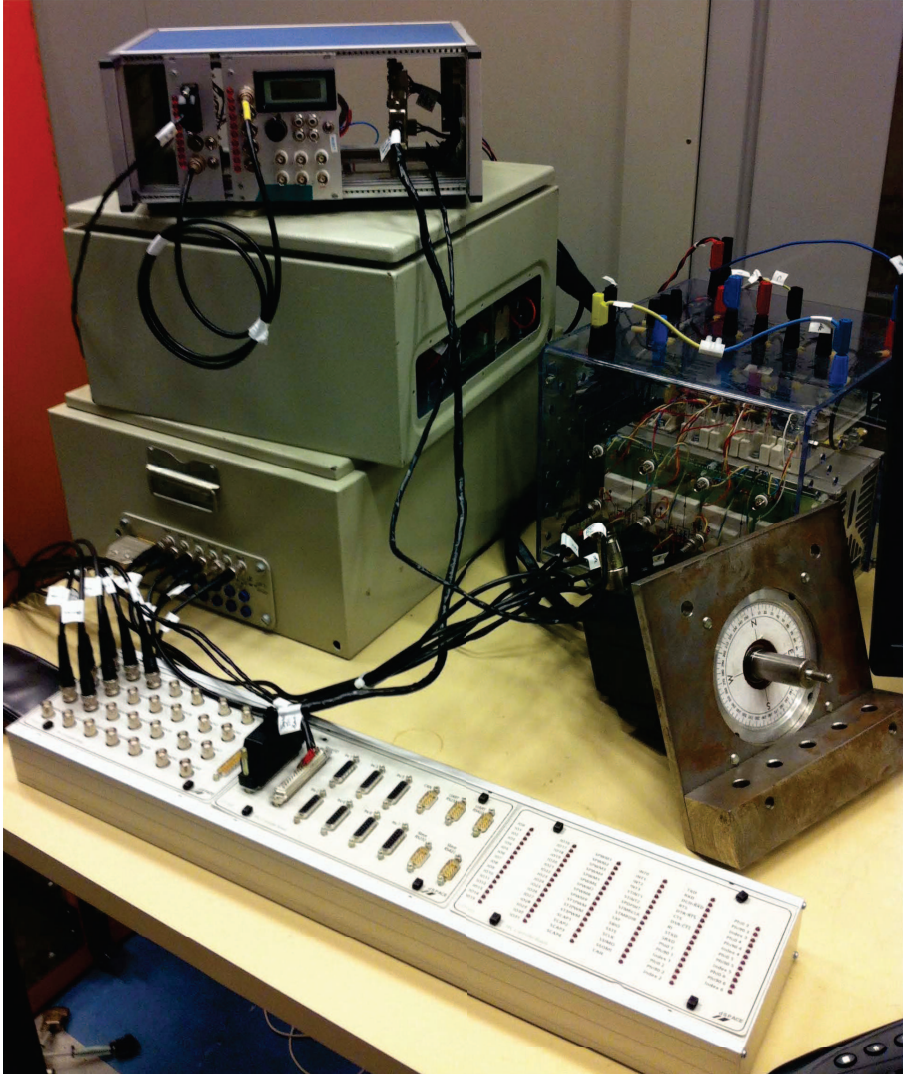


Figure 4.29: Photo of the 1 kW experimental system.

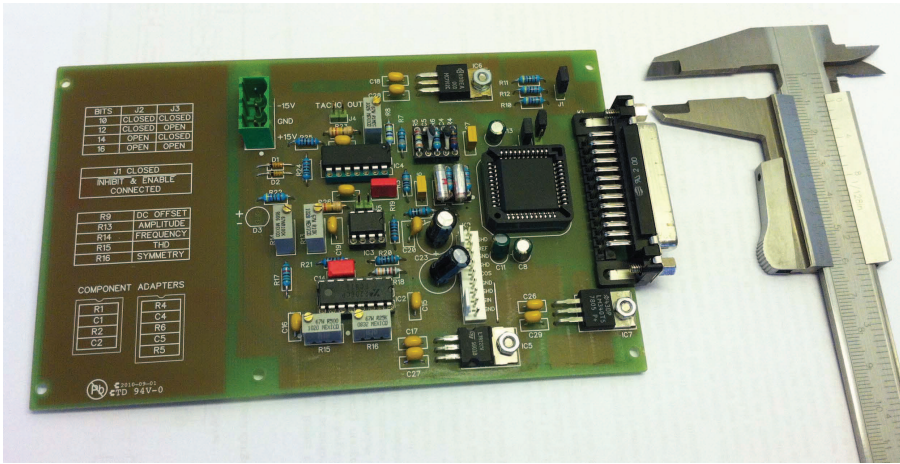


Figure 4.30: Resolver-to-Digital PCB.

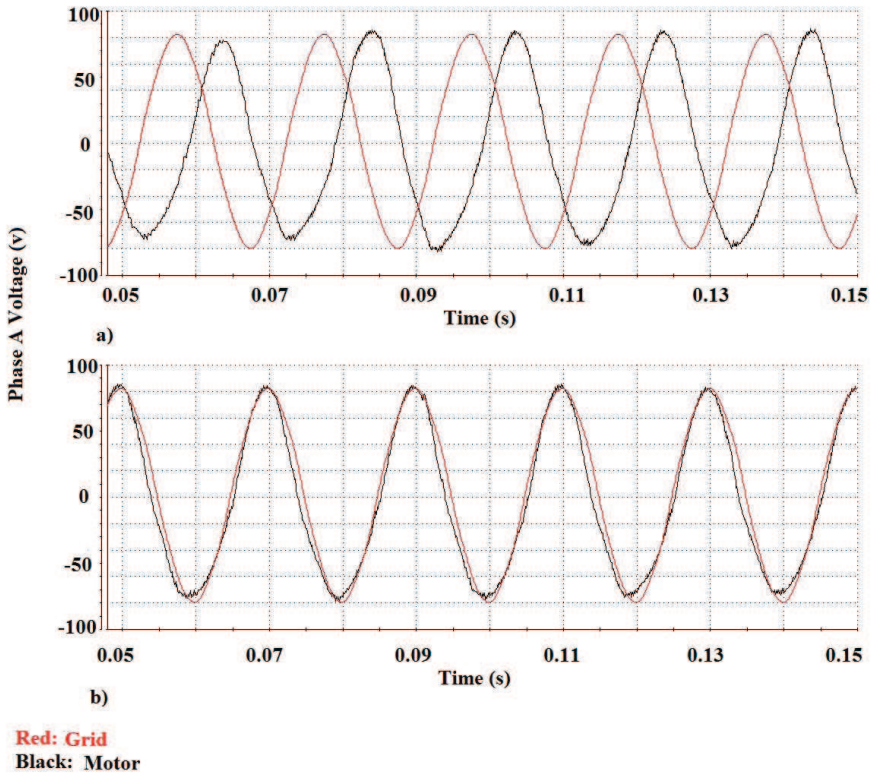


Figure 4.31: Measurement: the motor grid-side winding and grid phase A voltages: a) before synchronization b) after synchronization.

## 4.5 A Trigonometric Velocity Estimator Using a Resolver Sensor

Industrial drive systems need position feedback signal for the proper control and operation. This angular position signal can be estimated or measured. Sensorless drive systems are widely used in industrial applications, but still there are some applications where sensorless control can not achieve the required performance and a position sensor like a resolver or an encoder is necessary to have [78, 79].

In many applications, the motor speed is needed for control purposes. Since it is expensive to have two separate sensors for the angle and speed measurement, the speed signal is estimated from the measured angle in drive systems [80]. One of the most used methods is to estimate the speed through differentiation of the position signal, followed by a low-pass filter [81]. This method has a good performance at steady state, but due to the time-delay impact in the filtering stage, the transient response may not be fast enough [78].

A resolver is a very reliable and robust position sensor that is suitable for harsh environment. There are one rotating coil attached to the shaft and two stationary perpendicular coils in the resolver sensor. A high-frequency signal is injected to the rotary coil and the induced voltages on the stationary coils are measured. The rotor position is extracted by the processing of these three waveforms [82]. An RDC can be utilized to extract the position in digital format. To estimate the speed from this extracted position, different methods can be used [83].

Different observer-based velocity estimators have been suggested [84]. These observers can be deterministic such as the the methods based on the phased-locked loop (PLL) techniques [85], or can be stochastic such as the methods based on the Kalman filtering. However, there are some combinations of PLL and Kalman filtering methods that are reported also [86].

The stochastic observers like Kalman filter, treat the system as an uncertain system with some noise inputs. For proper operation of the filter, noise related parameters such as process noise covariance or measurement noise covariance, should finely be tuned. Usually a trial and error approach is needed for tuning. However, the Kalman filter is optimal filter and has a very good dynamic performance [87].

For the observers using a PLL, the main limitation is that the system is sensitive to the position error in order to estimate the speed. So, this will create a delay in speed estimation in the whole drive system reducing the drive dynamic response especially during the acceleration or braking [84]. Moreover, the motor parameters are needed for observer design as well. However, different improvements of the basic scheme have been reported for these PLL-based methods [88].

However, the system design and structure depend to a far extent on the application. Many different speed estimators has been reported for different drive applications that can be found in the literature [89].

For this application, an open-loop trigonometric speed estimator is proposed and explained assuming that the angle position is available by a RD converter. The proposed method has a simple structure and is easy to implement by software (there is no need for extra hardware components). Derivation

of  $\sin$  and  $\cos$  of the angle is calculated and then the speed is extracted using trigonometric features. Afterwards, a low-pass filter is used to reduce the speed noise. During differentiation the  $\pm\pi$  jumps in the position is eliminated since  $\sin$  and  $\cos$  of the angle are used. There is no need to tune any parameter in the proposed estimator, but the low-pass filter should be designed properly to achieve required dynamic performance.

In the proposed velocity estimator, it is assumed that the angle information is available by the measurement, but it is possible to use the estimated position as well. So there is no limitation to use the method in other applications like sensorless drive systems. However, this proposed extension should be investigated more for more exactness.

#### 4.5.1 Resolver and RD Converter for Position Measurement

Resolvers are basically rotary transformers with one primary coil in the rotor and two secondary coils in the stator used for the shaft position measurement. A high frequency signal,  $u_{ref}$ , is injected into the rotor and two induced voltages on the stator coils,  $u_{sin}$  and  $u_{cos}$ , are measured. By processing the rotor excitation waveform and the two measured stator voltages, the shaft position can be extracted. For example, a RD converter can be utilized for the angle estimation. Fig. 4.32(a) and Fig. 4.32(b) show a simple diagram of the resolver sensor arrangement and a basic schematic diagram of a type II RD converter, respectively [90].

If the rotor position is  $\theta$ , the resolver windings voltages can be written as:

$$u_{ref} = A \sin\omega t \quad (4.1)$$

$$u_{cos} = B \sin\omega t \cos\theta \quad (4.2)$$

$$u_{sin} = B \sin\omega t \sin\theta \quad (4.3)$$

where  $\omega$ ,  $A$ , and  $B$  are the frequency of the excitation signal, the excitation voltage, and the measured coils' voltage, respectively.

The resolver signals, are fed to the RD converter for position tracking and velocity estimation as shown in Fig. 4.32(b). The input signals,  $u_{sin}$  and  $u_{cos}$ , are multiplied respectively by  $\cos\phi$  and  $\sin\phi$  where  $\phi$  is the RD converter estimation of the position  $\theta$ . The result is subtracted and demodulated by a phase detector that utilizes the ac reference signal  $u_{ref}$ . So, a dc error signal is generated that is proportional to  $\sin(\theta - \phi)$  by the constant  $K$ . This error signal is fed to a loop filter, usually a low-pass, to estimate the analog velocity. The velocity signal is delivered to the voltage controlled oscillator (VCO). The analog integrator of the VCO outputs a pulse to a up/down counter until the final value of the counter equals the shaft angle,  $\theta$  [91]. This digitized estimated position is sampled and hold at the proper time by a latch circuit that makes it available at the user port. Some signal handshaking might be needed to read the value by the user.

Since there are two integrators in this type II RD converter (the counter counted as one integrator), the ramp signal can be tracked, but the transient performance will be poor. So, for high performance transient tracking the scheme should be modified. For example, in [91] instead of a loop filter and demodulator a bang-bang type phase comparator is suggested.

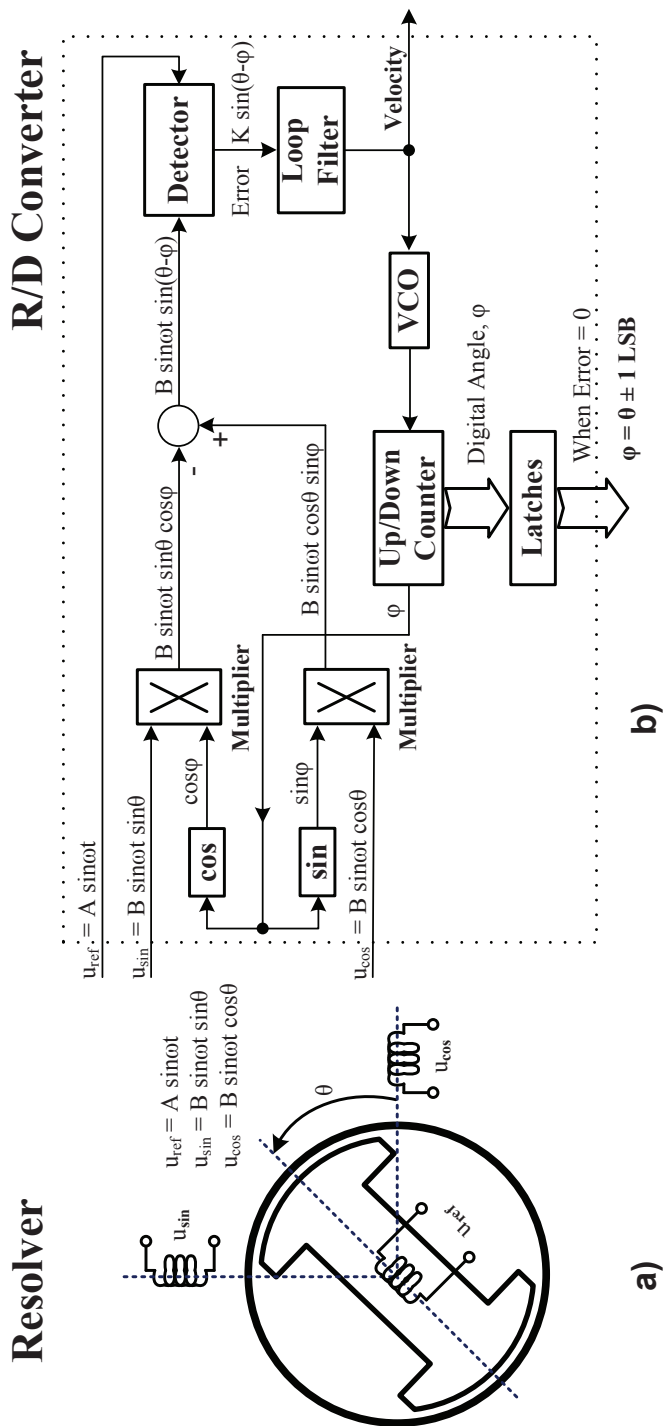


Figure 4.32: Block diagram of (a) the resolver and (b) the tracking loop of an RD converter.

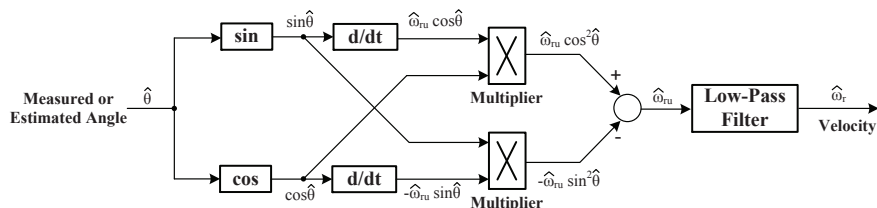


Figure 4.33: Block diagram of the proposed trigonometric open-loop velocity estimator.

## 4.5.2 The Proposed Trigonometric Velocity Estimator

For speed estimation, the open-loop position differentiation is the straight forward method that has the best dynamic performance [92], but noise amplification due to the differentiation is the main limitation of the method. A low-pass filter is used after differentiation to enhance the estimator performance with respect to the noise reduction criteria. The filter naturally imposes a time delay in the response signal. However, it is possible to optimize the low-pass filter by compromising between the dynamic performance and noise attenuation in many applications [93]. Another problem with the direct differentiation method is angle  $\pm\pi$  jumps that needs some programming and look-up table searching for proper velocity estimation [94].

When the angle changes from  $-\pi$  to  $+\pi$  or vice versa, the differentiator observes a big change in the position signal that is much bigger than the true velocity which ruins the estimated velocity signal. The controller needs to take care of those variations. As mentioned before, there are closed-loop velocity estimators that usually provide robust velocity signals concerning noise, but with a slower dynamic response compared to the direct position derivation methods. As mentioned in [92], the application type has an important impact on the selection of the suitable estimator.

### Trigonometric Velocity Estimator

Fig. 4.33 shows the proposed trigonometric velocity estimator. After reading the angle,  $\hat{\theta}$ , in digital format by the controller, the  $\sin \hat{\theta}$  and  $\cos \hat{\theta}$  are calculated. By this operation, the  $\pm\pi$  jumps are eliminated from the estimator. Two deviators, differentiate the  $\sin$  and  $\cos$  signals. After differentiations, to extract the velocity signal, the signals are multiplied by the  $\cos \hat{\theta}$  and  $\sin \hat{\theta}$  and then they are subtracted from each other. The result is the velocity signal. The basic trigonometric equation:

$$\hat{\omega}_{ru} \sin^2 \hat{\theta} + \hat{\omega}_{ru} \cos^2 \hat{\theta} = \hat{\omega}_{ru} \quad (4.4)$$

shows how the angular velocity,  $\hat{\omega}_{ru}$ , is extracted. However, because of the derivation operation, there will be amplified noise in the velocity. A low-pass filter is used to enhance the response. This filter can be adjusted by the application. For example, in the motor drive system application, usually the speed step response time is part of the specification. So, the filter bandwidth can be obtained since it is inversely proportional to the response time.

## Simulation of the Proposed Trigonometric Velocity Estimator

To evaluate the trigonometric estimator by simulations, Matlab software is used. First, a set of data are generated as true values for the velocity and position. The target application is a motor drive system, so consistent data values are generated, similar to those available in the drive system. Then the trigonometric estimator is used for velocity estimation. The result is compared with the true velocity signal to evaluate the estimator performance.

In a drive system, the motor speed is controlled by controlling the torque, and the torque is controlled by controlling the electric current in a proper way. Usually, the rotor position is needed in the controller to apply a suitable voltage to the motor to achieve this goal. The applied voltages or currents have some ripples that can be observed in the torque and speed as well. Here it is assumed that the motor is controlled in the way that the desirable torque is feasible to have. Then, it is assumed that the motor is accelerating for one second to reach to a speed that is close to  $300 \text{ rad/s}$ . Then the speed will be constant for one second. Next, the motor decelerates and the speed decreases to a negative value that is close to  $-300 \text{ rad/s}$ . Finally, the speed is constant for another second. A Gaussian noise is added to the torque signal representing torque ripple in the system. Using the mechanical state-space equations in discrete form, the velocity and angle discrete data are generated. The state-space equations are:

$$\omega_r(k) = \omega_r(k-1) + T_s T_e(k-1) + W(k-1) \quad (4.5)$$

$$\theta(k) = \theta(k-1) + T_s \omega_r(k-1) \quad (4.6)$$

where  $T_e$ ,  $T_s$ ,  $W$ , and  $k$  are the torque, sampling time, torque noise and sample time index, respectively. The sample time,  $T_s$  is  $100\mu\text{s}$  in the simulations. Moreover, the torque signal is generated according to the before mentioned speed profile. The signal  $W$  is a Gaussian noise with the covariance of  $2 \times 10^{-2}$ . The obtained angle signal is added by another noise term to represent the measurement and quantization noise. This noise level is selected to be a low value,  $1 \times 10^{-18}$  in this case.

The low-pass filter has an important impact on the the estimated speed performance in both steady-state and dynamic tracking modes. A second order Butterworth filter is used for the simulations. The filter cutoff frequency is  $100 \text{ Hz}$ .

Different simulations have been performed to evaluate the estimator where Fig. 4.34 shows some examples. The true velocity and estimated one in different time intervals, the velocity error, and the angle during the motor speed reversal interval are shown in this Fig. The simulation results show that the proposed method has a good performance in both steady state and dynamic speed tracking (the error is less than  $\pm 1\%$ ).

## Typical Experimental Results

The details of the hardware setup has been explained earlier, and here practical results are provided. The proposed velocity estimator is used in the drive system to synchronize the motor/generator with the grid voltage. Consequently, the controllers are optimized to have better performance in the application

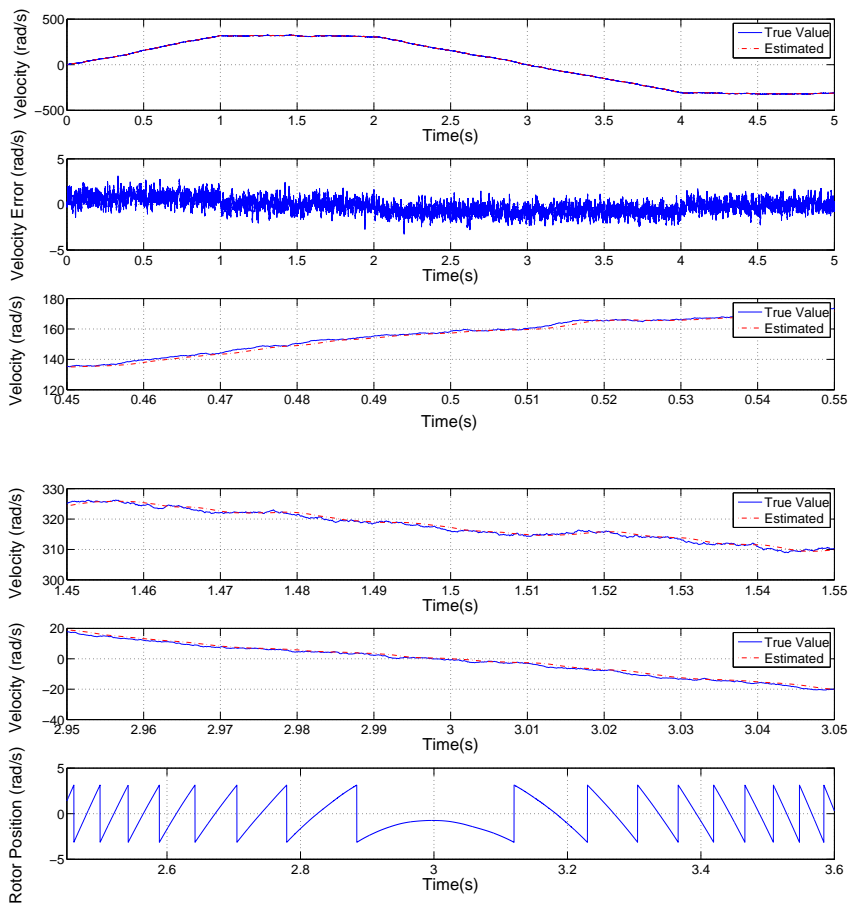


Figure 4.34: Simulation result: true and estimated speed/position by the trigonometric estimator.

context. However, to verify the proposed velocity estimator, a reference command signal is used for the velocity. The estimated velocity is tracking the command signal with a low error value in steady state (less than  $\pm 0.5\%$ ), and transient.

Fig. 4.35 shows both the reference and estimated signal of the velocity. At first the system is at stand still. Then the speed increases to  $2\pi 50$  electrical rad/s. Then it is constant for 3 s, and then it decreases to  $-2\pi 50$  electrical rad/s. Finally, the velocity command stays constant. The estimated signal is very close to the reference signal, so it is difficult to identify them from the graph. Moreover, the signals are showed in this Fig. for different time intervals during the acceleration, steady state, and deceleration as well. The electrical rotor angle is shown in Fig. 4.36 during the start up and the time that the motor changes the speed from the positive to negative.

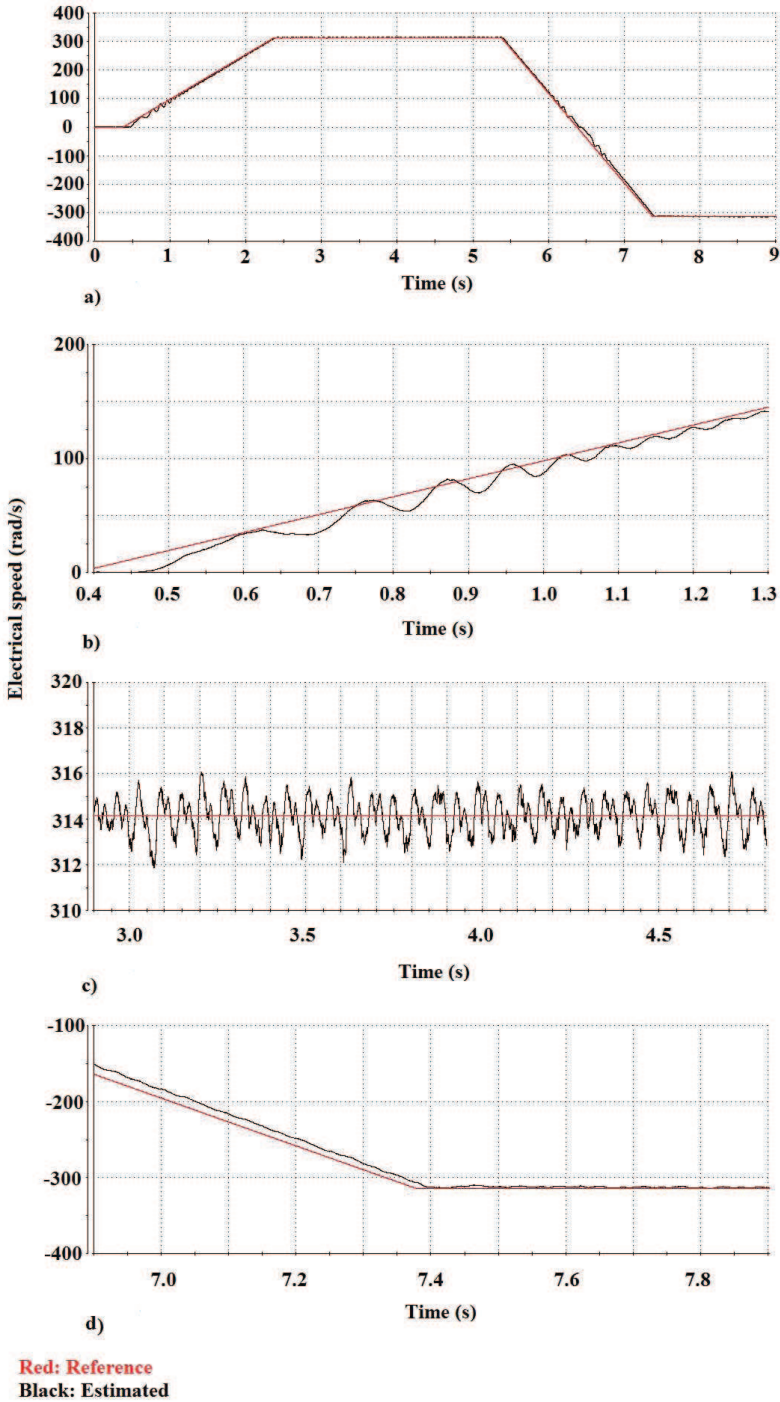


Figure 4.35: Measurement: the reference and estimated velocity in the drive system.

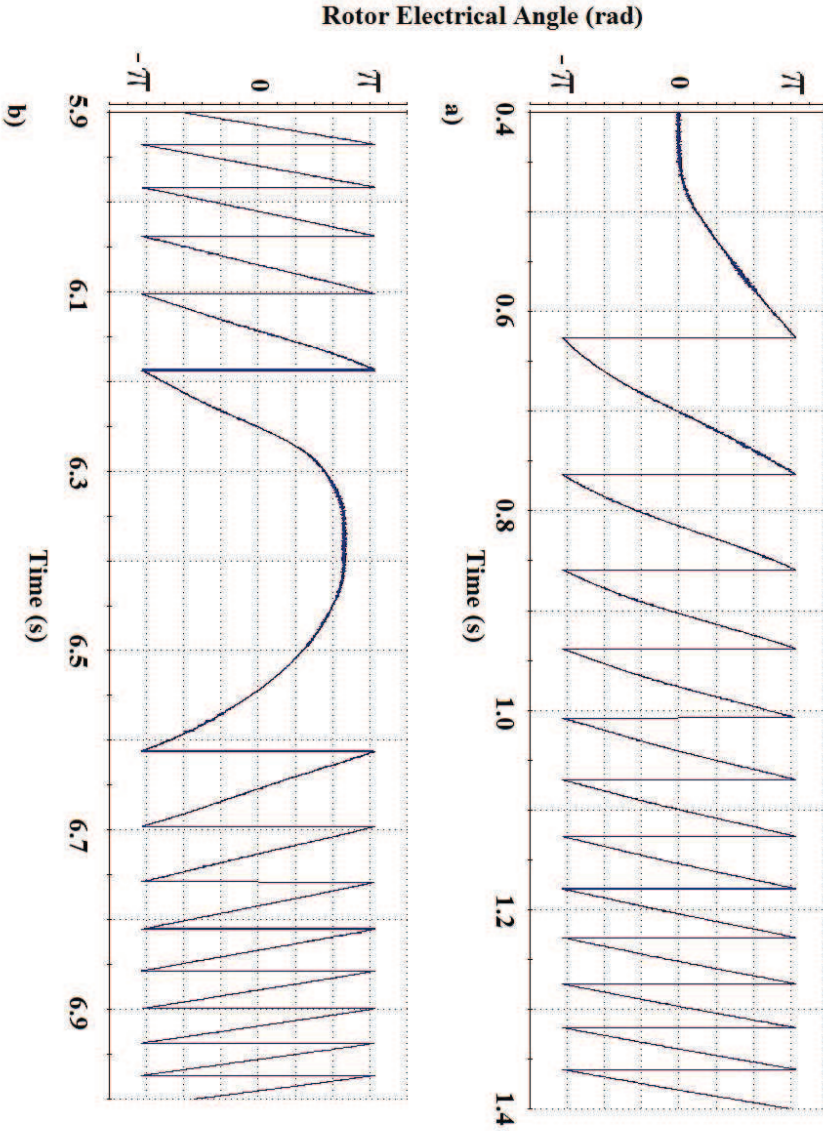


Figure 4.36: Measurement: the rotor angle during: a) start up, b) speed reversal.



## Chapter 5

# Integrated Motor Drives and Non-Isolated Battery Chargers

Non-isolated battery chargers are the first alternative compared to isolated types in vehicle applications. Recalling the related standards [4, 5], galvanic isolation is not a mandatory requirement, but it can greatly ease the safety requirements. So, the isolation is a very favorable option if the cost and space can be afforded. Consequently, the non-isolated types are very common in the market, but some considerations are needed in order to fulfil the safety requirements. Extra shielding, battery isolation from the vehicle chassis and earth path monitoring can be mentioned as challenges. More explanations are provided in [6] and in the first chapter.

In the non-isolated type of chargers, there is electrical contact between the dc output and ac line grid. Recalling different types of integrated chargers presented in chapter two, the motor is used as some inductors and the inverter switches in the charger circuit.

The main problem of using the motor is the developed torque in the motor due to the current flow in the windings. The motor may start to rotate or vibrate if the developed torque is not controlled in a proper way. So, it can be implied that zero torque is one important feature that solves these problems. For example, one solution for torque control is to use a mechanical brake as reported in [32]. If the motor starts to rotate, there will be induced back EMF that makes the control very complicated in addition to imposed extra rotational losses.

Compared to the isolated chargers, the non-isolated ones are more efficient mainly because of less components, for instance there is not an isolating transformer. Nevertheless, to have a high quality current harmonic content, usually a high-switching frequency is used in the charger. In this case the motor may not be a good inductor since the stator iron materials are not designed for high-frequency switching operation [95,96]. Consequently, it seems that these integrated chargers are less efficient compared to the conventional separate battery chargers. However, that is a compromise between integration, cost

reduction, and efficiency. Hence, in the whole electrical system design one needs to consider the integrated charging feature to modify the drive system if it is needed. For example, the stator material can be selected to have higher efficiency for battery charging operation.

The developed electromagnetic torque in an electrical machine is a function of machine current and machine structure including the geometrical features. The torque describing function can be a complicated non-linear function that depends on the machine type. For example, to encounter the magnetic saturation the torque function can be a complicated function. In most cases, there are two flux components in the machine and the torque is developed as result of interaction between these two flux components. The common flux in the mutual magnetic circuit contributes to the torque development and the leakage flux does not affect the torque function. In the case of the SRM, the energy approach is utilized to describe the developed torque in the machine. To be able to use motor as an energy storage device or isolating transformer, it is desirable to have a zero torque in the machine during the charge operation. The conceptual explanation of the zero torque condition is to use the motor as inductors where the mutual flux is zero during the charging operation. Equivalently, the leakage flux or inductance can be used as the energy storage device in the charger circuit. For example, the zero torque condition can be solved to extract the relevant condition for the currents or fluxes. Consequently, different configurations for the motor windings can be realized in order to have the motor in standstill while charging.

One disadvantage of using motor leakage inductance in the charger circuit can be low values of the leakage inductances leading to a poor power quality of the line current in terms of high THD. Increasing the switching frequency is one solution that one can immediately suggest. However, the converter and iron losses increase which needs a system level compromise in the design. Nevertheless, there are some products available in the market like the system proposed by AC Propulsion Inc. [50], which implies that the whole idea is feasible.

In this chapter, two different class of non-isolated integrated chargers are described. The first type is based on a split-phase motor, a three-phase inverter and a switching device for the windings reconfiguration. There are some variants for the proposed charger regarding the windings connection configuration. The second type is based on a split-phase PM motor with dual inverters. In the latest proposed charger, there is no need to have a switching device and it is possible to use the same hardware for the both traction and battery charging.

## 5.1 Non-Isolated Battery Chargers Based on the Dual-Windings Motor and a Switching Relay

As mentioned earlier, the main challenge of using the motor as inductors is keeping the torque zero. Assume that the midpoints of motor windings are available for each phase. This is a split-phase motor in which the phase shift

is zero between the two sets of three-phase windings.

The first scheme is shown in Fig. 5.1 for the charging and traction mode including the switching device realization. The motor windings of each phase are divided into two equivalent parts and are then reconnected inversely to cancel out the torque in the charging mode. The motor is used as three energy storage inductors in this scheme. As explained before, just leakage inductances are used and mutual fluxes are canceled out by reverse connection of the windings. The circuit topology is a three-phase Boost rectifier which is explained in detail in [18, 65] including practical implementation results.

A switching device that can be a relay for example, is used to reconfigure the motor windings for the traction and charging modes. Compared to the switching device presented in the previous chapter, this is a simple device. The second alternative is shown in Fig. 5.2 where the phase windings are connected in parallel. The electric motor can handle the current two times more than that of the first alternative. Consequently, the charging power can be increased twice compared with the first scheme, if the inverter could handle it. This figure shows the circuit diagrams in the charging, traction and integrated charging/traction modes. The last mode is a physical realization of the integrated charger. Compared to the first alternative, the switching device is simpler and the charger power level is doubled. However, the total leakage inductance in this case is lower than in the first case meaning that the current ripple is higher for the second case. More specific, if the total inductance per phase is  $2L_r$  in the first case, the second case has the total per phase inductance of  $L_r/2$  that is 4 times lower.

The above-mentioned integrated motor drive and non-isolated battery chargers are based on the three-phase Boost rectifier. The main limitation of the rectifier in this topology is that the dc output voltage should be more than the peak line voltage to have unity power factor operation. So, a DC/DC converter is shown as an option in this case for the case that the battery voltage does not meet this requirement. Moreover, the DC/DC converter provides a more freedom in control during the charge and discharge cycles. Another advantage is that the motor design is a simpler task since the dc bus voltage is a constant value.

Unity power factor operation is one feature of the proposed chargers. However, there might be a need to add a small line filter to meet the THD requirements during the battery charging operation.

Another advantage of the circuit is bidirectional operation capability. Hence, it is possible to use the vehicle for G2V applications.

As is shown in the figure, just a simple switch is needed to convert the traction mode to the charging mode operation. Moreover, both three-phase and single-phase supplies can be connected to the circuit without any changes in the hardware in charging mode. However, there are some changes in the control algorithm for this purpose.

To validate the proposed schemes experimentally, the split-phase PMSM explained in the previous chapter with the power level of 1 kW is used in a three-phase rectifier circuit. By feeding the three-phase and single-phase sinusoidal waveforms, the motor is in stand still and charging operation is normal. So the motor is successfully used as three independent inductors according to the above mentioned configurations.

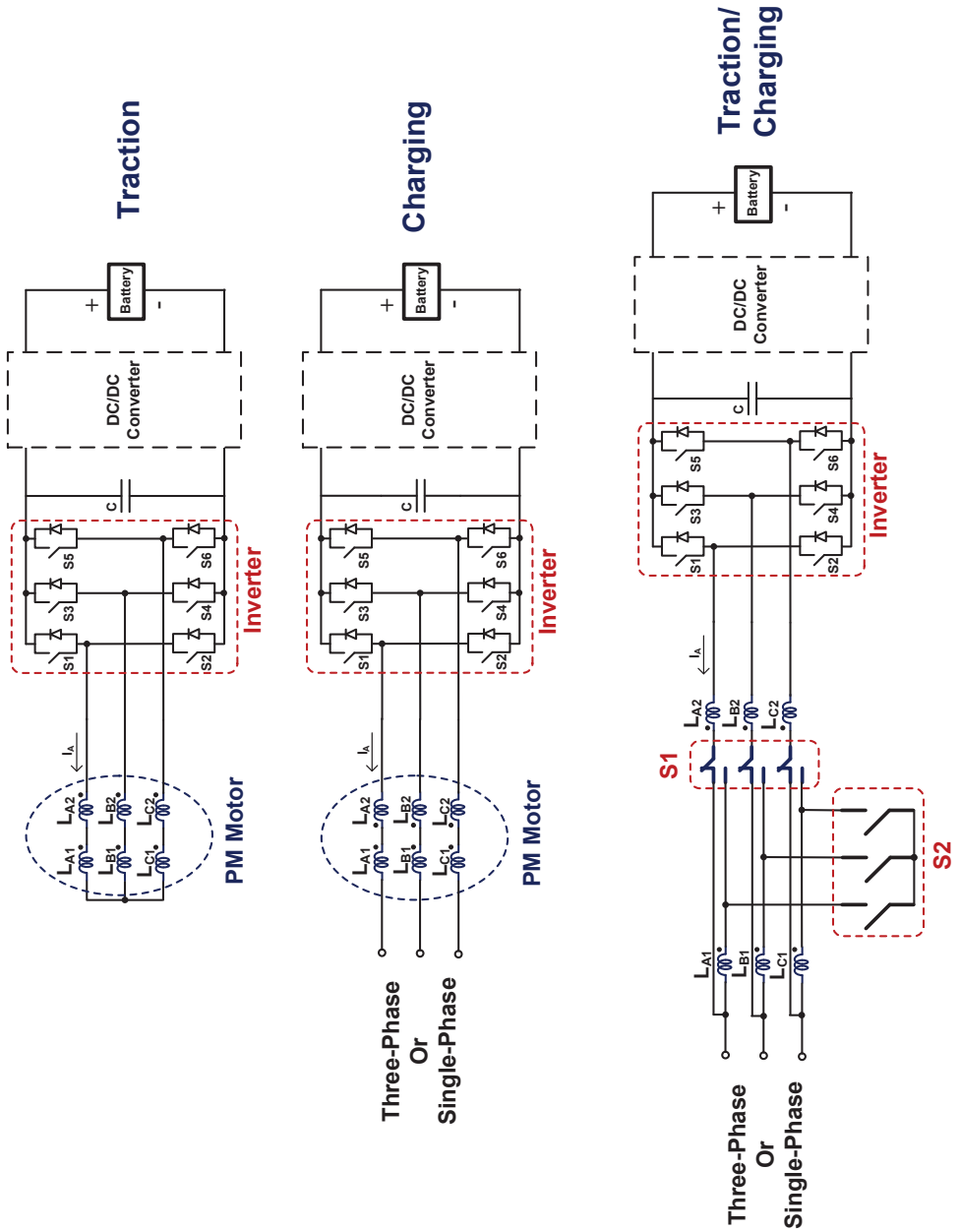


Figure 5.1: Non-isolated battery charger based on the dual-winding motor and a switching device: the charge power is equal to the traction power.

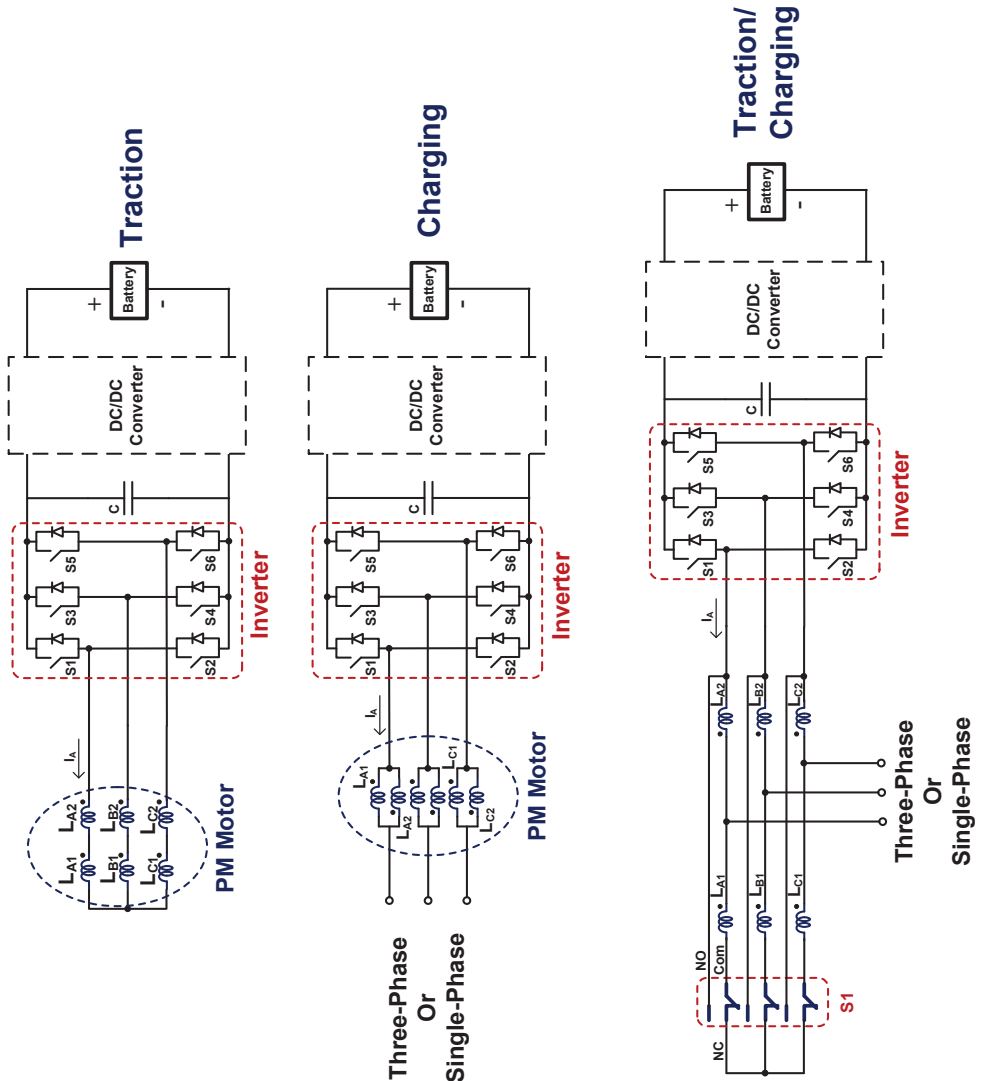


Figure 5.2: Non-isolated battery charger based on the dual-winding motor and a switching device: the charge power is twice of the traction power.

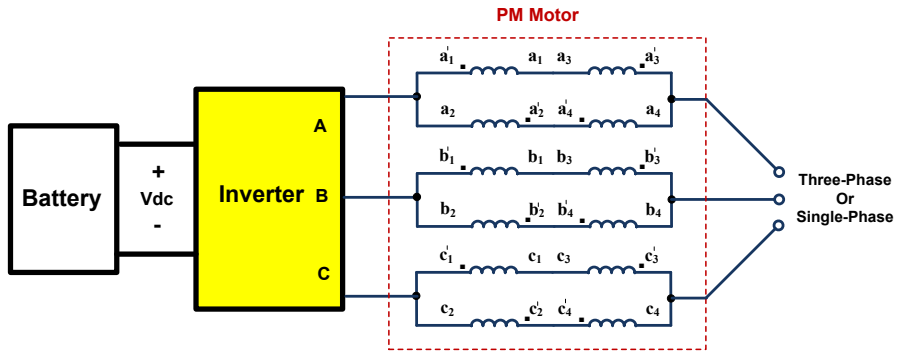


Figure 5.3: Non-isolated battery charger based on the split-phase 20 kW PM motor with the parallel connected windings.

## 5.2 Non-Isolated Battery Chargers Based on the Split-Phase PM Motor and a Switching Relay

It is possible to implement the before mentioned non-isolated charger schemes for the split-phase PM motor with an arbitrary phase shift between the two sets of the stator windings too. As long as the zero torque condition can be held in the motor during the charge operation, it is possible to use the split-phase PM motor inductances in the charger circuit. If the same current is flowing into the two sets of windings with opposite directions, the developed torque is ideally zero. However, because of the windings harmonic contents or variable rotor position dependent phase inductances, there is a winding's current limitation that reduces the maximum charge power. In this case, by reducing the charge power, one can reach an acceptable level of the performance for the battery charging. For the 20 kW IPMSM explained in previous chapter in section 4.3, a non-isolated integrated charger is proposed (Fig. 5.3) that is similar to Fig. 5.2. Winding configuration, finite element method (FEM) simulation results, Matlab simulation results and practical measurements show that the proposed scheme is practically feasible.

Fig. 5.3 shows the proposed system in charging mode for the 20 kW IPMSM in which the parameters are presented in Table 4.2. The polarity of windings is such that the developed torque is ideally zero. However, for this PM motor, because of winding's space harmonics, the maximum current in each winding is measured to be half of the rated value before reaching a high level audible noise. So, a maximum total current of 15  $A_{rms}$  is permissible for the battery charging that is equivalent to a power level of 10 kW for a three-phase system. The motor audible noise is the main limitation to increase the battery charging power level for this motor.

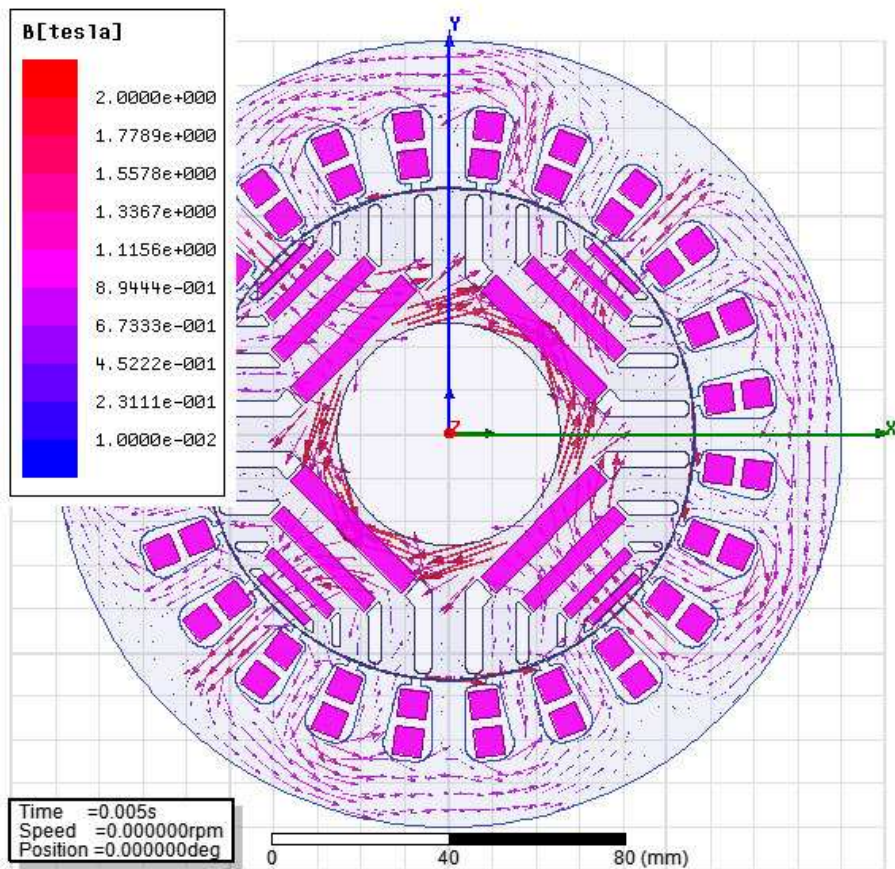


Figure 5.4: Simulation result: magnetic flux density distribution in the 20 kW IPMSM during battery charging in non-isolated charger with a sinusoidal current supply.

### 5.2.1 Non-Isolated Integrated Charger Based on the Split-Phase PM Motor: FEM Simulation Results

Ansoft/Maxwell software package is used to perform simulations for the motor during battery charging. A symmetrical three-phase sinusoidal current with a peak value of 9 A and a frequency of 50 Hz is assumed for the motor. Simulation has been conducted for the different rotor positions while the motor is in standstill. Fig. 5.4 shows the basic geometry and magnetic field distribution for the time instant that the phase A current is in the maximum value ( $t=5$  ms). As is shown in the figure, the motor laminations are exposed to a variable flux density. Consequently, there is a magnetic core loss in laminations during the battery charging.

Fig. 5.5 and 5.6 show the motor phase A inductance and the developed electromagnetic torque for different rotor positions. Both the inductance and torque are varying when the rotor position is changing. For a three-phase boost converter, the inverter controls the motor currents, so the inductance

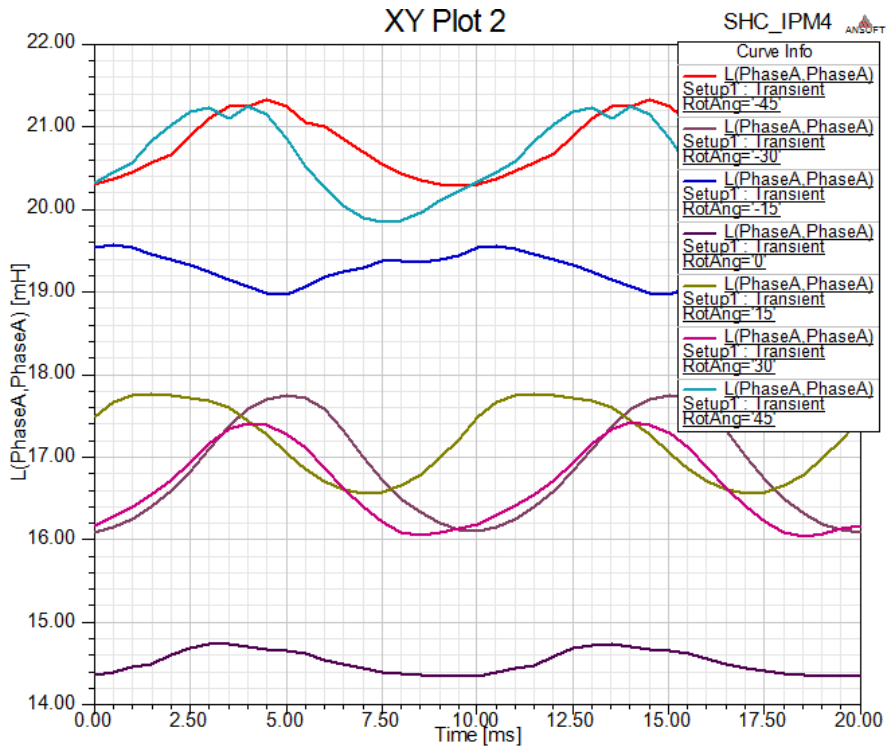


Figure 5.5: Simulation result: Phase inductance in the 20 kW PM motor during battery charging in non-isolated charger with a parallel connected winding arrangement.

variation is not critical and a proper control operation can reduce the adverse impact. Compared to the nominal torque that is  $127 \text{ Nm}$ , the developed torque is small. Moreover, the average torque is close to zero which means the motor will be in standstill during charging, but there will be an audible noise when the magnitude of the the torque is high. As mentioned earlier, for this motor when the current is more than the half of the rated value, the motor starts to sound.

For a three-phase rectifier, the value of inductor can not be too low or too high. The first one, causes a large THD value and the second one, makes the control and power transfer difficult because of large voltage drop on the inductor. By connecting the motor windings in series or parallel, designer has the option to select the inductor value that is close to the desirable one. However, there are other parameters in the system, like switching frequency, that will impose other constraints on the charger. So, more considerations than the inductor value is needed in the system design stage.

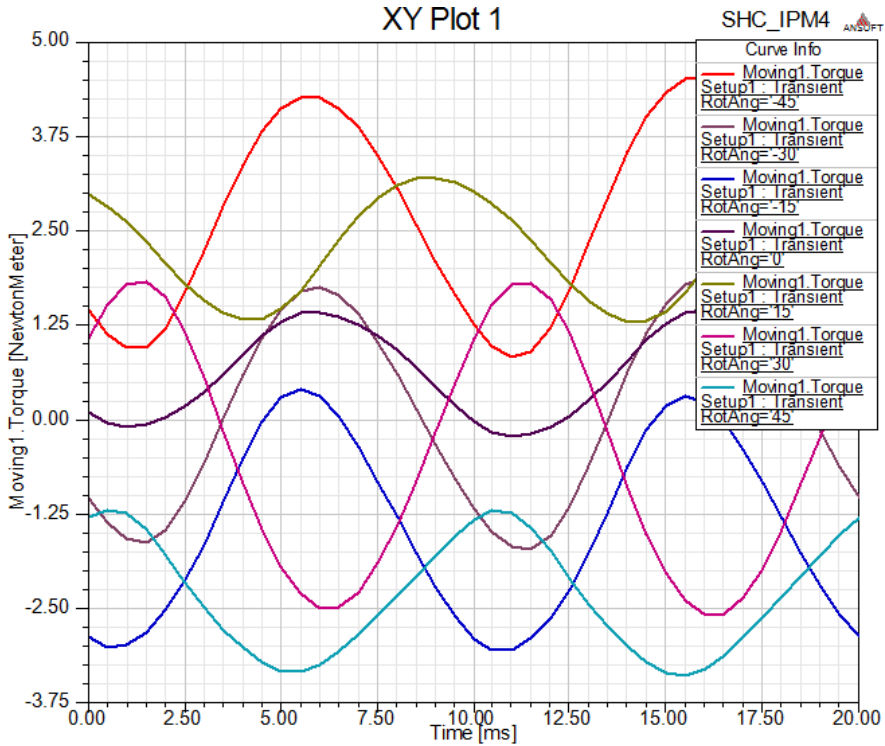


Figure 5.6: Simulation result: developed torque in the 20 kW PM motor during battery charging in non-isolated charger with a parallel connected winding arrangement.

### 5.2.2 Non-Isolated Integrated Charger Based on the Split-Phase PM Motor: Practical System Results

To verify this non-isolated integrated charger a simple practical system is developed which the motor is used as the three inductors. Fig. 5.7 shows the system configuration and Fig. 5.8 depicts a photo of the system. The three-phase or single-phase supply is connected to the motor and then to a bridge rectifier. A large capacitor, 3300  $\mu F$ , reduces the ripple on the dc bus. The motor behavior, like audible noise and waveforms, are studied in this setup. The main reason of using this system is simplicity and easy control. Testing in a three-phase boost rectifier with full control features like current limit operation is expected for the next step.

This bridge rectifier is a naturally commutated rectifier that one can find detail explanations in classical power electronics textbooks [97]. Fig. 5.9 shows the measured supply voltage, line (motor) current and motor voltage. As is shown in this figure, the waveforms are heavily distorted due to the grid frequency rectification and diode rectifier operation. To calculate the motor phase inductance, the rms values of the motor's voltage and current are calculated by use of the measured and recorded data. The calculated value of the induc-

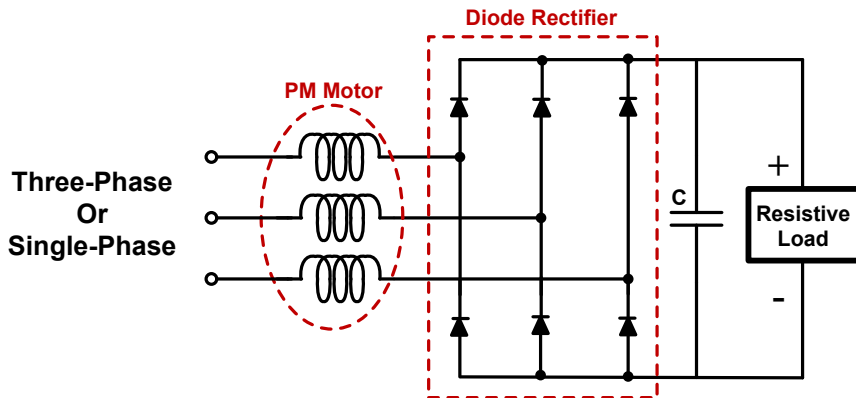


Figure 5.7: Main diagram of the practical setup of the non-isolated integrated charger.

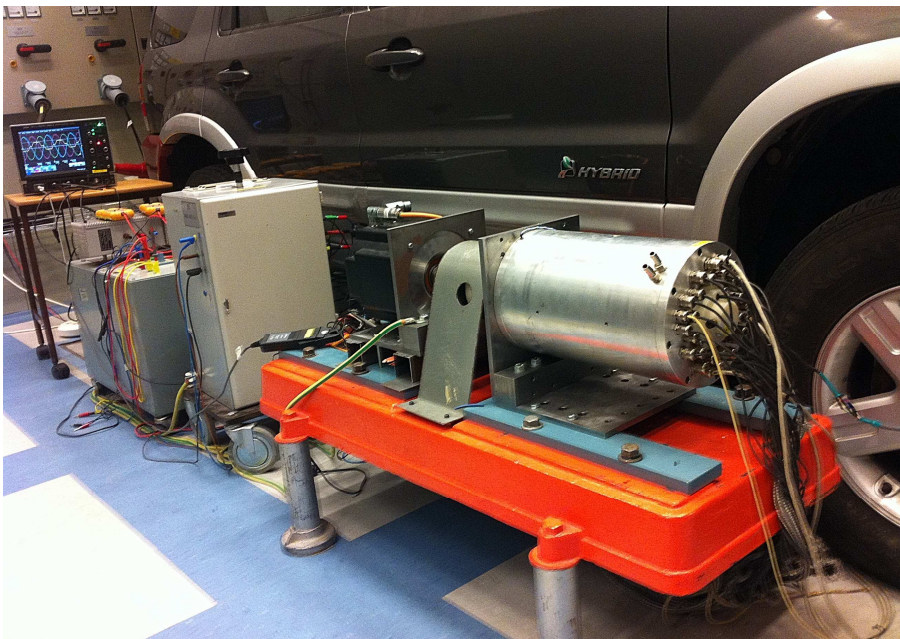


Figure 5.8: Practical setup for testing the non-isolated integrated charger for the 20 kW PM motor.

tance is  $7\text{ mH}$  that is lower than the value simulated in FEM (see Fig. 5.5). However, the calculated value using the measurement data, is based on the assumption that the voltages and currents are pure sinusoidal.

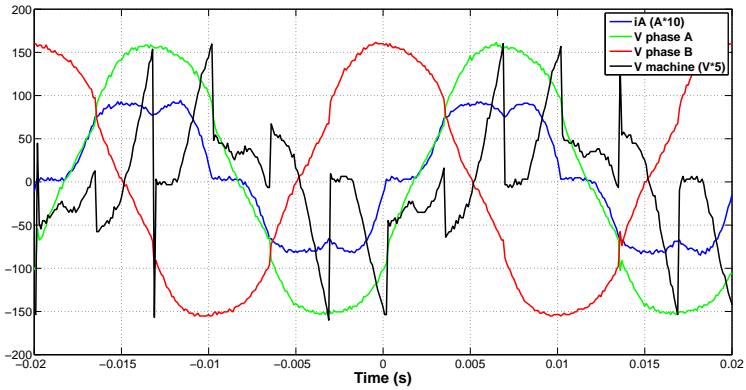


Figure 5.9: Measurement: supply voltage and motor waveforms of non-isolated integrated charger in the bridge rectifier setup.

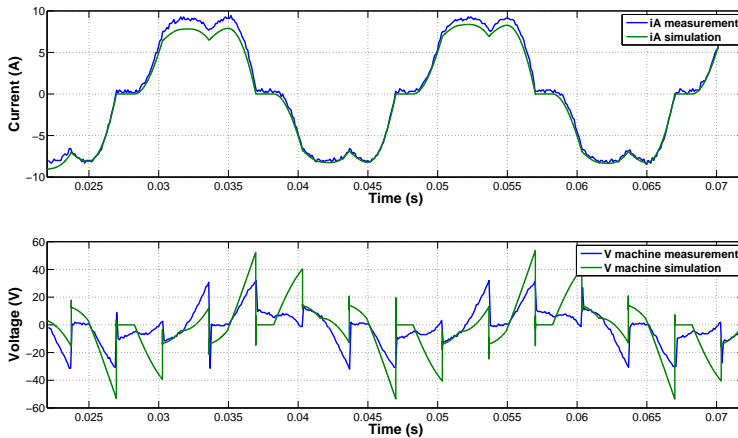


Figure 5.10: Measurement and simulation: measurement and Matlab simulation of the motor phase voltage and current of non-isolated integrated charger in the bridge rectifier setup.

The rectifier system is simulated in Matlab/Simulink using Power System Blockset. The calculated value of the inductance,  $7\text{ mH}$ , is used in this simulation. Fig. 5.10 shows one phase of the motor current and voltage for both the measurement and Matlab simulation. The current waveforms are very similar, but for the voltage there is a difference. The inductor voltage is the derivative of the current that is a noisy operation that can be one reason of the difference in addition to winding's space harmonics.

### 5.3 Integrated Motor Drive and Non-Isolated Battery Charger Based on a Split-Phase PM Motor and Dual Inverters

Multi-phase machines have some features such as reduced power electronic components rating, reduced torque ripple, and increased reliability that make them a favorable option in some applications, for instance in the area of high-power drive systems. However, in the next chapter more information regarding this topic is provided and in this chapter just the application of an integrated battery charger is considered. A combined motor drive and non-isolated battery charger based on a split-phase PM motor and dual inverters is proposed and explained in this section. By connecting the two motor winding star points to a single-phase ac supply, it is possible to charge the battery through the inverters from a commonly available single-phase outlet. In this way, a separate battery charger is not needed.

In a two-pole three-phase PM motor, there are three windings in the stator that are shifted 120 electrical degrees. In the split-phase PM motor, each phase winding is divided into two equivalent parts and are shifted symmetrically around the stator periphery as is explained in chapter 2. It is possible to connect each set of the three-phase windings to a separate inverter. If two windings are exactly the same, the same inverters can be used, and then each can provide half of the motor power in the traction mode. It is assumed that the null points of these two three-phase windings are not connected to each other, and the reason is explained in the next chapter. Fig. 5.11 shows the proposed integrated motor drive and battery charger based on the split-phase PM motor with dual inverters. As is shown in the Fig., the single-phase ac source is connected to the neutral points of the windings for battery charging and there is no need for extra switching devices.

In the traction mode, the two inverters power the motor by using FOC. The system dc bus and two phase currents of each three-phase windings are measured by the controller. The speed control is performed based on the MTPA method that has been extended for the proposed system from a classical machine model to a double  $dq$  model one. For battery charging, the source is connected to the motor two neutral points,  $n_1$  and  $n_2$ , by a plug. The motor windings are used as inductors to form a single-phase full-bridge Boost rectifier by using the available power semiconductors in the inverters. Since the component power rating are usually high for traction purposes, the charger is a high-power non-isolated battery charger.

#### 5.3.1 System Operation in Traction Mode: FOC of Split-Phase PM Motor

A simple diagram of the drive system in the traction mode is shown in Fig. 5.12. The reference speed is compared with the measured or estimated speed to provide the speed error signal. A  $PI$  controller processes the speed error. The output is a proper torque reference signal to achieve the desired speed control performances. The torque development is made by indirect current control of the machine in the direction of  $d$  and  $q$  axes. For the PM motor, to obtain

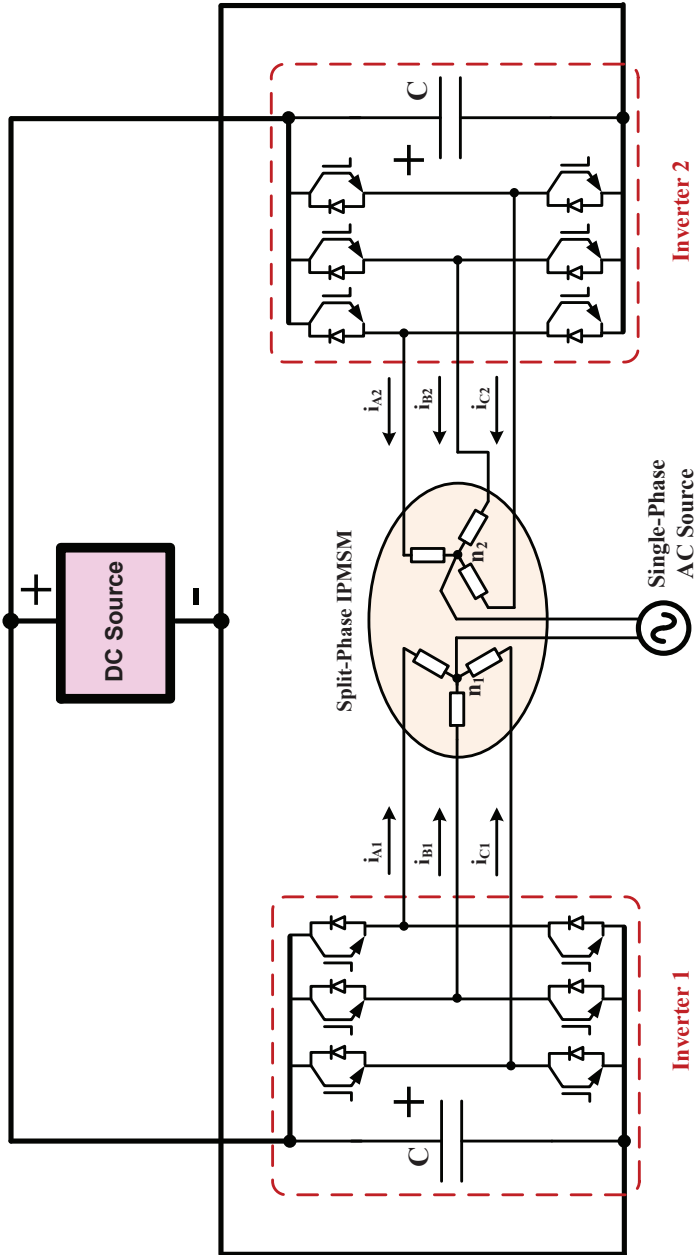


Figure 5.11: Integrated motor drive and non-isolated battery charger based on the split-phase PM motor and dual inverters.

the reference values for the current controllers, the MTPA strategy is utilized that is explained in the next chapter.

The reference values for the  $dq$  components of the current are calculated in the MTPA section, where can be stored as a look up table. The two sets of windings have identical  $dq$  reference values because of the symmetry. The reference values are input to four independent current regulators. Two phase currents out of three are measured for each set of windings to calculate the  $dq$  components of the currents respectively. The measured current components are compared with the reference values. The error signals are fed to the  $PI$  regulators for fast current control action. The current controllers' output signals are inputs to the decoupling network to cancel out nonlinear terms in the controller by feeding-forward the proper signal.

The output of the decoupling network is  $dq$  reference voltages for each inverter. Using the rotor angle, these  $dq$  values are transformed into the  $\alpha\beta$  stationary reference frame values. Here, it is assumed that the position signal is available by a sensor like a resolver or an encoder.

In the case of a failure in one set of windings or in one inverter, the second one can continue to operate without any change, but an adjustment of the torque reference value is needed since the motor can no longer provide the rated torque. So, the system is fault-tolerant to some extent. A dc bus failure will shut down the drive system because the two inverters are connected to the same dc bus.

### 5.3.2 System Configuration in Battery Charging Mode

The system configuration in battery charging mode and its simplified diagram is shown in Fig. 5.13. The vehicle is connected to the single-phase power source, the utility grid or other sources, through a plug. The battery charger topology is a single-phase full-bridge Boost converter [16]. This configuration is a non-isolated bidirectional topology which has the possibility to feed power back from the battery to the grid if required. However, the electromagnetic compatibility issues need to be considered carefully for the proper converter operation and safety reasons to avoid frequent tripping of the earth-fault monitoring system.

The top and bottom switches for each inverter are operating simultaneously. So, each inverter operates like a leg with two switches. For example, the switch  $S_1$  is equivalent to switches  $S_{11}$ ,  $S_{13}$ , and  $S_{15}$  if they operate simultaneously. The grid supply is connected to the neutral points of the motor, so the total current entering each winding is equal to the other one. Moreover, with simultaneous switching in the top and bottom switches, the currents are equal in each phase. Consequently the developed torque in the motor is zero and the motor does not turn during the charge operation. So it is not needed to use a mechanical brake during battery charging.

It might be needed to add a small line filter to enhance the current waveform. There are different methods for the converter control [98–101]. For example, a hysteresis current control of the inductor current is employed where a unity power factor operation is feasible too.

During the charge operation, the total emf of each three-phase winding is zero, which means there is no magnetic stored energy in the motor iron, so

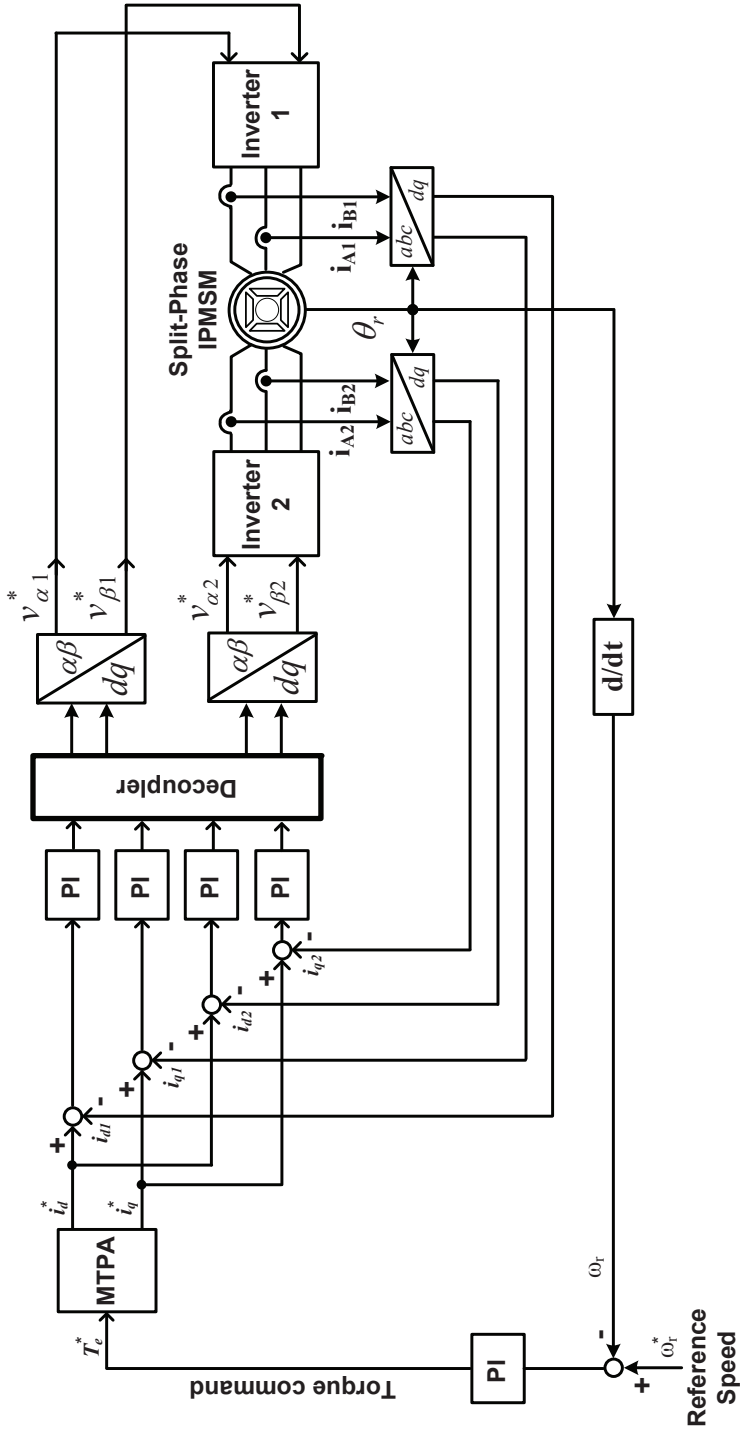


Figure 5.12: FOC of a split-phase PM motor with dual inverters using MTPA for the traction mode.

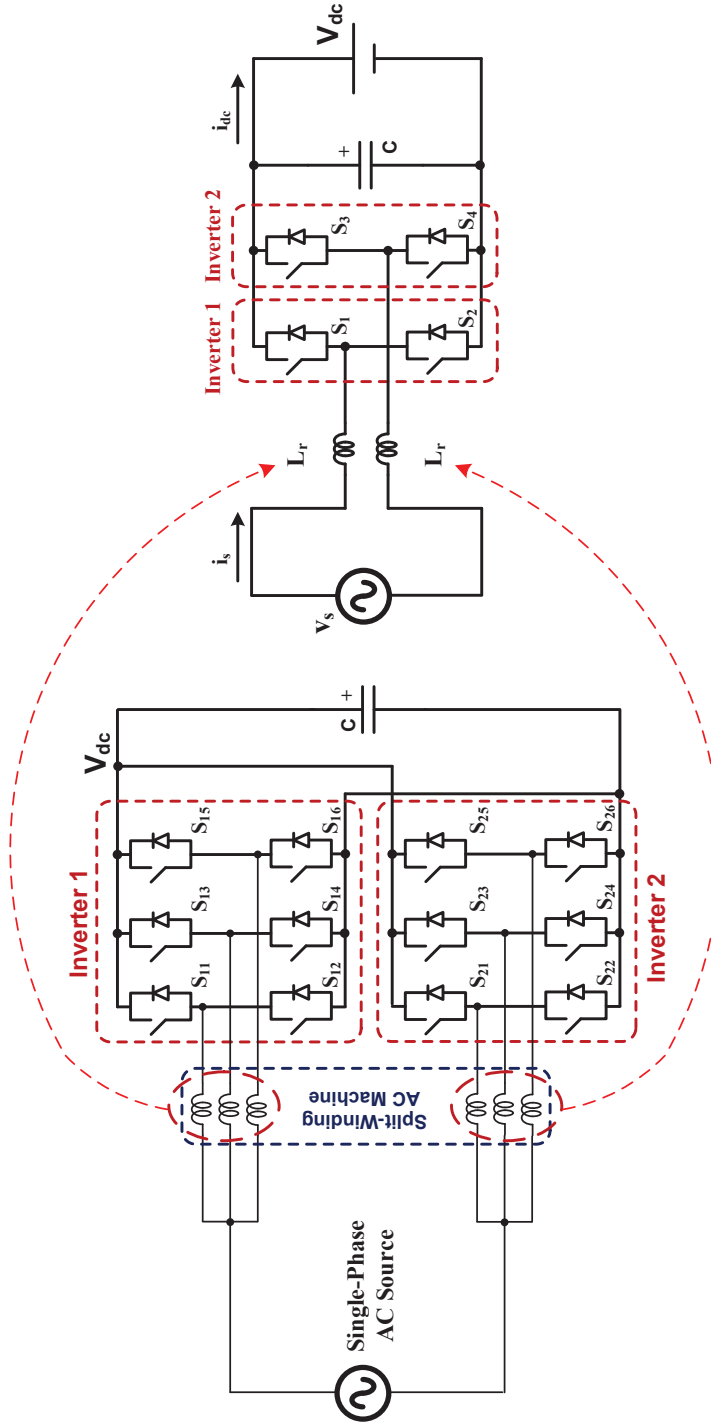


Figure 5.13: Integrated battery charger based on split-phase PM motor and dual inverters in battery charge mode.

just leakage inductance of the windings are used as the energy storage devices in the converter circuit. For the constructed 20 kW split-phase PM motor whose are used in the simulations, the leakage inductance of each winding is 1.5 mH. So the equivalent inductance, three-parallel leakage inductances,  $L_r$ , is 0.5 mH for each three-phase winding. Since there are two sets of three-phase windings, the total inductance in the ac supply-side is 1 mH. The system dc bus voltage is 500 V. The charger components are rated for the traction operation, so the charger is a high-power device. Theoretically it is possible to charge the battery with 10 kW, but practically the single-phase sources are usually limited to a few kilo watts. However, the separate battery charger is eliminated in the system which has an important impact on the system cost.

### 5.3.3 Simulation Results for Charging Mode

The system in charging mode is simulated by using the Ansoft/Simplorer software package. The single-phase grid voltage is 230 V<sub>rms</sub>. The motor windings are replaced by the leakage inductances in the simulation as mentioned before. The dc link is connected to a battery, so it is not needed to regulate the dc bus voltage by the controller. For the bulk battery charging, the charger is charging the battery by a constant current. Equivalently, this current is equal to a desired constant power level considering the battery voltage.

If we assume that the converter is ideal and is operating with unity power factor, it is possible to calculate the magnitude of the current value of the ac source. To provide a reference current for the converter, the ac source voltage is measured to make a sinusoidal reference waveform. The reference current is proportional to the voltage by a power conversion constant. For simulation, a hysteresis current control is utilized to follow this reference current. The reference current is compared to the measured current. Then, to increase the line current, the inverter switches make a short-circuit to charge the inductor and after reaching the upper hysteresis band, the switches de-charge the inductor energy to the output capacitor and the battery considering input voltage polarity.

Fig. 5.14 shows the grid current and voltage during charge operation. At the beginning the charging power is 2.5 kW, and after 35 ms the power increases to 10 kW. Unity power factor operation can be seen from the Fig. Moreover, the current waveform for different time intervals are show in Fig. 5.15 and 5.16. The hysteresis upper band and lower band for the current controller are 1 A in this case.

The battery voltage is constant during a few switching instants with a good approximation, so naturally the current ripple in the dc side can be high. The dc bus capacitor value determines the current ripple in the battery during the charge operation. However, high dc link capacitor values can not be afforded due to the space and cost impact. A compromise has to be done between the current battery ripple and capacitor value.

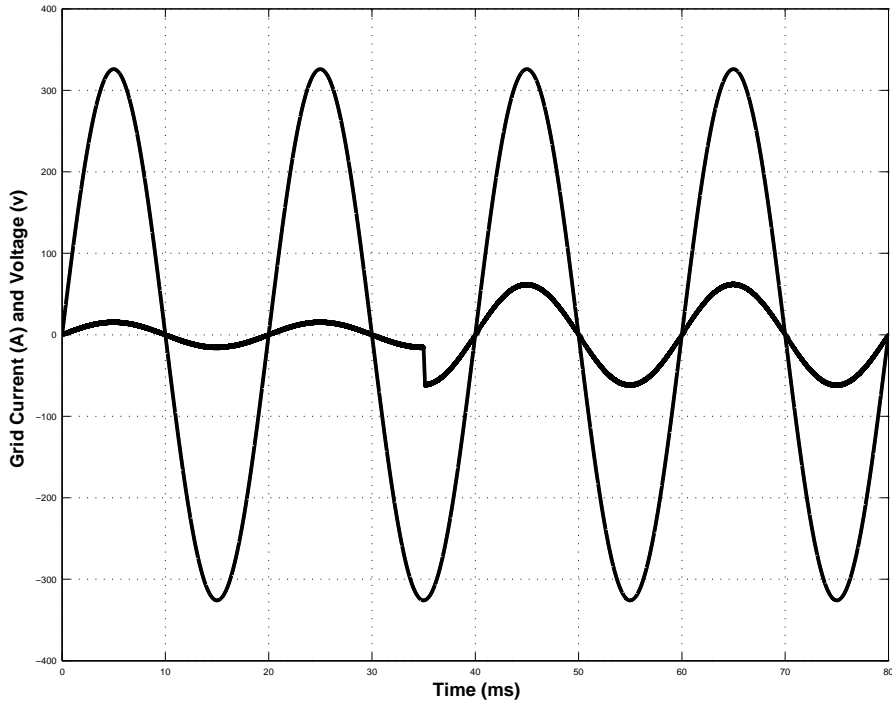


Figure 5.14: Simulation result: grid current and voltage during battery charging for a charge level step change from 2.5 kW to 10 kW.

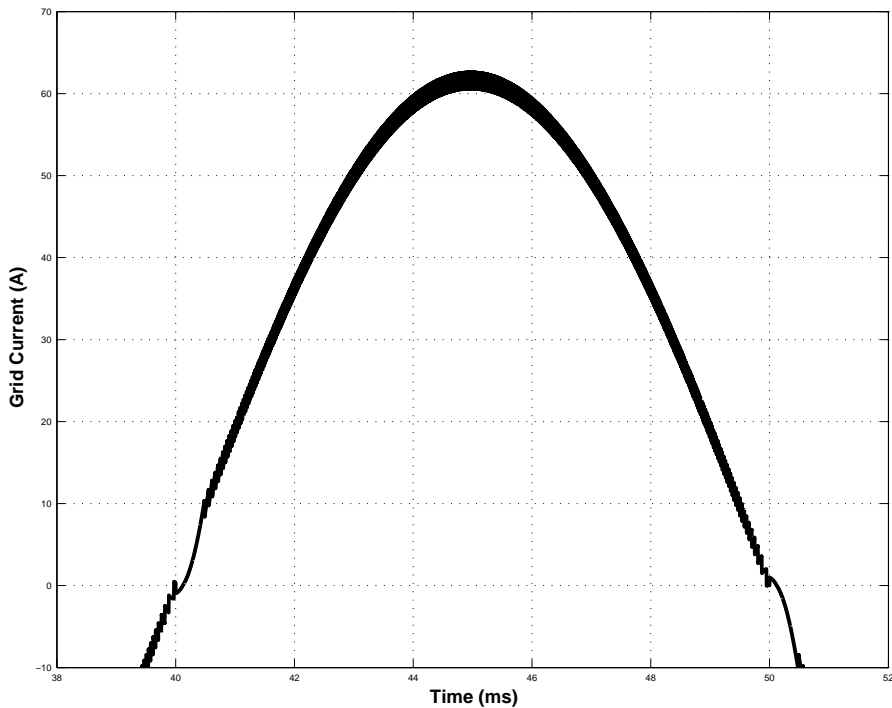


Figure 5.15: Simulation result: grid current during battery charging for grid half period.

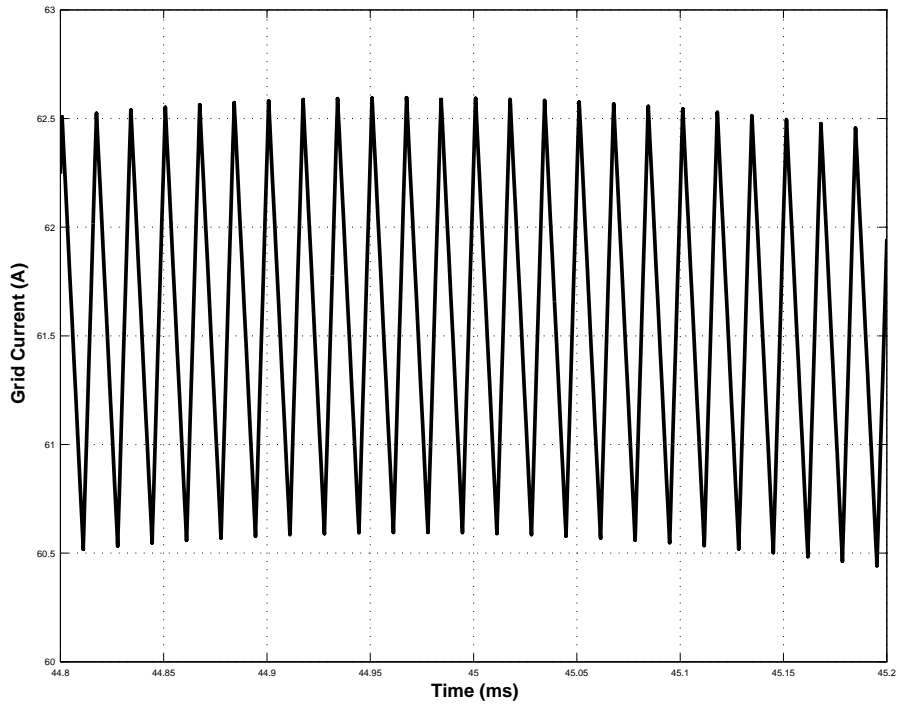


Figure 5.16: Simulation result: grid current during battery charging for a few switching periods.



## Chapter 6

# Modal Field-Oriented Control of a Split-Phase PM Motor with Dual Inverters

As mentioned earlier, multiphase motors have many advantages compared to classical three-phase machines like a higher efficiency, a greater fault tolerance, a lower torque ripple, and a reduced power electronics component rating [58]. One important disadvantage of the multiphase drive system is that the control is more complicated than that of the classical three-phase drive systems. The aim of this chapter is to give a systematic frame-work for designing a high-performance controller for the drive system based on the split-phase PM motor and dual inverters. The methodology, modal control by eigenvalue decomposition, is a very strong tool resulting from the linear system theory and is well established in the control community.

Split-phase electric motors have two similar stator windings that share the same magnetic circuit, but are shifted in space. The total power is equivalently shared between two windings by using two separate three-phase inverters [60]. For the induction motors, this scheme is widely studied and is used in industry [61, 102–105]. Permanent magnet motors are recently started to be utilized in multiphase motor drive applications too [106, 107].

Different types of drive systems are reported for multiphase motors [58, 59] like direct torque control or vector control. For induction motors there are many reports addressing the speed control, but for the PM motors more work is expected. FOC and its variations are widely used in industrial drive applications, and usually are considered as high-performance solutions. There are more than three sets of windings in the stator, so there is a tight coupling between the stator flux components that needs special consideration for the control. Usually decoupling networks are used to achieve an acceptable controller performance.

As an example, FOC is used for an induction motor [102] with double stator windings where the error of the two stator currents are used in the controller.

The current difference signal is used in controller to keep the balance between the two sets of stator windings. Luca De Camillies et. al. published a paper regarding the double winding induction motor control in 2001 [108]. To cancel out  $d$  and  $q$  axes coupling, an eigenvalue assignment method is exploited to enhance the control scheme that is based on the FOC. The decoupling procedure is done in two steps: at first the coupling between  $d$  and  $q$  equations are canceled out and then the dynamics between the two stator windings are decoupled. However, the motor time constants are not directly engaged in the design process.

In this work, a similarity transform is used to decompose the system's state-space model to its modal form (eigenvalue diagonalized system) for decoupled control. As is shown later on, new variables are evolved from this transformation that are summation and negation of the  $d$  and  $q$  components of the stator currents. A decoupled model is achieved that based upon the classical FOC is modified. Moreover, the system eigenvalues, the inverse of motor time constants, provide more information on the system dynamics. For example, the required bandwidth of the controller can easily be calculated in this method to reach an acceptable transient performance for the fastest dynamics in the motor. However, the feedforward term is utilized to enhance the control. Consequently one advantage of this work is to introduce a framework to be able to design the  $PI$  current controllers in a systematic way and avoiding trial and error procedures by using similarity transformation.

In addition to presented control scheme for the drive system, an MTPA is presented for the split-phase PM motor drive using a double  $dq$  approach to derive the  $dq$  current references for the speed control loop. Computer simulations are performed to verify the proper operation of the system for the speed control.

## 6.1 Drive System of the Split-Phase PM Motor with Dual Inverters

In a two-pole three-phase PM motor that can be of an IPMSM type, there are three windings in the stator that are shifted 120 electrical degrees. In the split-phase IPMSM, each phase winding is divided into two equivalent parts and are shifted symmetrically around the stator periphery. Basically, there will be six windings inside the stator, instead of three, for a two-pole machine. It is possible to connect each set of the three-phase windings to a separate inverter. If two windings are exactly the same, the same inverters can be used, and then each can provide half of the motor power. It is assumed that the null points of these two three-phase windings are not connected to each other.

Fig. 6.1 shows the structure of the drive system that is comprised of a split-phase IPMSM, two independently controlled inverters, some measurement sensors and the controllers.

In the case of a failure in one set of windings or inverters, the drive system is able to continue with half-power. However, in the case of failure in the dc bus, the operation can not be continued. The two stator windings are tightly coupled to each other because they are using the same stator iron path. So if there is a short circuit in one set of windings, it is not possible for the second

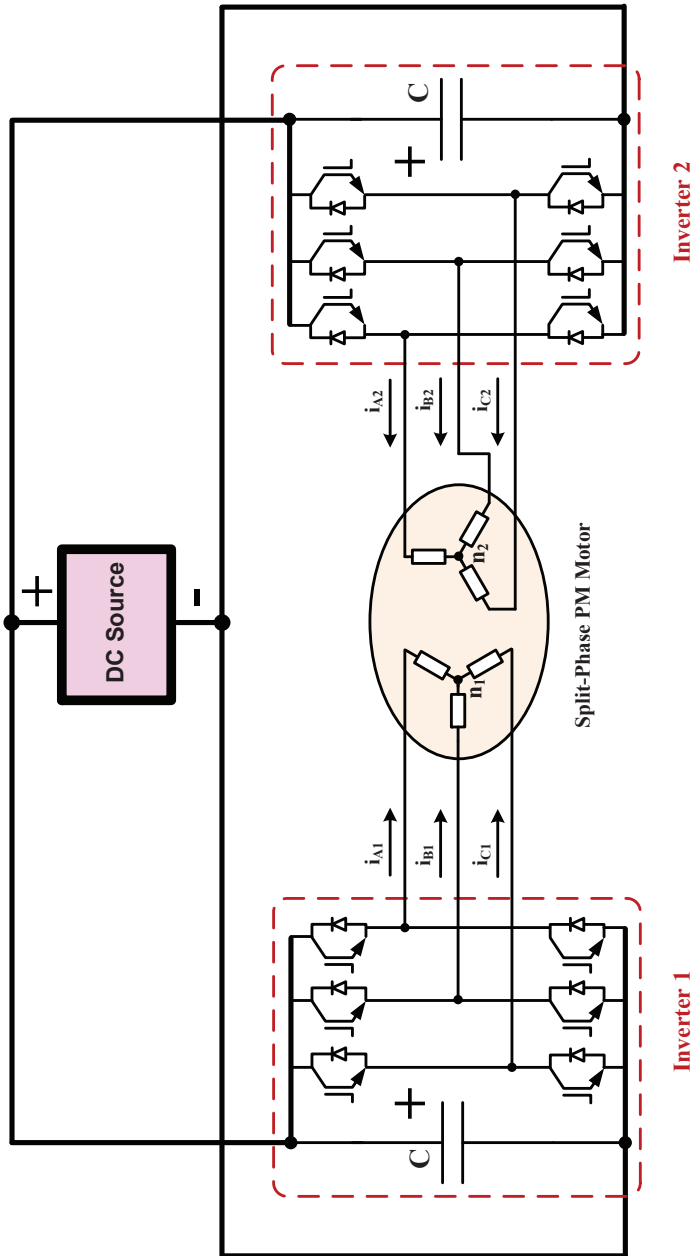


Figure 6.1: Drive system structure of the split-phase PM motor with dual inverters.

set of windings and related inverter to continue driving even at reduced power. There might be high-current levels in the system causing severe damage to the motor or inverter. The symmetrical geometry of the motor can be considered as an advantage. It can be assumed that in steady state the currents and voltages have the same rated values in the two sets of windings and inverters. This assumption simplifies the controller design.

## 6.2 Modal State-Space Model of the Split-Phase PM Motor

The mathematical model of the split-phase PM motor is described in chapter 3 including the electrical and dynamical equations. Nevertheless, the equations are again presented here for more convenience. The dynamic equations are

$$v_{d_1} = r_s i_{d_1} + \frac{d}{dt} \psi_{d_1} - \omega_r \psi_{q_1} \quad (6.1)$$

$$v_{q_1} = r_s i_{q_1} + \frac{d}{dt} \psi_{q_1} + \omega_r \psi_{d_1} \quad (6.2)$$

$$v_{d_2} = r_s i_{d_2} + \frac{d}{dt} \psi_{d_2} - \omega_r \psi_{q_2} \quad (6.3)$$

$$v_{q_2} = r_s i_{q_2} + \frac{d}{dt} \psi_{q_2} + \omega_r \psi_{d_2} \quad (6.4)$$

$$\psi_{d_1} = L_d i_{d_1} + L_{md} i_{d_2} + \psi_{pm} \quad (6.5)$$

$$\psi_{q_1} = L_q i_{q_1} + L_{mq} i_{q_2} \quad (6.6)$$

$$\psi_{d_2} = L_{md} i_{d_1} + L_d i_{d_2} + \psi_{pm} \quad (6.7)$$

$$\psi_{q_2} = L_{mq} i_{q_1} + L_q i_{q_2} \quad (6.8)$$

where  $v_{d_1}$ ,  $v_{d_2}$ ,  $v_{q_1}$ ,  $v_{q_2}$ ,  $i_{d_1}$ ,  $i_{d_2}$ ,  $i_{q_1}$ ,  $i_{q_2}$ ,  $\psi_{d_1}$ ,  $\psi_{d_2}$ ,  $\psi_{q_1}$ , and  $\psi_{q_2}$  are the motor first set and second set of  $dq$  voltages, currents and fluxes respectively. The electrical speed is denoted by  $\omega_r$ , and the stator resistance is symbolized by  $r_s$ . The magnet flux is represented by  $\psi_{pm}$ . The parameters  $L_d$ ,  $L_q$ ,  $L_{md}$ ,  $L_{mq}$  are the direct and quadrature axis winding self and mutual inductances, respectively. Moreover,  $L_d = L_l + L_{md}$  and  $L_q = L_l + L_{mq}$ . It was assumed that the zero components are zero due to symmetrical three-phase quantities.

The developed electromagnetic torque can be expressed as

$$T_e = \frac{3P}{2} \frac{P}{2} [\psi_{pm}(i_{q_1} + i_{q_2}) + (L_d - L_q)(i_{d_1} i_{q_1} + i_{d_1} i_{q_2} + i_{d_2} i_{q_1} + i_{d_2} i_{q_2})]. \quad (6.9)$$

The two following equations describe the mechanical part of the motor

$$\frac{d\omega_r}{dt} = \frac{P}{2J} (T_e - \frac{2B_m}{P} \omega_r - T_L) \quad (6.10)$$

$$\frac{d\theta_r}{dt} = \omega_r \quad (6.11)$$

where  $J$ ,  $B_m$ ,  $T_L$ , and  $P$  are the moment of inertia, viscous friction coefficient, load torque, and motor number of poles, respectively.

If the motor rotates as a generator while the terminals are open with zero currents, the induced voltages in the windings are shifted for the two sets of windings because of the space shift. For example, the voltage in phase A of the first set of the three-phase windings has a  $\pi/6$  phase shift with respect to phase A of the second set of three-phase windings. But using the before-mentioned extended Park transformation or its inverse,  $\mathbf{K}_s$  or  $\mathbf{K}_s^{-1}$ , the  $dq$  voltages are the same. So, the same  $dq$  voltage does not result the same voltage in  $abc$  and the  $\pi/6$  phase shift should be accounted for this case.

The split-phase PM motor flux equations, (6.5)-(6.8), show that both windings' currents are contributing to the stator flux for both  $d$  and  $q$  components. Any attempt for regulating the  $dq$  currents needs some kind of decoupling. If the rotational emf is neglected in the voltage equations, it is possible to decompose the system equations by using its eigenvalues and related eigenvector (similarity transform). In the FOC of a three-phase motor, the rotational emf voltages are eliminated by adding feedforward terms in the controller. At first these terms are ignored in the system equations to be able to decouple  $d$  and  $q$  components by transforming them to a modal form using similarity transformation. A new set of variables are defined as a result of this transformation. The system equations are obtained with the use of the new variables and the control strategy is developed accordingly.

### 6.2.1 System State-Space Model Using Currents as States

The main idea is to have decoupled  $PI$  current controllers, so the system equations are re-written in state-space format while the currents are state variables. The  $dq$  fluxes are calculated as a function of the currents and permanent magnet flux by the following matrix equations as

$$\begin{bmatrix} \psi_{d1} \\ \psi_{d2} \end{bmatrix} = \begin{bmatrix} L_d & L_{md} \\ L_{md} & L_d \end{bmatrix} \begin{bmatrix} i_{d1} \\ i_{d2} \end{bmatrix} + \begin{bmatrix} \psi_{pm} \\ \psi_{pm} \end{bmatrix} \quad (6.12)$$

$$\begin{bmatrix} \psi_{q1} \\ \psi_{q2} \end{bmatrix} = \begin{bmatrix} L_q & L_{mq} \\ L_{mq} & L_q \end{bmatrix} \begin{bmatrix} i_{q1} \\ i_{q2} \end{bmatrix}. \quad (6.13)$$

Now, by inserting the above equations in the voltage equations (6.1)-(6.4), the double  $dq$  model of the split-phase PM motor in state-space form is

$$\begin{aligned} \frac{d}{dt} \begin{bmatrix} i_{d1} \\ i_{d2} \end{bmatrix} &= -r_s \begin{bmatrix} L_d & L_{md} \\ L_{md} & L_d \end{bmatrix}^{-1} \begin{bmatrix} i_{d1} \\ i_{d2} \end{bmatrix} + \begin{bmatrix} L_d & L_{md} \\ L_{md} & L_d \end{bmatrix}^{-1} \begin{bmatrix} v_{d1} \\ v_{d2} \end{bmatrix} \\ &\quad + \omega_r \begin{bmatrix} L_d & L_{md} \\ L_{md} & L_d \end{bmatrix}^{-1} \begin{bmatrix} \psi_{q1} \\ \psi_{q2} \end{bmatrix} \end{aligned} \quad (6.14)$$

$$\begin{aligned} \frac{d}{dt} \begin{bmatrix} i_{q1} \\ i_{q2} \end{bmatrix} &= -r_s \begin{bmatrix} L_q & L_{mq} \\ L_{mq} & L_q \end{bmatrix}^{-1} \begin{bmatrix} i_{q1} \\ i_{q2} \end{bmatrix} + \begin{bmatrix} L_q & L_{mq} \\ L_{mq} & L_q \end{bmatrix}^{-1} \begin{bmatrix} v_{q1} \\ v_{q2} \end{bmatrix} \\ &\quad - \omega_r \begin{bmatrix} L_q & L_{mq} \\ L_{mq} & L_q \end{bmatrix}^{-1} \begin{bmatrix} \psi_{d1} \\ \psi_{d2} \end{bmatrix}. \end{aligned} \quad (6.15)$$

When the inputs,  $dq$  voltages in this case, are zero and the rotational emf is ignored, the system behavior is described by the eigenvalues of the matrices

$A_d$  and  $A_q$  that are defined as

$$A_d = -r_s \begin{bmatrix} L_d & L_{md} \\ L_{md} & L_d \end{bmatrix}^{-1} = \begin{bmatrix} \frac{-r_s L_d}{L_d^2 - L_{md}^2} & \frac{r_s L_{md}}{L_d^2 - L_{md}^2} \\ \frac{r_s L_{md}}{L_d^2 - L_{md}^2} & \frac{-r_s L_d}{L_d^2 - L_{md}^2} \end{bmatrix} \quad (6.16)$$

$$A_q = -r_s \begin{bmatrix} L_q & L_{mq} \\ L_{mq} & L_q \end{bmatrix}^{-1} = \begin{bmatrix} \frac{-r_s L_q}{L_q^2 - L_{mq}^2} & \frac{r_s L_{mq}}{L_q^2 - L_{mq}^2} \\ \frac{r_s L_{mq}}{L_q^2 - L_{mq}^2} & \frac{-r_s L_q}{L_q^2 - L_{mq}^2} \end{bmatrix}. \quad (6.17)$$

The eigenvalues of matrix  $A_d$ ,  $\lambda_{d1}$  and  $\lambda_{d2}$ , are

$$\lambda_{d1} = -\frac{r_s}{L_d - L_{md}} = -\frac{r_s}{L_l} \quad (6.18)$$

$$\lambda_{d2} = -\frac{r_s}{L_d + L_{md}}. \quad (6.19)$$

The eigenvalues of matrix  $A_q$ ,  $\lambda_{q1}$  and  $\lambda_{q2}$ , for the  $q$  components are

$$\lambda_{q1} = -\frac{r_s}{L_q - L_{mq}} = -\frac{r_s}{L_l} \quad (6.20)$$

$$\lambda_{q2} = -\frac{r_s}{L_q + L_{mq}}. \quad (6.21)$$

All eigenvalues are real and negative in this case which means the system is stable as expected since the inputs are zero and rotational emf is ignored. The inverse of eigenvalues are the motor time constants for the  $dq$  components. These time constants are  $\tau_{d1} = -\frac{L_l}{r_s}$ ,  $\tau_{d2} = -\frac{L_d + L_{md}}{r_s}$ ,  $\tau_{q1} = -\frac{L_l}{r_s}$ ,  $\tau_{q2} = -\frac{L_q + L_{mq}}{r_s}$  respectively. Two time constants are describing  $dq$  dynamics and two equal time constants show the impact of motor leakage inductance.

Consequently, eigenvectors are calculated for each eigenvalue as

$$\mathbf{e}_{d1} = \begin{bmatrix} \frac{1}{2} \\ -\frac{1}{2} \end{bmatrix} \quad (6.22)$$

$$\mathbf{e}_{d2} = \begin{bmatrix} \frac{1}{2} \\ \frac{1}{2} \end{bmatrix} \quad (6.23)$$

$$\mathbf{e}_{q1} = \begin{bmatrix} \frac{1}{2} \\ -\frac{1}{2} \end{bmatrix} \quad (6.24)$$

$$\mathbf{e}_{q2} = \begin{bmatrix} \frac{1}{2} \\ \frac{1}{2} \end{bmatrix} \quad (6.25)$$

where  $\mathbf{e}_{d1}$ ,  $\mathbf{e}_{d2}$ ,  $\mathbf{e}_{q1}$ , and  $\mathbf{e}_{q2}$  and are the eigenvectors related to  $\lambda_{d1}$ ,  $\lambda_{d2}$ ,  $\lambda_{q1}$ , and  $\lambda_{q2}$  respectively. The matrices  $\mathbf{X}_d$  and  $\mathbf{X}_q$  are defined as matrices that have above eigenvectors as columns, i. e.

$$\mathbf{X}_d = [ \mathbf{e}_{d1} \quad \mathbf{e}_{d2} ] = \begin{bmatrix} \frac{1}{2} & \frac{1}{2} \\ -\frac{1}{2} & \frac{1}{2} \end{bmatrix} \quad (6.26)$$

$$\mathbf{X}_q = [ \mathbf{e}_{q1} \quad \mathbf{e}_{q2} ] = \begin{bmatrix} \frac{1}{2} & \frac{1}{2} \\ -\frac{1}{2} & \frac{1}{2} \end{bmatrix}. \quad (6.27)$$

Matrices  $\mathbf{X}_d$  and  $\mathbf{X}_q$  are equal in this case and their inverse is  $\mathbf{X}_d^{-1} = \mathbf{X}_q^{-1} = \begin{bmatrix} 1 & -1 \\ 1 & 1 \end{bmatrix}$ . Now by defining the new variables using  $\mathbf{X}_d^{-1}$  and  $\mathbf{X}_q^{-1}$ , the system state-space model is diagonalized (similarity transform). The new variables are defined as:

$$\begin{bmatrix} i_{dn} \\ i_{dp} \end{bmatrix} = \mathbf{X}_d^{-1} \begin{bmatrix} i_{d1} \\ i_{d2} \end{bmatrix} = \begin{bmatrix} i_{d1} - i_{d2} \\ i_{d1} + i_{d2} \end{bmatrix} \quad (6.28)$$

$$\begin{bmatrix} i_{qn} \\ i_{qp} \end{bmatrix} = \mathbf{X}_q^{-1} \begin{bmatrix} i_{q1} \\ i_{q2} \end{bmatrix} = \begin{bmatrix} i_{q1} - i_{q2} \\ i_{q1} + i_{q2} \end{bmatrix}. \quad (6.29)$$

As is shown in the equations, the new currents are summations and negations of the  $d$  and  $q$  currents respectively. To change back from the new variables to the original ones, the following inverse transformations are needed

$$\begin{bmatrix} i_{d1} \\ i_{d2} \end{bmatrix} = \begin{bmatrix} \frac{1}{2} & \frac{1}{2} \\ -\frac{1}{2} & \frac{1}{2} \end{bmatrix} \begin{bmatrix} i_{dn} \\ i_{dp} \end{bmatrix} \quad (6.30)$$

$$\begin{bmatrix} i_{q1} \\ i_{q2} \end{bmatrix} = \begin{bmatrix} \frac{1}{2} & \frac{1}{2} \\ -\frac{1}{2} & \frac{1}{2} \end{bmatrix} \begin{bmatrix} i_{qn} \\ i_{qp} \end{bmatrix}. \quad (6.31)$$

As is shown later on it is more convenient to define new variables for the flux  $dq$  components similar to the transformation that is used for the currents as

$$\begin{bmatrix} \psi_{dn} \\ \psi_{dp} \end{bmatrix} = \mathbf{X}_d^{-1} \begin{bmatrix} \psi_{d1} \\ \psi_{d2} \end{bmatrix} = \begin{bmatrix} \psi_{d1} - \psi_{d2} \\ \psi_{d1} + \psi_{d2} \end{bmatrix} \quad (6.32)$$

$$\begin{bmatrix} \psi_{qn} \\ \psi_{qp} \end{bmatrix} = \mathbf{X}_q^{-1} \begin{bmatrix} \psi_{q1} \\ \psi_{q2} \end{bmatrix} = \begin{bmatrix} \psi_{q1} - \psi_{q2} \\ \psi_{q1} + \psi_{q2} \end{bmatrix}. \quad (6.33)$$

With this variable change, the relation between the fluxes and currents are

$$\begin{bmatrix} \psi_{dn} \\ \psi_{dp} \end{bmatrix} = \begin{bmatrix} L_d - L_{md} & 0 \\ 0 & L_d + L_{md} \end{bmatrix} \begin{bmatrix} i_{dn} \\ i_{dp} \end{bmatrix} + \begin{bmatrix} 0 \\ 2\psi_{pm} \end{bmatrix} \quad (6.34)$$

$$\begin{bmatrix} \psi_{qn} \\ \psi_{qp} \end{bmatrix} = \begin{bmatrix} L_q - L_{mq} & 0 \\ 0 & L_q + L_{mq} \end{bmatrix} \begin{bmatrix} i_{qn} \\ i_{qp} \end{bmatrix}. \quad (6.35)$$

The same transformation can be used for the  $dq$  voltages. Hence, the new voltage variables are defined as

$$\begin{bmatrix} v_{dn} \\ v_{dp} \end{bmatrix} = \mathbf{X}_d^{-1} \begin{bmatrix} v_{d1} \\ v_{d2} \end{bmatrix} = \begin{bmatrix} v_{d1} - v_{d2} \\ v_{d1} + v_{d2} \end{bmatrix} \quad (6.36)$$

$$\begin{bmatrix} v_{qn} \\ v_{qp} \end{bmatrix} = \mathbf{X}_q^{-1} \begin{bmatrix} v_{q1} \\ v_{q2} \end{bmatrix} = \begin{bmatrix} v_{q1} - v_{q2} \\ v_{q1} + v_{q2} \end{bmatrix} \quad (6.37)$$

As a first result, the torque equation in terms of the new variables is

$$T_e = \frac{3P}{2} [\psi_{pm} i_{qp} + (L_d - L_q) i_{dp} i_{qp}]. \quad (6.38)$$

So the positive components of the new  $dq$  currents are contributing in the torque development. The above equation is very similar to the classical torque

equation for a normal three-phase PM motor. The negative components of the currents,  $i_{dn}$  and  $i_{qn}$ , that are related to the motor leakage inductance are not influencing the torque equation.

Now the new variables are replaced on the original system equations to have a decoupled state-space model for the electrical dynamics as is described in the following

$$\frac{d}{dt} \begin{bmatrix} i_{dn} \\ i_{dp} \end{bmatrix} = \begin{bmatrix} \frac{-r_s}{L_d - L_{md}} & 0 \\ 0 & \frac{-r_s}{L_d + L_{md}} \end{bmatrix} \begin{bmatrix} i_{dn} \\ i_{dp} \end{bmatrix} + \begin{bmatrix} \frac{1}{L_d - L_{md}} & 0 \\ 0 & \frac{1}{L_d + L_{md}} \end{bmatrix} \begin{bmatrix} v_{dn} \\ v_{dp} \end{bmatrix} + \omega_r \begin{bmatrix} \frac{1}{L_d - L_{md}} & 0 \\ 0 & \frac{1}{L_d + L_{md}} \end{bmatrix} \begin{bmatrix} \psi_{qn} \\ \psi_{qp} \end{bmatrix} \quad (6.39)$$

$$\frac{d}{dt} \begin{bmatrix} i_{qn} \\ i_{qp} \end{bmatrix} = \begin{bmatrix} \frac{-r_s}{L_q - L_{mq}} & 0 \\ 0 & \frac{-r_s}{L_q + L_{mq}} \end{bmatrix} \begin{bmatrix} i_{qn} \\ i_{qp} \end{bmatrix} + \begin{bmatrix} \frac{1}{L_q - L_{mq}} & 0 \\ 0 & \frac{1}{L_q + L_{mq}} \end{bmatrix} \begin{bmatrix} v_{qn} \\ v_{qp} \end{bmatrix} - \omega_r \begin{bmatrix} \frac{1}{L_q - L_{mq}} & 0 \\ 0 & \frac{1}{L_q + L_{mq}} \end{bmatrix} \begin{bmatrix} \psi_{dn} \\ \psi_{dp} \end{bmatrix}. \quad (6.40)$$

As is shown in the equations, the system is diagonalized and the diagonal elements are the previously calculated eigenvalues. To design the current controller it is more convenient to write the new state-space equations of the system in the following form as

$$v_{dp} = r_s i_{dp} + (L_d + L_{md}) \frac{d}{dt} i_{dp} - \omega_r \psi_{qp} \quad (6.41)$$

$$v_{qp} = r_s i_{qp} + (L_q + L_{mq}) \frac{d}{dt} i_{qp} + \omega_r \psi_{dp} \quad (6.42)$$

$$v_{dn} = r_s i_{dn} + L_l \frac{d}{dt} i_{dn} - \omega_r \psi_{qn} \quad (6.43)$$

$$v_{qn} = r_s i_{qn} + L_l \frac{d}{dt} i_{qn} + \omega_r \psi_{dn}. \quad (6.44)$$

Now it is possible to compensate the rotational emf terms that are multiplied by  $\omega_r$  by adding a feedforward term in the controller.

### 6.3 FOC of the Drive System Using Decomposed Variables

A simple diagram of the drive system based on the decoupled variables is shown in Fig. 6.2. The reference speed is compared with the measured or estimated speed to provide the speed error signal. A *PI* controller processes the speed error. The output is a proper torque reference signal to achieve the desired speed dynamical performance. The torque development is made by indirect current control of the machine in the direction of the *d* and *q* axes. For the split-phase PM motor, a MTPA strategy is utilized to obtain the reference values for the current controllers. The developed MTPA for this motor is explained in this section. However, the anti wind up circuits and limiters are not shown for the simplicity. In a normal FOC, the *dq* components of the currents are

directly controlled where a decoupling network is utilized [58]. In the proposed scheme, the new defined currents are controlled and the decoupling network is eliminated. The feedforward part is still there but with the new defined variables.

The reference values for current  $dq$  components are calculated according to the MTPA strategy. The values are calculated off-line and are stored in a look up table. The two set of windings have identical  $dq$  reference values because of the symmetry. The reference values are input to the four independent current regulators. Two phase currents out of three are measured for each set of three-phase windings to calculate the  $dq$  components of the currents respectively. Then they are transformed to the new currents,  $i_{dp}$ ,  $i_{dn}$ ,  $i_{qp}$ , and  $i_{qn}$ . Four independent  $PI$  controllers provide the reference voltage values for the inverters in terms of transformed variables. The inverse transformation is applied to calculate the voltages in  $dq$ . Using the rotor angle, these  $dq$  values are transformed into  $\alpha\beta$  stationary reference frame values. Here, it is assumed that the position signal is available by a sensor like a resolver or an encoder.

In the case of a failure in one set of three-phase windings or in one inverter, the second one can continue to operate, but an adjustment of the torque reference value is needed since the motor can no longer provide the rated torque.

### 6.3.1 MTPA Strategy for the Split-Phase PM Motor

MTPA for a drive system based on the classical three-phase PM motor is a well-known method [109–111]. For the split-phase PM motor the optimal trajectories are extracted using the same approach as one does for a classical drive system. For the drive system, the reference values of the current  $dq$  components are the same for the two sets of windings due to symmetry. The current controllers, ideally, can generate the reference currents, so the system equations can be simplified with this assumption. Assume that the optimal currents of the two set of windings are equal, that is

$$i_d = i_{d_1} = i_{d_2} \quad (6.45)$$

$$i_q = i_{q_1} = i_{q_2}. \quad (6.46)$$

By replacing the above equations in the split-phase PM motor torque equation, (6.9), the torque is simplified to

$$T_e = 3\frac{P}{2}[\psi_{pm}i_q + 2(L_d - L_q)i_d i_q]. \quad (6.47)$$

The developed torque with respect to the stator current magnitude is maximized by using MTPA. A variable change is made for this calculation according to Fig. 6.3 that shows the motor vector diagram in steady-state as follows:

$$i_d = -I_s \sin\beta \quad (6.48)$$

$$i_q = I_s \cos\beta \quad (6.49)$$

where  $I_s = \sqrt{i_d^2 + i_q^2}$  is the magnitude of the stator current, and  $\beta$  is the stator current vector angle with respect to the  $q$  axis. So, the torque equation is a

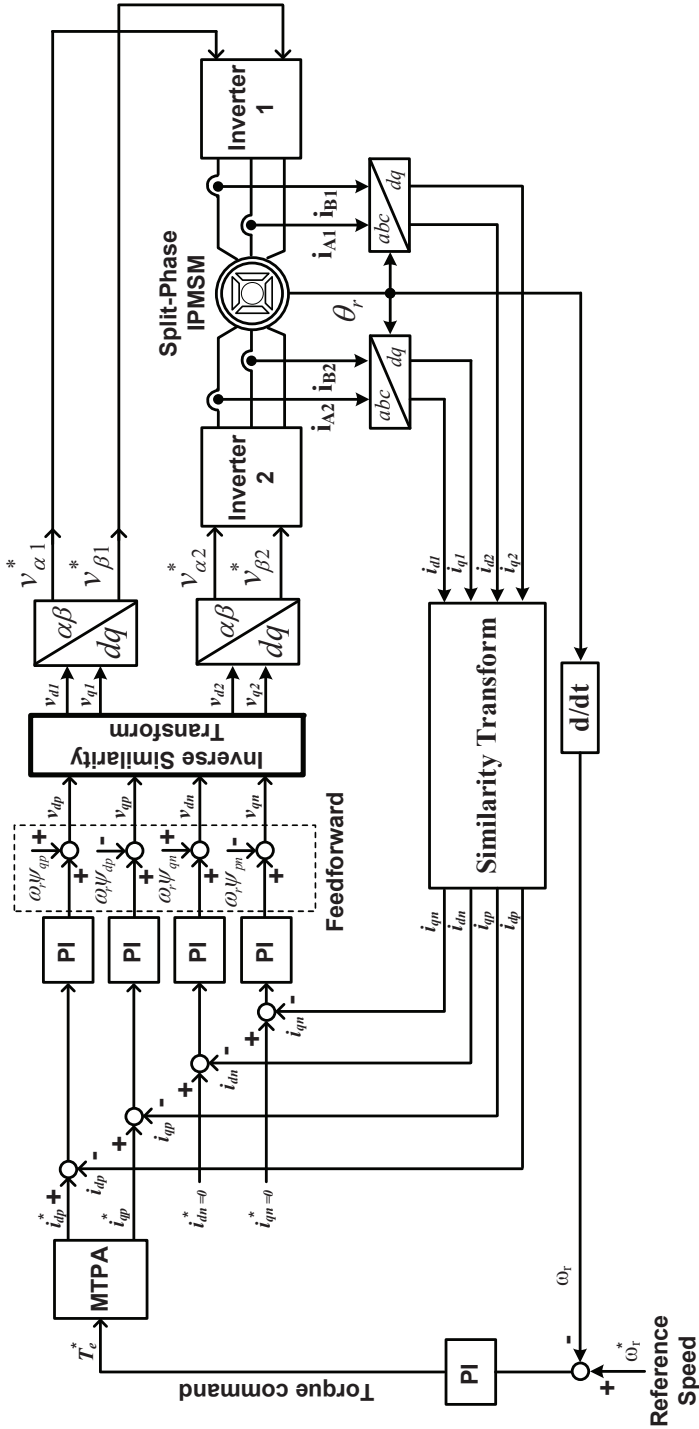


Figure 6.2: Proposed modal FOC for the split-phase PM motor with dual inverters based on the MTPA.

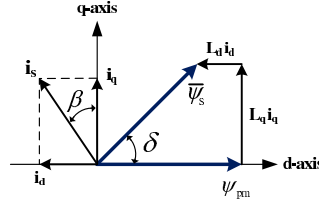


Figure 6.3: Vector diagram of the motor in steady state and with identical  $dq$  currents for each set of windings.

function of  $I_s$  and  $\beta$  as

$$\begin{aligned} T_e(I_s, \beta) &= 3\frac{P}{2}[\psi_{pm}I_s \cos\beta - 2(L_d - L_q)I_s^2 \sin\beta \cos\beta] \\ &= 3\frac{P}{2}[\psi_{pm}I_s \cos\beta - (L_d - L_q)I_s^2 \sin 2\beta]. \end{aligned} \quad (6.50)$$

For a constant  $I_s$ , the torque can be maximized by setting the derivative of equation (6.50) to zero with respect to  $\beta$  as

$$\frac{\partial T_e(I_s, \beta)}{\partial \beta} = 3\frac{P}{2}[\psi_{pm}(-I_s \sin\beta) - 2(L_d - L_q)I_s^2 \cos 2\beta] = 0. \quad (6.51)$$

The above equation can be simplified to the following condition:

$$\psi_{pm} \sin\beta + 2(L_d - L_q)I_s \cos 2\beta = 0. \quad (6.52)$$

Using the trigonometrical identity  $\cos 2\beta = 1 - 2\sin^2\beta$ , (6.52) is written as a second order equation with respect to  $\sin\beta$ :

$$4(L_d - L_q)I_s \sin^2\beta - \psi_{pm} \sin\beta - 2(L_d - L_q)I_s = 0. \quad (6.53)$$

For the split-phase PM motor, the value of  $(L_d - L_q)$  is negative and the optimal  $i_d$  is negative too. So, the solution of (6.53) is calculated as

$$\sin\beta = \frac{\psi_{pm} - \sqrt{\psi_{pm}^2 + 32(L_d - L_q)^2 I_s^2}}{8(L_d - L_q)I_s}. \quad (6.54)$$

As a result, the calculated value of  $i_d$  is

$$i_d = -I_s \sin\beta = \frac{-\psi_{pm} + \sqrt{\psi_{pm}^2 + 32(L_d - L_q)^2 I_s^2}}{8(L_d - L_q)}. \quad (6.55)$$

Now,  $i_q$  can be calculated as

$$i_q = \pm \sqrt{I_s^2 - i_d^2} \quad (6.56)$$

where the positive and negative signs are for the positive and negative torque values respectively.

Now one can replace calculated optimal values of  $i_d$  and  $i_q$  into the torque equation (6.47) to calculate the maximum torque as a function of  $I_s$ :

$$T_e = 3 \frac{P}{2} \left[ \psi_{pm} + 2(L_d - L_q) \frac{-\psi_{pm} + \sqrt{\psi_{pm}^2 + 32(L_d - L_q)^2 I_s^2}}{8(L_d - L_q)} \right] \sqrt{I_s^2 - \left( \frac{-\psi_{pm} + \sqrt{\psi_{pm}^2 + 32(L_d - L_q)^2 I_s^2}}{8(L_d - L_q)} \right)^2}. \quad (6.57)$$

So for a given current, the maximum torque according to MTPA is calculated according to the equation above. The reference values of  $i_d$  and  $i_q$  are transformed to the related  $i_{dp}$  and  $i_{qp}$  according to before mentioned similarity transform that is  $i_{dp} = 2i_d$  and  $i_{qp} = 2i_q$ . The optimal trajectory that is a function of required torque is calculated offline and saved in a look up table.

### 6.3.2 Design of Current PI Controllers

The current controllers have a vital impact on the drive systems performance making their design an important task in the system design. Usually the electrical dynamics are faster than the mechanical dynamics, so it is reasonable to assume that the electrical time constants are ten times faster than the mechanical time constants. Hence it is assumed that during the switching period the speed is constant. The developed electromagnetic torque is a function of currents, that means the quality of the produced torque and consequently the speed depends on how the currents are controlled in the system. From the reliability point of view, the power electronic switches are very sensitive to overcurrent situations. Thus it is very important to have an accurate control on the current during the transients to be in the safe side during the operation.

The motor electrical dynamical equations are explained by (6.41)-(6.44) in terms of new variables. As is shown in Fig. 6.2, the rotational emf terms are canceled out by the feedforward operation. Hence, the transfer function for each current component is a first order equation while it is fully decoupled from the other current components. Consequently, the transfer functions can be defined as

$$G_{dp}(s) = \frac{i_{dp}(s)}{v_{dp}(s)} = \frac{1}{(L_d + L_{md})s + r_s} \quad (6.58)$$

$$G_{qp}(s) = \frac{i_{qp}(s)}{v_{qp}(s)} = \frac{1}{(L_q + L_{mq})s + r_s} \quad (6.59)$$

$$G_{dn}(s) = G_{qn}(s) = \frac{i_{dn}(s)}{v_{dn}(s)} = \frac{i_{qn}(s)}{v_{qn}(s)} = \frac{1}{L_l s + r_s}. \quad (6.60)$$

There are four poles that two of them are identical. These double poles are related to the motor leakage inductance which are the fastest time constants in the system. Two other poles are related to the  $d$  and  $q$  axes respectively. So the design of the  $PI$  controllers is simplified to the design of four independent  $PI$  controllers for first order systems. Different approaches can be used to design the controllers. A convenient method is loop shaping that is a special case of the internal mode control (IMC) method [112].

The design procedure is explained for a first order system in the form of  $G_e(s) = \frac{i(s)}{v(s)} = \frac{1}{Ls+R}$  where the results are directly applied for the above transfer functions [112]. Assume that the *PI* controller transfer function is  $F_e(s) = K_p + K_i/s$  where  $K_p$  and  $K_i$  are the proportional and integral gains. It is desired to have a closed loop control system that enables following a reference current  $i^*$ . The transfer function describing the motor current and reference current is  $G_{cl}(s) = i(s)/i^*(s) = \frac{F_e(s)G_e(s)}{1+F_e(s)G_e(s)}$ . In the loop shaping method [112], the *PI* gains are selected to have the closed-loop transfer function as  $G_{cl}(s) = \frac{\alpha_e}{s+\alpha_e}$  where  $\alpha_e$  is the closed-loop system bandwidth. For a first order system, the closed-loop system bandwidth and rise time,  $t_r$ , are related to each other by  $t_r = \ln 9/\alpha_e$  [112]. By choosing  $K_p = \alpha_e L$  and  $K_i = \alpha_e R$ , the closed-loop transfer function will have the desired transfer function. So, at first step the controller bandwidth,  $\alpha_e$ , is selected and then the gains  $K_p$  and  $K_i$  are selected according to the above equations.

Basically by designing the controller in this way, the system original poles are canceled and they are replaced by desired poles. The controller bandwidth can not be selected to be high because of the limitation in the system sampling time. As a rule of thumb, the controller bandwidth can be selected 5-10 times slower than the system sampling time. If the system sampling time is  $T_s$ , the controller bandwidth can be written as  $\alpha_e = \frac{1}{5} \frac{2\pi}{T_s}$  where the bandwidth is 5 times slower than the sampling time in this case.

## 6.4 Simulation Results for the Drive System

A 4 pole split-phase PM machine is designed and constructed for a 20 kW traction system that is used in the simulations. The motor parameters are shown in Table 6.1. The whole system has been simulated by the use of the Matlab/Simulink software based on the above-mentioned system equations. An ideal converter has been used in the simulation (no PWM or SVM is used for the inverter). However, the converter voltages are limited by the maximum rated values in the simulations. For the simulation, the optimal values of  $i_{dp}$  and  $i_{qp}$  are stored in a look up table as a function of the input requested torque by the speed control loop.

To evaluate the drive system, a speed profile is commanded to the system under a variable torque load. The load is proportional to the speed and is close to the rated torque at the rated speed. Fig. 6.4 shows the reference speed and the motor speed. The reference value of speed is increased linearly from zero to  $2\pi 10 \text{ rad/s}$  during 1s and it is constant for another second until  $t = 2 \text{ s}$ . At  $t = 2 \text{ s}$  a step change is commanded to  $2\pi 50 \text{ rad/s}$  to evaluate the step response of the drive system. Then the speed reference is constant another second until  $t = 3 \text{ s}$ . At  $t = 3 \text{ s}$ , the speed is reduced to  $-2\pi 50 \text{ rad/s}$  during 2 s until  $t = 5 \text{ s}$  and then remains constant. As can be seen in the Fig., the speed has a good dynamic response. The developed electromagnetic torque by the motor is shown in Fig. 6.5.

The MTPA part of the controller provides the reference values for the *dq* current components. These reference values are shown in Fig. 6.6. The *d* component of the current is always negative, but the *q* component can be positive or negative for the positive or negative torque demand respectively.

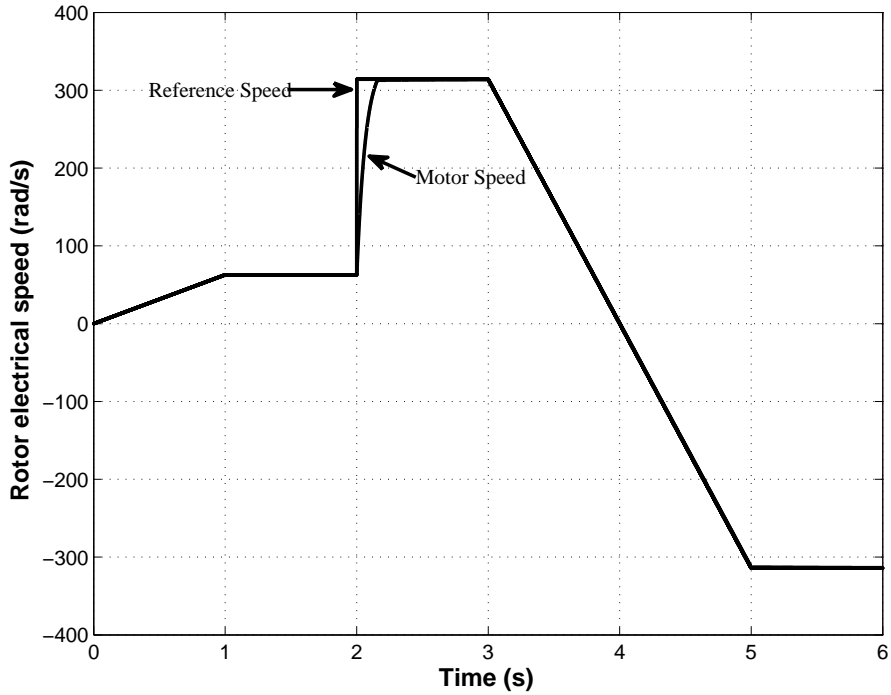


Figure 6.4: Simulation result: electrical reference speed and motor speed in traction.

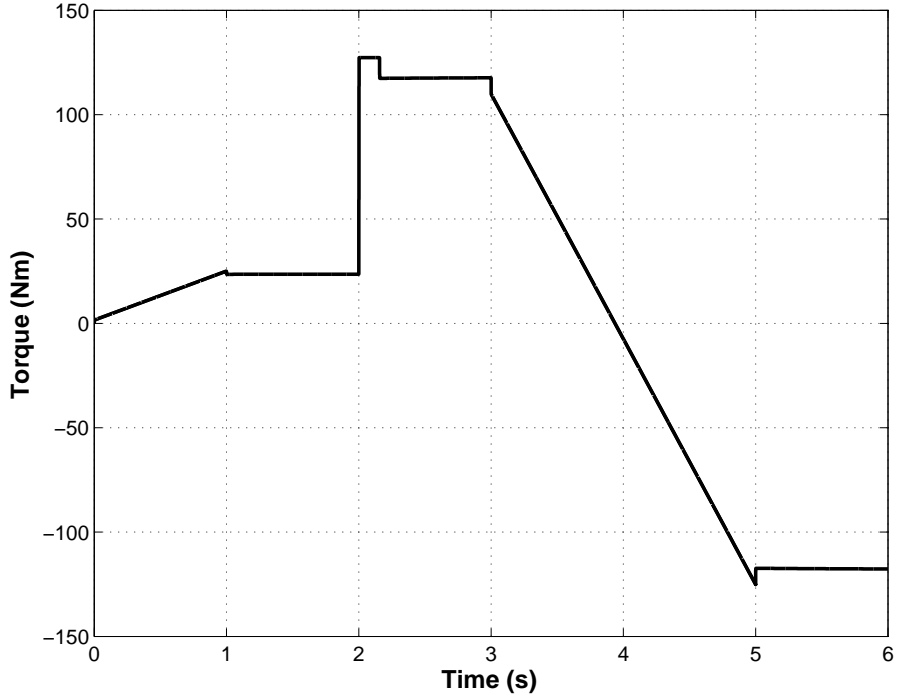


Figure 6.5: Simulation result: motor developed electromagnetic torque.

Table 6.1: Split-phase PM motor parameters

Rated power ( $kW$ )	20
Rated speed( $r/min$ )	1500
$P$ , No of poles	4
$\psi_{pm}$ , Permanent magnet flux ( $Wb$ )	1
$r_s$ , Stator resistance ( $Ohm$ )	0.96
$L_d$ , d-axis inductance ( $mH$ )	12
$L_q$ , q-axis inductance ( $mH$ )	33.7
$L_l$ , Leakage inductance ( $mH$ )	1.5
$J$ , Inertia ( $kg.m^2$ )	0.05
$B$ , Viscous friction coefficient ( $Nm.s/rad$ )	0.05

The three-phase current for the first set of the windings is shown in Fig. 6.7 for different time intervals.

As mentioned before, the motor windings are shifted  $\pi/6$  degree in the stator periphery. The current waveforms for the phase A of the first set of windings and the second set of windings are shown in Fig. 6.8 to show the phase shift in the currents also.

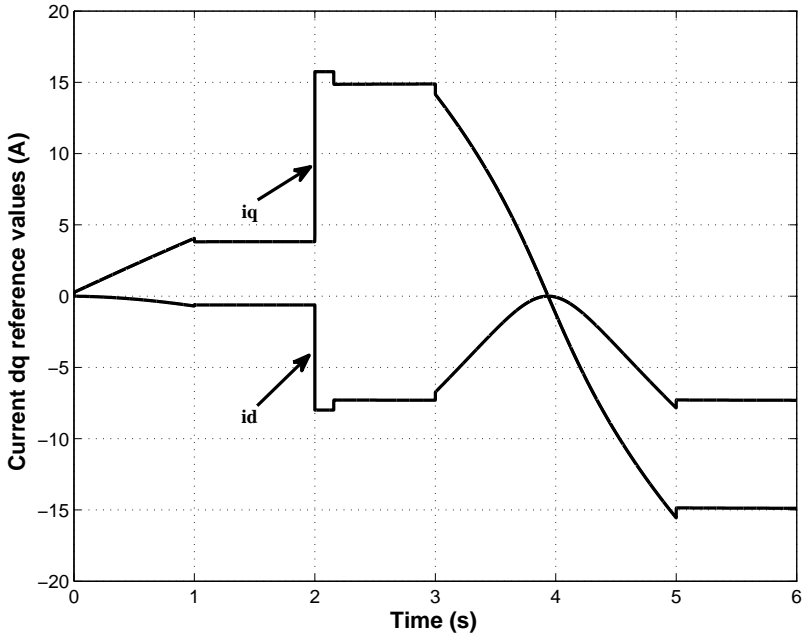


Figure 6.6: Simulation result: reference values of dq currents based on the MTPA strategy.

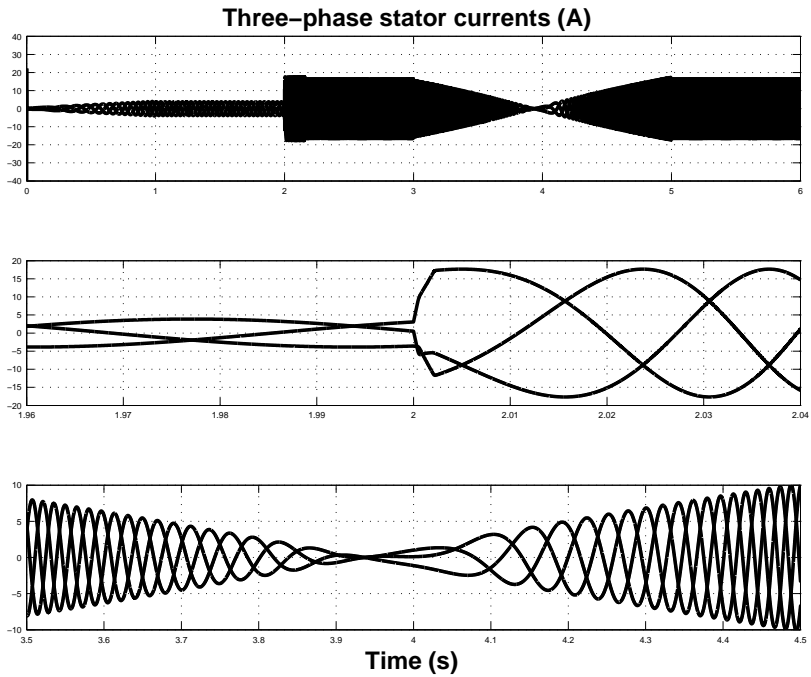


Figure 6.7: Simulation result: three-phase currents in one set of the three-phase windings.

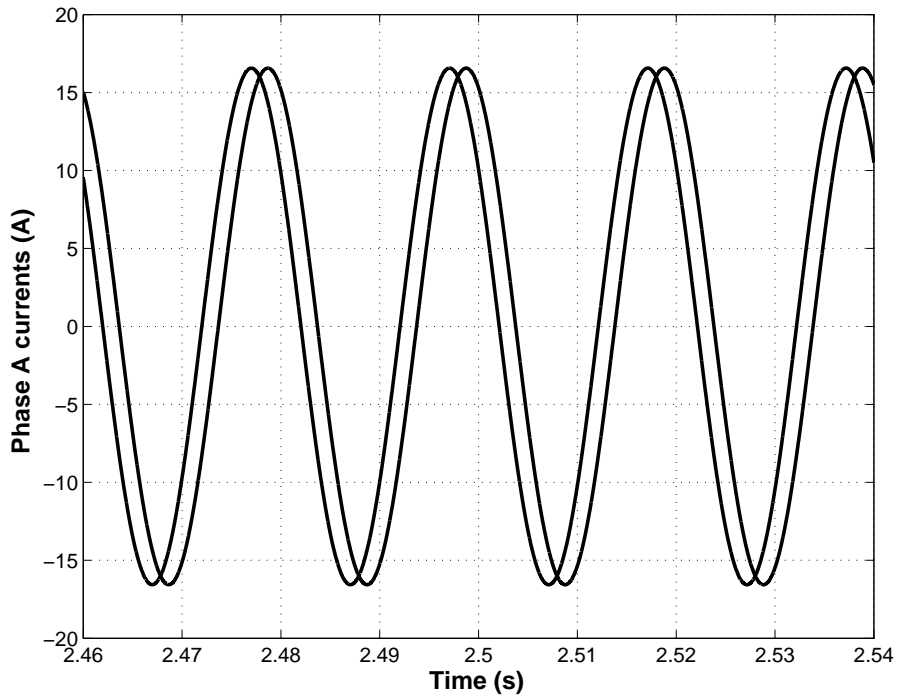


Figure 6.8: Simulation result: phase A currents for the first and the second set of windings.



# Chapter 7

## Conclusions and Future Work

### 7.1 Conclusions

Different examples of integrated motor drive and battery chargers introduced by academia or industry have been reviewed and compared. Circuit configuration, traction/charging functionality, charging features like bidirectional capability or unity power factor operation capability, control strategy for the traction and charging and the degree of integration are the main aspects of this review and comparison. Table 2.1 shows a summary of these solutions including the comparison results.

A novel integrated motor drive and isolated battery charger based on a split-phase PM motor is presented in this thesis. The charger is a high-power high-efficiency device which uses an extra clutch and a relay-based switching device to reconfigure the traction circuit from the traction mode to the charging mode. The motor is rotating during the charging operation which implies that the system efficiency in the charging mode is lower than the efficiency in the traction mode. On the other hand, a separate battery charger with a high power is eliminated from the system. The control strategy is developed for the battery charging mode for the grid synchronization and battery charging. The motor first synchronizes itself to the grid and then starts to charge the battery. The control algorithm, system functionality, simulation results, and experimental results are provided to verify the proper operation of the system. Two experimental setups have been designed and implemented to verify the proposed scheme. The first system is based on a 20 kW PM motor with a charging power of 3 kW and an efficiency close to 80% is measured. The optimal current trajectory for the motor during the charge operation and the loss analysis is performed and presented for this case. The second system is based on a split-phase PMSM motor with two identical windings that are not shifted in the space. The practical results for the second system show that the integrated charging is feasible in this scheme as well.

The galvanic isolation is the main advantage of the proposed integrated charger in this thesis compared to other types of integrated chargers. How-

ever, because of using an extra clutch, extra switching relays, and lower efficiency compared to other types of integrated chargers, more investigations are needed respect to the total cost of the system. It seems that this solution is an attractive option in higher power levels, in bus or truck applications for instance.

Non-isolated integrated chargers are the mostly used solutions in industrial applications so far. The motor is mainly used as inductances in the charging circuit. It is explained that developed torque in the motor should be zero to be able to use the motor in the charger circuit. Moreover, two main categories of non-isolated integrated motor drive and battery chargers are presented and explained in this thesis. The first solution uses the motor windings midpoints to cancel out the motor mutual flux to be able to use the leakage inductances in the battery charger. The second solution is presented for a split-phase PM motor with dual inverters. For the first solution, it is possible to charge the battery with a single-phase supply and/or a three-phase supply, however a single switch is needed to reconfigure the system for the traction and charging mode operation. The second solution just uses a single-phase power source for the battery charging, but there is no need for any extra component.

The proposed non-isolated integrated chargers in this thesis have a good potential to be utilized as a product because of the low price, simple structure and easy control. However, there is a switching device for the winding re-configuration that may be a limit for the practical implementation. In many applications, like vehicle battery charging, there is a tendency to use the electronic switches instead of relays. The lower price of the charger compared to the other alternatives is a considerable incentive to investigate the proposed concepts in more detail.

In most of proposed integrated chargers, the motor windings are re-figured by a switching device like a contactor, that is an electromechanical component. It is an advantage to have semiconductor electronic switches instead of the contactors because of reliability. Relays have shorter life time compared to the power electronic switches. At the other side, the relays have a lower price compared with the electronic switches.

A double  $dq$  model is developed for the split-phase PM motor using an extended Park transformation. Consequently, the modeling and control of split-phase PM motors that are a type of multi-phase motors are investigated in this context. As an example, a modal FOC-based drive system is presented for the split-phase PM motor. There is a tight coupling between the stator windings that needs a suitable decoupling scheme in the drive system. An eigenvalue decomposition method is utilized to decouple the system to its modal form. Based on the developed decomposed model, a decoupled controller is presented in the stationary  $dq$  reference frame. An MTPA strategy is developed for the split-phase PM motor to complete the whole drive system. Simulation results show that the system has a good dynamic and steady state performance in terms of speed response.

The rotor position is measured by a resolver in the experimental system. Due to high value of noises it is not possible to estimate the speed by direct differentiation of the position. A simple open loop velocity estimator is proposed that is called a trigonometric estimator. Simulation and experimental results are provided to verify that the estimator has a good dynamic and steady state

performance. Moreover, the method is used in the synchronization stage of the proposed isolated integrated charger where a good performance is measured. However, the method is a general scheme that can be used in other drive applications too.

## 7.2 Future Work

### 7.2.1 Future Work Suggestions for Integrated Motor Drive and Isolated Battery Chargers

The PM motors are started to be replaced by other types of machines because of increasing rare-earth magnet price. Consequently, different motor alternatives are considered in many applications like electric traction. The synchronous reluctance motor (SynRM) is an interesting alternative in traction applications, because a classical inverter can be utilized to drive the motor. At this thesis, a PM motor is investigated in the context of integrated motor drive and isolated battery charger. The same study can be performed for a system with a SynRM instead of a PM motor, for instance. In this case more detailed suggestions are presented at the following.

- Motor modeling: a double  $dq$  modeling approach is utilized to model the split-phase PM motor. It is possible to use the same modeling approach for a split-phase SynRM, but magnet induced flux linkage is zero. Moreover, the d and q axis directions are usually different for a PM motor and a SynRM which needs some considerations.
- Stability analysis: the maximum charge power is limited by the motor parameters and thermal limit. More theoretical work is suggested to calculate the maximum charging power while the motor is rotating at synchronous speed to avoid rotor oscillation.
- FEM simulation: for the isolated integrated charger FEM analysis is not performed in this work, and it is recommended to have in future works.
- Efficiency analysis: the motor core loss is assumed to be a constant value because of a constant speed operation during the battery charging. A more accurate model can be used in the efficiency analysis of the system.
- Improvement of control: the introduced controllers for the system in charging mode, for the both grid synchronization and charge control, can be used for a SynRM with slight modifications. However, there is a room for the improvement of grid synchronization and charge control parts. In the grid synchronization, a more reliable synchronization scheme is suggested. The proposed scheme can be improved to have a faster response. In the charge control, the  $dq$  currents are controlled that another  $PI$  loop is needed to control the power directly.
- Harmonic analysis: the motor windings space harmonics reduce the maximum battery charging power because of undesirable torque generation. This extra torque component makes the motor instable during the high power battery charging and a stability analysis is recommended in this

regard. Moreover, it is suggested to evaluate the impact of the harmonics, both time and space, in the maximum charging power level for the proposed isolated battery charger.

As mentioned before, the main challenge for the proposed isolated integrated charger is the system efficiency. If the motor in its classical shape is used as a transformer, there is an airgap in the magnetization path leading to a reduced efficiency. If the motor is used as a rotating transformer or motor/generator, the loss due to the rotation decreases the efficiency. One suggestion is to add extra windings in the stator to have an isolating transformer. The motor windings are not used in this scheme and the extra windings constitute primary and secondary of this grid-frequency step down or up transformer. However, this is a single-phase transformer and it is not possible to use it with a three-phase source. Moreover, it is possible to use the inverter or use another inverter to charge the battery. More investigations are needed to reach an operational solution. Fig. 7.1 shows a simple diagram of the placement of the motor windings and an equivalent circuit of the motor. The motor main windings are  $A$ ,  $B$ , and  $C$ , and the extra windings are  $W_1$ ,  $W_2$ , and  $W_3$ . During the charge time, the main windings are open and the extra windings operate as a step down transformer. There is no flux in the airgap or the flux level is negligible, so there is no electromagnetic torque during the operation of extra windings. The converter is not shown in this figure that can be the traction converter or a new one. During the traction mode, the extra windings are not used, so there is a possibility to use them for other purposes like as the position sensor. However, this solution needs more investigations to make it feasible.

The proposed isolated integrated charger based on a split-phase PM motor can be improved further in different aspects. A more optimized design is needed for the electric machine to have a higher efficiency in the charging mode. In the current design, the motor is optimized for traction mode, but it is recommended to optimize for the charging mode. By improving the system efficiency in charging mode, the system efficiency in traction mode increases. For example, laminations with lower loss can be utilized in the motor to reduce the iron loss, so the iron loss will be lower in traction mode as well.

The control for the grid synchronization and battery charging can be modified to be faster and more robust. Moreover, instead of shifted windings in the stator, non-shifted windings can be considered as an option since the relay switching device will be simpler.

## 7.2.2 Future Work Suggestions for Integrated Motor Drive and Non-Isolated Battery Chargers

Non-isolated chargers are investigated and some new schemes are proposed in this thesis. As mentioned earlier, the PM motor is used in this work that instead a SynRM can be used. So, the proposed non-isolated chargers can be investigated for the system based on a SynRM.

In this work, it is supposed that there is no a DC/DC converter between the inverter and the battery in the system. So the charger needs to operate for a wide range of output dc voltage with respect to different status of the battery

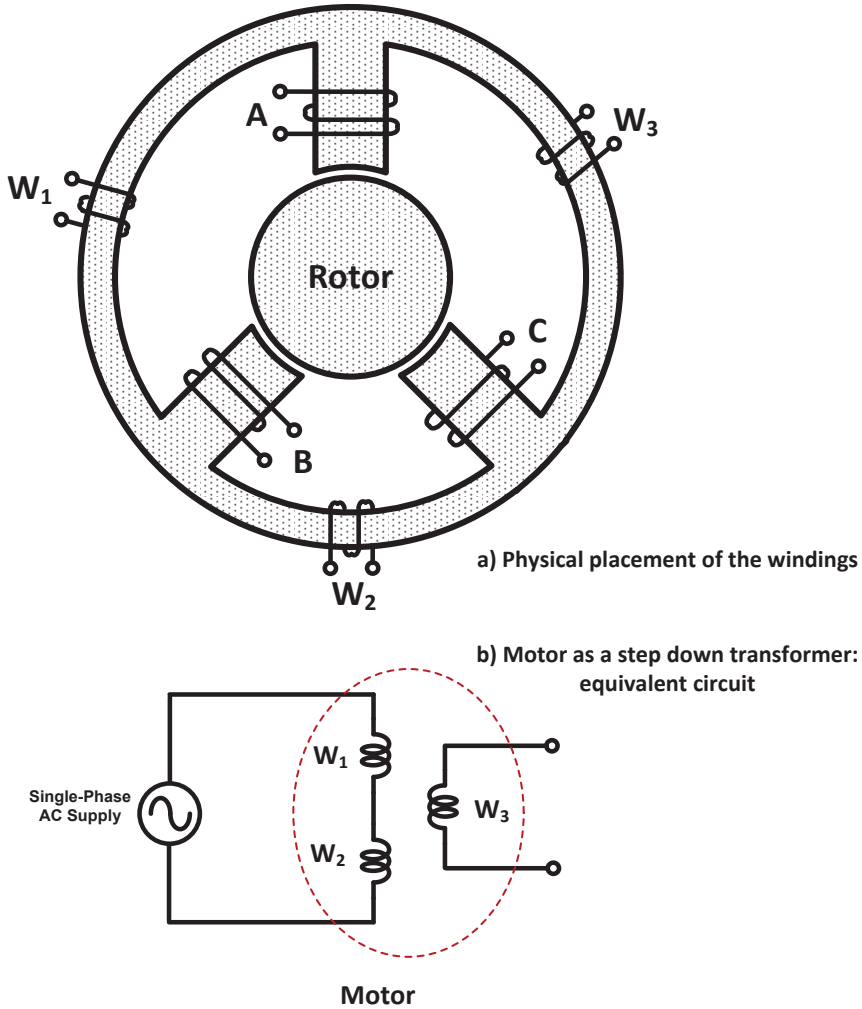


Figure 7.1: Motor configuration as a step down grid-frequency single-phase transformer: a) winding placement b) equivalent circuit.

state of charge. The modulation type of the converter can be investigated to reduce the battery current ripple during the charge operation.

The current waveform quality at the grid side is usually subject of stringent standards. The THD of the current is needed to be less than a certain value. The charger inductors that are the motor leakage inductances should be high enough to filter higher order current harmonics. If the motor leakage inductors have low values, it is possible to compensate the THD by increasing the switching frequency. So, an overall system level design is needed that is not considered in this thesis.

The motors are usually made of laminations like silicon steel laminations. These materials are not suitable for high frequency operation because of high value of core losses. However, the fundamental frequency of the current is the grid frequency that is not considered as high frequency. Using a high-frequency modulation technique like PWM degrades the system performance. However, for the high performance operation this impact needs to be considered in the charger circuit. For example during the motor design stage, a better material can be selected to help the charging efficiency as well.

For the non-isolated integrated charger, there is an inherent safety issue due to the standard regulations. It is highly desirable to have a low value of the earth current according to the standard requirement. Motor installations, windings method and power electronics need special attention to have a reliable charging operation. It will be disturbing to have earth fault error that forces the charger to an off state. More investigations regarding the whole system installation, safety and EMC are proposed in this context.

Some systems use a DC/DC converter between the inverter and the battery. So, there will be more options for the motor drive system and battery charger integration. It is suggested to include a DC/DC converter in the integrated charger circuit to investigate the impact of the DC/DC converter on the solutions that are presented in this work.

# Bibliography

- [1] J. Cao and A. Emadi, “Batteries need electronics,” *Industrial Electronics Magazine, IEEE*, vol. 5, no. 1, pp. 27–35, march 2011.
- [2] M. Yilmaz and P. T. Krein, “Review of charging power levels and infrastructure for plug-in electric and hybrid vehicles,” in *Electric Vehicle Conference (IEVC), 2012 IEEE International*, march 2012, pp. 1–8.
- [3] P. Krein, “Electrostatic discharge issues in electric vehicles,” *Industry Applications, IEEE Transactions on*, vol. 32, no. 6, pp. 1278–1284, 1996.
- [4] *Electric vehicle conductive charging system - Part1: General requirements*, IEC 61851-1 Standard, First edition, 2001.
- [5] *Electric vehicle conductive charging system - Part21: Electric vehicle requirements for conductive connection to an a.c./d.c. supply*, IEC 61851-21 Standard, First edition, 2001.
- [6] S. Haghbin, S. Lundmark, M. Alakula, and O. Carlson, “Grid-connected integrated battery chargers in vehicle applications: Review and new solution,” *Industrial Electronics, IEEE Transactions on*, vol. 60, no. 2, pp. 459–473, feb. 2013.
- [7] S. Haghbin, K. Khan, S. Lundmark, M. Alakula, O. Carlson, M. Leksell, and O. Wallmark, “Integrated chargers for ev’s and phev’s: examples and new solutions,” in *Electrical Machines (ICEM), 2010 XIX International Conference on*, sept. 2010, pp. 1–6.
- [8] S. Haghbin, M. Alakula, K. Khan, S. Lundmark, M. Leksell, O. Wallmark, and O. Carlson, “An integrated charger for plug-in hybrid electric vehicles based on a special interior permanent magnet motor,” in *Vehicle Power and Propulsion Conference (VPPC) Proceedings, in Lille, France*, 2010.
- [9] S. Haghbin, S. Lundmark, M. Alakula, and O. Carlson, “An isolated high-power integrated charger in electrified-vehicle applications,” *Vehicle Technology, IEEE Transactions on*, vol. 60, no. 9, pp. 4115–4126, nov. 2011.
- [10] S. Haghbin and M. Alakula, “Elektrisk apparat innefattande drivsystem och elektrisk maskin med omkopplingsbar statorlindning,” *Swedish Patent Office, Patent no 1050607-9*, Grant date: 14-02-2012.

- [11] M. Alakula and S. Haghbin, "Electrical apparatus comprising drive system and electrical machine with reconnectable stator winding," *International Patent WO/2011/159241*, Publication date 22 December 2011.
- [12] M. Rawson and S. Kateley, "Electric vehicle charging equipment design and health and safety codes," *California Energy Commission Report*, 1998.
- [13] C.-S. Wang, O. Stielau, and G. Covic, "Design considerations for a contactless electric vehicle battery charger," *Industrial Electronics, IEEE Transactions on*, vol. 52, no. 5, pp. 1308 – 1314, 2005.
- [14] H. Sakamoto, K. Harada, S. Washimiya, K. Takehara, Y. Matsuo, and F. Nakao, "Large air-gap coupler for inductive charger [for electric vehicles]," *Magnetics, IEEE Transactions on*, vol. 35, no. 5, pp. 3526 – 3528, Sep. 1999.
- [15] B. Singh, B. Singh, A. Chandra, K. Al-Haddad, A. Pandey, and D. Kothari, "A review of three-phase improved power quality ac-dc converters," *Industrial Electronics, IEEE Transactions on*, vol. 51, no. 3, pp. 641 – 660, 2004.
- [16] —, "A review of single-phase improved power quality ac-dc converters," *Industrial Electronics, IEEE Transactions on*, vol. 50, no. 5, pp. 962 – 981, 2003.
- [17] E. Ismail and R. Erickson, "A new class of low-cost three-phase high-quality rectifiers with zero-voltage switching," *Power Electronics, IEEE Transactions on*, vol. 12, no. 4, pp. 734 – 742, Jul. 1997.
- [18] J. Mandiola, D. Carmona, S. Haghbin, T. Abdulahovic, and M. Ellsen, "An fpga implementation of a voltage-oriented controlled three-phase pwm boost rectifier," in *Electrical Systems for Aircraft, Railway and Ship Propulsion (ESARS), 2012*, oct. 2012, pp. 1 – 6.
- [19] V. Vlatkovic, D. Borojevic, X. Zhuang, and F. Lee, "Analysis and design of a zero-voltage switched, three-phase pwm rectifier with power factor correction," in *Power Electronics Specialists Conference, 1992. PESC '92 Record., 23rd Annual IEEE*, 1992.
- [20] R. Jayabalan, B. Fahimi, A. Koenig, and S. Pekarek, "Applications of power electronics-based systems in vehicular technology: state-of-the-art and future trends," in *Power Electronics Specialists Conference, 2004. PESC 04. 2004 IEEE 35th Annual*, vol. 3, 2004, pp. 1887 – 1894 Vol.3.
- [21] R. Ghorbani and S. Haghbin, "Battery charge station using on-board motor drive," *US Patent no. 61540741*, filed on 29-09-2011, pending.
- [22] A. G. Cocconi, "Combined motor drive and battery recharge system," *US Patent no. 5,341,075*, 23 August 1994.
- [23] W. E. Rippel, "Integrated traction inverter and battery charger apparatus," *US Patent no. 4,920,475*, 24 April 1990.

- [24] —, “Integrated motor drive and recharge system,” *US Patent no. 5,099,186*, 24 March 1992.
- [25] L. De-Sousa and B. Bouchez, “Combined electric device for powering and charging,” *International Patent WO 2010/057892 A1*, 2010.
- [26] —, “Method and electric combined device for powering and charging with compensation means,” *International Patent WO 2010/057893 A1*, 2010.
- [27] L. De Sousa, B. Silvestre, and B. Bouchez, “A combined multiphase electric drive and fast battery charger for electric vehicles,” in *IEEE Vehicle Power and Propulsion Conference (VPPC) Proceedings, 2010, France*, Oct. 2010.
- [28] A. Bruyre, L. De Sousa, B. Bouchez, P. Sandulescu, X. Kestelyn, and E. Semail, “A multiphase traction/fast-battery-charger drive for electric or plug-in hybrid vehicles,” in *IEEE Vehicle Power and Propulsion Conference (VPPC) Proceedings, 2010, France*, Oct. 2010.
- [29] S. Lacroix, E. Laboure, and M. Hilairret, “An integrated fast battery charger for electric vehicle,” in *IEEE Vehicle Power and Propulsion Conference (VPPC) Proceedings, 2010, France*, Oct. 2010.
- [30] S. J. Lee and S. K. Sul, “An integral battery charger for 4 wheel drive electric vehicle,” in *Industry Applications Society Annual Meeting, 1994., Conference Record of the 1994 IEEE*, Oct. 1994, pp. 448–452 vol.1.
- [31] L. Solero, “Nonconventional on-board charger for electric vehicle propulsion batteries,” *Vehicular Technology, IEEE Transactions on*, vol. 50, no. 1, pp. 144–149, Jan. 2001.
- [32] F. Lacressonniere and B. Cassoret, “Converter used as a battery charger and a motor speed controller in an industrial truck,” in *Power Electronics and Applications, 2005 European Conference on*, 0 2005.
- [33] H.-C. Chang and C.-M. Liaw, “Development of a compact switched-reluctance motor drive for ev propulsion with voltage-boosting and pfc charging capabilities,” *Vehicular Technology, IEEE Transactions on*, vol. 58, no. 7, pp. 3198–3215, 2009.
- [34] M. Barnes and C. Pollock, “New class of dual voltage converters for switched reluctance drives,” *Electric Power Applications, IEE Proceedings -*, vol. 145, no. 3, pp. 164–168, May 1998.
- [35] —, “Forward converters for dual voltage switched reluctance motor drives,” *Power Electronics, IEEE Transactions on*, vol. 16, no. 1, pp. 83–91, Jan. 2001.
- [36] W. K. Thong and C. Pollock, “Low-cost battery-powered switched reluctance drives with integral battery-charging capability,” *Industry Applications, IEEE Transactions on*, vol. 36, no. 6, pp. 1676–1681, 2000.

- [37] R. M. Davis and W. F. Ray, "Battery chargers in variable reluctance electric motor systems," *U.K. Patent GB 1604066*, 1978.
- [38] G. Pellegrino, E. Armando, and P. Guglielmi, "An integral battery charger with power factor correction for electric scooter," *Power Electronics, IEEE Transactions on*, vol. 25, no. 3, pp. 751–759, 2010.
- [39] —, "An integral battery charger with power factor correction for electric scooter," in *Electric Machines and Drives Conference, 2009. IEMDC '09. IEEE International*, May 2009, pp. 661–668.
- [40] C. Stancu, S. Hiti, and E. Mundt, "Mobile electric power for medium and heavy duty hybrid electric vehicles," in *Power Electronics Specialists Conference, 2004. PESC 04. 2004 IEEE 35th Annual*, vol. 1, 2004, pp. 228–234 Vol.1.
- [41] F. J. Perez-Pinal and I. Cervantes, "Multi-reconfigurable power system for ev applications," in *Power Electronics and Motion Control Conference, 2006. EPE-PEMC 2006. 12th International*, 30 2006.
- [42] S. Y. Kim, I. Jeong, K. Nam, and H.-S. Song, "Three-port full bridge converter application as a combined charger for phev," in *Vehicle Power and Propulsion Conference, 2009. VPPC '09. IEEE*, 2009, pp. 461–465.
- [43] L. Tang and G.-J. Su, "Control scheme optimization for a low-cost, digitally-controlled charger for plug-in hybrid electric vehicles," in *Energy Conversion Congress and Exposition (ECCE), 2010 IEEE*, 2010, pp. 3604–3610.
- [44] G.-J. Su and L. Tang, "Control of plug-in hybrid electric vehicles for mobile power generation and grid support applications," in *Applied Power Electronics Conference and Exposition (APEC), 2010 Twenty-Fifth Annual IEEE*, 2010, pp. 1152–1157.
- [45] D. Thimmesch, "An scr inverter with an integral battery charger for electric vehicles," *Industry Applications, IEEE Transactions on*, vol. IA-21, no. 4, pp. 1023–1029, 1985.
- [46] C. Liaw and H. Chang, "An integrated driving/charging switched reluctance motor drive using three-phase power module," *Industrial Electronics, IEEE Transactions on*, 2010.
- [47] A.-T. Avestruz, J. Holloway, R. Cox, and S. Leeb, "Voltage regulation in induction machines with multiple stator windings by zero sequence harmonic control," in *Applied Power Electronics Conference and Exposition, 2005. APEC 2005. Twentieth Annual IEEE*, vol. 2, 2005, pp. 746–752 Vol. 2.
- [48] H. Plesko, J. Biela, J. Luomi, and J. Kolar, "Novel concepts for integrating the electric drive and auxiliary dc x2013;dc converter for hybrid vehicles," *Power Electronics, IEEE Transactions on*, vol. 23, no. 6, pp. 3025–3034, 2008.

- [49] Y.-J. Lee, A. Khaligh, and A. Emadi, "Advanced integrated bidirectional ac/dc and dc/dc converter for plug-in hybrid electric vehicles," *Vehicular Technology, IEEE Transactions on*, vol. 58, no. 8, pp. 3970–3980, 2009.
- [50] "Ac propulsion electric vehicle drive system specifications," *AC Propulsion Inc. Technical Note*, 2008.
- [51] G. Chen and K. Smedley, "Steady-state and dynamic study of one-cycle-controlled three-phase power-factor correction," *Industrial Electronics, IEEE Transactions on*, vol. 52, no. 2, pp. 355–362, april 2005.
- [52] Y. Liu and K. Smedley, "Control of a dual boost power factor corrector for high power applications," in *Industrial Electronics Society, 2003. IECON '03. The 29th Annual Conference of the IEEE*, vol. 3, nov. 2003, pp. 2929–2932 Vol.3.
- [53] R. Krishnan, *Switched Reluctance Motor Drives: Modeling, Simulation, Analysis, Design, And Applications*. CRC, 2001.
- [54] M. Krishnamurthy, C. Edrington, A. Emadi, P. Asadi, M. Ehsani, and B. Fahimi, "Making the case for applications of switched reluctance motor technology in automotive products," *Power Electronics, IEEE Transactions on*, vol. 21, no. 3, pp. 659–675, may 2006.
- [55] K. Rahman and S. Schulz, "High-performance fully digital switched reluctance motor controller for vehicle propulsion," *Industry Applications, IEEE Transactions on*, vol. 38, no. 4, pp. 1062–1071, jul/aug 2002.
- [56] H. Hannoun, M. Hilaret, and C. Marchand, "Design of an srm speed control strategy for a wide range of operating speeds," *Industrial Electronics, IEEE Transactions on*, vol. 57, no. 9, pp. 2911–2921, sept. 2010.
- [57] A. Emadi, S. Williamson, and A. Khaligh, "Power electronics intensive solutions for advanced electric, hybrid electric, and fuel cell vehicular power systems," *Power Electronics, IEEE Transactions on*, vol. 21, no. 3, pp. 567–577, may 2006.
- [58] E. Levi, "Multiphase electric machines for variable-speed applications," *Industrial Electronics, IEEE Transactions on*, vol. 55, no. 5, pp. 1893–1909, may 2008.
- [59] E. Levi, R. Bojoi, F. Profumo, H. Toliyat, and S. Williamson, "Multiphase induction motor drives - a technology status review," *Electric Power Applications, IET*, vol. 1, no. 4, pp. 489–516, july 2007.
- [60] L. Parsa, "On advantages of multi-phase machines," in *Industrial Electronics Society, 2005. IECON 2005. 31st Annual Conference of IEEE*, nov. 2005, p. 6 pp.
- [61] T. Lipo, "A dq model of a six-phase induction machine," *International conference of Electrical Machines, ICEM*, pp. 860–867, 1980.

- [62] S. Haghbin, *An Isolated Integrated Charger for Electric or Plug-in Hybrid Vehicles*. Licentiate Thesis, Chalmers University of Technology, 2011.
- [63] S. E. Lyshevski, *Electromechanical Systems, Electric Machines, and Applied Mechatronics*. CRC Press, 1999.
- [64] M. Malinowski, “Sensorless control strategies for three-phase pwm rectifiers,” Ph.D. dissertation, Faculty of Electrical Engineering, Institute of Control and Industrial Electronics, Warsaw University of Technology, 2001.
- [65] S. LECHAT SANJUAN, *Voltage Oriented Control of Three-Phase Boost PWM Converters*. Master Thesis, Chalmers University of Technology, 2010.
- [66] K. Khan, S. Haghbin, M. Leksell, and O. Wallmark, “Design and performance analysis of a permanent-magnet assisted synchronous reluctance machine for an integrated charger application,” in *Electrical Machines (ICEM), 2010 XIX International Conference on*, 2010, pp. 1–6.
- [67] B. K. Bose, *Modern power electronics and ac drives*. Prentice Hall, 2001.
- [68] P. Vas, *Sensorless vector and direct torque control*. Oxford Press, 1998.
- [69] D. Vindel, S. Haghbin, A. Rabiei, O. Carlson, and R. Ghorbani, “Field-oriented control of a pmsm drive system using the dspace controller,” in *Electric Vehicle Conference (IEVC), 2012 IEEE International*, march 2012, pp. 1–5.
- [70] K. Khan, *Design of a Permanent-Magnet Assisted Synchronous Reluctance Machine for a Plug-In Hybrid Electric Vehicle*. Licentiate Thesis, Royal Institute of Technology, 2011.
- [71] S. Zhao, *Modeling and control of a PMSynRel drive for a plug-in hybrid electric vehicle*. Licentiate Thesis, Royal Institute of Technology, 2011.
- [72] S. Haghbin, K. Khan, S. Zhao, M. Alakula, S. Lundmark, and O. Carlson, “An integrated 20-kw motor drive and isolated battery charger for plug-in vehicles,” *Power Electronics, IEEE Transactions on*, vol. 28, no. 8, pp. 4013–4029, aug. 2013.
- [73] S. Haghbin, M. Sadeghi Kani, D. Vindel, O. Carlson, and S. Lundmark, “A trigonometric velocity estimator using a resolver sensor in drive system applications,” in *IECON 2012 - 38th Annual Conference on IEEE Industrial Electronics Society*, oct. 2012, pp. 2889–2894.
- [74] J. Kolar, F. Zach, and F. Casanellas, “Losses in pwm inverters using igbts,” *Electric Power Applications, IEE Proceedings -*, vol. 142, no. 4, pp. 285–288, jul 1995.
- [75] F. Casanellas, “Losses in pwm inverters using igbts,” *Electric Power Applications, IEE Proceedings -*, vol. 141, no. 5, pp. 235–239, sep 1994.

- [76] *IEC 61000-4-5, Electromagnetic compatibility EMC Part 4-5: Testing and measurement techniques Surge immunity test*, IEC Standard, 2005.
- [77] S. Haghbin, S. Lundmark, O. Carlson, and M. Alakula, "A combined motor/drive/battery charger based on a split-windings pmsm," in *Vehicle Power and Propulsion Conference (VPPC), 2011 IEEE*, sept. 2011, pp. 1–6.
- [78] R. Hoseinnezhad, A. Bab-Hadiashar, and P. Harding, "Calibration of resolver sensors in electromechanical braking systems: A modified recursive weighted least-squares approach," *Industrial Electronics, IEEE Transactions on*, vol. 54, no. 2, pp. 1052–1060, april 2007.
- [79] G. Liu, "On velocity estimation using position measurements," in *American Control Conference, 2002. Proceedings of the 2002*, vol. 2, 2002, pp. 1115–1120 vol.2.
- [80] Y. Su, C. Zheng, P. Mueller, and B. Duan, "A simple improved velocity estimation for low-speed regions based on position measurements only," *Control Systems Technology, IEEE Transactions on*, vol. 14, no. 5, pp. 937–942, sept. 2006.
- [81] S.-M. Yang and S.-J. Ke, "Performance evaluation of a velocity observer for accurate velocity estimation of servo motor drives," *Industry Applications, IEEE Transactions on*, vol. 36, no. 1, pp. 98–104, jan/feb 2000.
- [82] A. Michalski, J. Sienkiewicz, and Z. Watral, "Universal magnetic circuit for resolvers with different speed ratios [instrumentation notes]," *Instrumentation Measurement Magazine, IEEE*, vol. 10, no. 5, pp. 58–68, october 2007.
- [83] C. Attaianesi and G. Tomasso, "Position measurement in industrial drives by means of low-cost resolver-to-digital converter," *Instrumentation and Measurement, IEEE Transactions on*, vol. 56, no. 6, pp. 2155–2159, dec. 2007.
- [84] R. Lorenz and K. Van Patten, "High-resolution velocity estimation for all-digital, ac servo drives," *Industry Applications, IEEE Transactions on*, vol. 27, no. 4, pp. 701–705, jul/aug 1991.
- [85] G.-C. Hsieh and J. Hung, "Phase-locked loop techniques. a survey," *Industrial Electronics, IEEE Transactions on*, vol. 43, no. 6, pp. 609–615, dec. 1996.
- [86] A. Bellini and S. Bifaretti, "Implementation of a digital filter for speed noise reduction in drives with electromagnetic resolver," in *Power Electronics and Applications, 2005 European Conference on*, 0-0 2005, pp. 10 pp. –P.10.
- [87] L. Harnefors, "Speed estimation from noisy resolver signals," in *Power Electronics and Variable Speed Drives, 1996. Sixth International Conference on (Conf. Publ. No. 429)*, sept. 1996, pp. 279–282.

- [88] L. Ben-Brahim and M. Benammar, "A new pll method for resolvers," in *Power Electronics Conference (IPEC), 2010 International*, june 2010, pp. 299–305.
- [89] K. W and M. Konghirun, "A dsp - based vector control of pmsm servo drive using resolver sensor," in *TENCON 2006. 2006 IEEE Region 10 Conference*, nov. 2006, pp. 1–4.
- [90] S.-H. Hwang, H.-J. Kim, J.-M. Kim, L. Liu, and H. Li, "Compensation of amplitude imbalance and imperfect quadrature in resolver signals for pmsm drives," *Industry Applications, IEEE Transactions on*, vol. 47, no. 1, pp. 134–143, jan.-feb. 2011.
- [91] C.-H. Yim, I.-J. Ha, and M.-S. Ko, "A resolver-to-digital conversion method for fast tracking," *Industrial Electronics, IEEE Transactions on*, vol. 39, no. 5, pp. 369–378, oct 1992.
- [92] R. Brown, S. Schneider, and M. Mulligan, "Analysis of algorithms for velocity estimation from discrete position versus time data," *Industrial Electronics, IEEE Transactions on*, vol. 39, no. 1, pp. 11–19, feb 1992.
- [93] J. Spriet and J. Bens, "Optimal design and comparison of wide-band digital on-line differentiators," *Acoustics, Speech and Signal Processing, IEEE Transactions on*, vol. 27, no. 1, pp. 46–52, feb 1979.
- [94] N. Hagiwara, Y. Suzuki, and H. Murase, "A method of improving the resolution and accuracy of rotary encoders using a code compensation technique," *Instrumentation and Measurement, IEEE Transactions on*, vol. 41, no. 1, pp. 98–101, feb 1992.
- [95] A. Boglietti, M. Lazzari, and M. Pastorelli, "Iron losses prediction with pwm inverter supply using steel producer data sheets," in *Industry Applications Conference, 1997. Thirty-Second IAS Annual Meeting, IAS '97., Conference Record of the 1997 IEEE*, vol. 1, oct 1997, pp. 83–88 vol.1.
- [96] T. Mthombeni, P. Pillay, and R. Strnat, "New epstein frame for lamination core loss measurements under high frequencies and high flux densities," *Energy Conversion, IEEE Transactions on*, vol. 22, no. 3, pp. 614–620, sept. 2007.
- [97] N. Mohan, M. T. Undeland, and W. P. Robbins, *Power Electronics: Converters, Applications, and Design*. John Wiley and Sons, 1995.
- [98] T. Ohnuki, O. Miyashita, T. Haneyoshi, and E. Ohtsuji, "High power factor pwm rectifiers with an analog pulsewidth prediction controller," *Power Electronics, IEEE Transactions on*, vol. 11, no. 3, pp. 460–465, may 1996.
- [99] A. de Castro, P. Zumel, O. Garcia, T. Riesgo, and J. Uceda, "Concurrent and simple digital controller of an ac/dc converter with power factor correction based on an fpga," *Power Electronics, IEEE Transactions on*, vol. 18, no. 1, pp. 334–343, jan 2003.

- [100] H. Kanaan and K. Al-Haddad, "Modeling techniques applied to switch-mode power converters: application to the boost-type single-phase full-bridge rectifier," in *Human System Interactions, 2008 Conference on*, may 2008, pp. 979 –983.
- [101] M.-Y. Chang, J.-Y. Lin, and Y.-Y. Tzou, "Dsp-based fully digital control of a ac/dc converter with a nonlinear digital current mode control," in *Power Electronics Specialists Conference, 1996. PESC '96 Record., 27th Annual IEEE*, vol. 2, jun 1996, pp. 1702 –1708 vol.2.
- [102] R. Bojoi, M. Lazzari, F. Profumo, and A. Tenconi, "Digital field-oriented control for dual three-phase induction motor drives," *Industry Applications, IEEE Transactions on*, vol. 39, no. 3, pp. 752 – 760, may-june 2003.
- [103] R. Bojoi, E. Levi, F. Farina, A. Tenconi, and F. Profumo, "Dual three-phase induction motor drive with digital current control in the stationary reference frame," *Electric Power Applications, IEE Proceedings -*, vol. 153, no. 1, pp. 129 – 139, jan. 2006.
- [104] R. Kianinezhad, B. Nahid-Mobarakeh, L. Baghli, F. Betin, and G.-A. Capolino, "Modeling and control of six-phase symmetrical induction machine under fault condition due to open phases," *Industrial Electronics, IEEE Transactions on*, vol. 55, no. 5, pp. 1966 –1977, may 2008.
- [105] G. Singh, K. Nam, and S. Lim, "A simple indirect field-oriented control scheme for multiphase induction machine," *Industrial Electronics, IEEE Transactions on*, vol. 52, no. 4, pp. 1177 – 1184, aug. 2005.
- [106] L. Parsa and H. Toliyat, "Multi-phase permanent magnet motor drives," in *Industry Applications Conference, 2003. 38th IAS Annual Meeting. Conference Record of the*, vol. 1, oct. 2003, pp. 401 – 408 vol.1.
- [107] F. Scuiller, E. Semail, J.-F. Charpentier, and P. Letellier, "Multi-criteria-based design approach of multi-phase permanent magnet low-speed synchronous machines," *Electric Power Applications, IET*, vol. 3, no. 2, pp. 102 –110, march 2009.
- [108] L. De Camillis, M. Matuonto, A. Monti, and A. Vignati, "Optimizing current control performance in double winding asynchronous motors in large power inverter drives," *Power Electronics, IEEE Transactions on*, vol. 16, no. 5, pp. 676 –685, sep 2001.
- [109] M. Haque and M. Rahman, "Control trajectories for interior permanent magnet synchronous motor drives," in *Electric Machines Drives Conference, 2007. IEMDC '07. IEEE International*, vol. 1, may 2007, pp. 306 –311.
- [110] A. Consoli, G. Scarcella, G. Scelba, and A. Testa, "Steady-state and transient operation of ipmsms under maximum-torque-per-ampere control," *Industry Applications, IEEE Transactions on*, vol. 46, no. 1, pp. 121 –129, jan.-feb. 2010.

- [111] C.-T. Pan and S.-M. Sue, "A linear maximum torque per ampere control for ipmsm drives over full-speed range," *Energy Conversion, IEEE Transactions on*, vol. 20, no. 2, pp. 359 – 366, june 2005.
- [112] L. Harnefors, *Control of variable-speed drives*. Course compendium, Mälardalen University, Sweden, 2002.